UNIVERSITY OF CALIFORNIA SAN DIEGO

Biosensing In-Ear Systems: Expanding Opportunities for Mobile Health Monitoring and Brain-Computer Interfaces

A dissertation submitted in partial satisfaction of the
requirements for the degree
Doctor of Philosophy

in

Bioengineering

by

Akshay Paul

Committee in charge:

Professor Gert Cauwenberghs, Chair
Professor Todd P. Coleman
Professor William D. Hairston
Professor Patrick P. Mercier
Professor Erik S. Viirre
Professor Sheng Xu

2023

The dissertation of Akshay Paul is approved, and it is acceptable in quality and form for publication on microfilm and electronically.

University of California San Diego

2023

DEDICATION

Dedicated to my parents and brother,

for their immense love and support.

EPIGRAPH

If you wish to make an apple pie from scratch, you must first invent the universe.

—Carl Sagan

Success is the sum of small efforts – repeated day in and day out.

– Robert Collier

On all four sides, surrounded by the Lord's Circle of Protection

—Guru Arjan Dev Ji

TABLE OF CONTENTS

LIST OF FIGURES

LIST OF TABLES

ACKNOWLEDGEMENTS

Foremost, I would like to thank my advisor and committee chair, Professor Gert Cauwenberghs for his steadfast support, guidance, and wisdom which were instrumental in the completion of this work and have proved to be invaluable to my personal growth.

I would like to thank members of my committee, Prof. Todd Coleman, Dr. Dave Hairston, Prof. Patrick Mercier, Prof. Erik Viirre, and Prof. Sheng Xu for their willingness to collaborate, openness to share ideas, and generosity with time to aid in the development of this work. Thank you to Dr. Dave Hairston for being an invaluable advisor, mentor, and research collaborator for the past several years.

I would also like to acknowledge Stephen Deiss, Yuchen Xu, and Min Lee for being immeasurably generous with their time, expertise, help, and support over the course of many wonderful ear-related research projects, which has contributed towards the success of this work and my growth as a researcher. I acknowledge all members of the Integrated Systems Neuroengineering (ISN) Laboratory, especially Preston Fowler, Jiajia Wu, Gopabandhu Hota, Jeremy Ford, Soumil Jain, Gwenevere Frank, and Jeonghoon Kim, for providing assistance during various stages of this work and for helping to create a warm and friendly lab environment.

I am very grateful to former members of the ISN lab, many of whom were excellent mentors, including Jun Wang, Rajkumar Kubendran, and Abraham Akinin.

Chapter 3 is largely a reprint of material as it may appear in IEEE Explore, 2019, Akshay Paul, Abraham Akinin, Min S. Lee, Matthew Kleffner, Stephen R. Deiss, and

Gert Cauwenberghs, "Integrated In-Ear Device for Auditory Health Assessment," *41st Annual International Conference of the IEEE Engineering in Medicine and Biology Society (EMBC)*. The thesis author was the primary investigator and author of this paper.

Chapter 4 is largely a reprint of material as it may appear in IEEE Explore, 2018, Akshay Paul, Stephen Deiss, Dave Tourtelotte, Matt Kleffner, Tao Zhang, and Gert Cauwenberghs,"Electrode-skin impedance characterization of in-ear electrophysiology accounting for cerumen and electrodermal response," *9th International IEEE/EMBS Conference on Neural Engineering (NER)*. The thesis author was the primary investigator and author of this paper.

Chapter 5 is largely a reprint of material as it may appear in IEEE Explore, 2022, Akshay Paul, Min S. Lee, Yuchen Xu, Stephen R. Deiss, and Gert Cauwenberghs, "A versatile in-ear biosensing system for continuous brain and health monitoring," *2022 IEEE International Symposium on Circuits and Systems (ISCAS)*. The thesis author was the primary investigator and author of this paper.

Chapter 6 is largely a combination of material as it may appear in the following venues: Akshay Paul, Min S. Lee, Yuchen Xu, Stephen R. Deiss, and Gert Cauwenberghs, "A versatile in-ear biosensing system for continuous brain and health monitoring," *2022 IEEE International Symposium on Circuits and Systems (ISCAS)*, May 2022 and Akshay Paul, Min S Lee, Yuchen Xu, Stephen R Deiss, and Gert Cauwenberghs, "A Versatile In-Ear Biosensing System and Body-Area Network for Unobtrusive Continuous Health Monitoring," *IEEE Transactions on Biomedical Circuits and Systems (TBioCAS)*, 2023. The thesis author was the primary investigator and author of this paper.

Chapter 7 is largely a combination of material as it may appear in the following venues: Akshay Paul, Preston Fowler, Yuchen Xu, Min S. Lee, Jun Wang, and Gert Cauwenberghs, "Neural Recording Analog Front-End Noise Reduction with Digital Correlated Double Sampling," *IEEE Biomedical Circuits and Systems Conference (BioCAS)*, Oct. 2022 and Akshay Paul, Preston Fowler, Yuchen Xu, Min S. Lee, Gabor Temes, and Gert Cauwenberghs, "Window-Optimized Digital Correlated Double Sampling for Analog Front-End Noise Suppression," *IEEE Transactions on Biomedical Circuits and Systems (TBioCAS)*, 2023. The thesis author was the primary investigator and author of this paper.

Chapter 8 is largely a reprint of material as it may appear in IEEE Explore, 2021, Akshay Paul, Gopabandhu Hota, Behnam Khaleghi, Yuchen Xu, Tajana Rosing, and Gert Cauwenberghs, "Attention State Classification with In-Ear EEG," *IEEE Biomedical Circuits and Systems Conference (BioCAS)*. The thesis author was the primary investigator and author of this paper.

VITA

2015	B.S. in Biomedical Engineering, University of California Irvine
2018	M.S. in Bioengineering, University of California San Diego
2023	Ph. D. in Bioengineering, University of California San Diego

PUBLICATIONS

Akshay Paul, Preston Fowler, Yuchen Xu, Min S. Lee, Gabor Temes, and Gert Cauwenberghs, "Window-Optimized Digital Correlated Double Sampling for Analog Front-End Noise Suppression," *IEEE Transactions on Biomedical Circuits and Systems (TBioCAS)*, 2023 (submitted)

Akshay Paul, Min S Lee, Yuchen Xu, Stephen R Deiss, and Gert Cauwenberghs, "A Versatile In-Ear Biosensing System and Body-Area Network for Unobtrusive Continuous Health Monitoring," *IEEE Transactions on Biomedical Circuits and Systems (TBioCAS)*, 2023

Akshay Paul, Preston Fowler, Yuchen Xu, Min S. Lee, Jun Wang, and Gert Cauwenberghs, "Neural Recording Analog Front-End Noise Reduction with Digital Correlated Double Sampling," *IEEE Biomedical Circuits and Systems Conference (BioCAS)*, Oct. 2022

Min S. Lee, Akshay Paul, Yuchen Xu, W. David Hairston, and Gert Cauwenberghs, "Characterization of Ag/AgCl Dry Electrodes for Wearable Electrophysiological Sensing," *Frontiers in Electronics*, 2022

Akshay Paul, Min S. Lee, Yuchen Xu, Stephen R. Deiss, and Gert Cauwenberghs, "A versatile in-ear biosensing system for continuous brain and health monitoring," *2022 IEEE International Symposium on Circuits and Systems (ISCAS)*, May 2022

Benjamin Hofflich, Irene Lee, Alan Lunardhi, Nitesh Sunku, Jason Tsujimoto, Gert Cauwenberghs, and Akshay Paul, "Audio Mapping Using LiDAR to Assist the Visually Impaired," *IEEE Biomedical Circuits and Systems Conference (BioCAS)*, 2022

Serena Tang, Keli Wang, Stephanie Ogrey, Jorge Villazon, Sana Khan, Akshay Paul, Nolan Ardolino, Rajkumar Kubendran, and Gert Cauwenberghs, "Unity Human Eye Model for Gaze Tracking with a Query-Driven Dynamic Vision Sensor," *44th Annual International Conference of the IEEE Engineering in Medicine & Biology Society (EMBC)*, 2022

Jun Wang, Ren Liu, Youngbin Tchoe, Alessio Paolo Buccino, Akshay Paul, Agnieszka D'Antonio-Chronowska, Kelly A Frazer, Chul Kim, Shadi Dayeh, and Gert Cauwenberghs, "Low-Power 256-Channel Nanowire Electrode-on-Chip Neural Interface for Intracellular Electrophysiology," *IEEE Biomedical Circuits and Systems Conference (BioCAS)*, 2021

Akshay Paul, Gopabandhu Hota, Behnam Khaleghi, Yuchen Xu, Tajana Rosing, and Gert Cauwenberghs, "Attention State Classification with In-Ear EEG," *IEEE Biomedical Circuits and Systems Conference (BioCAS)*, 2021

Rajkumar Kubendran, Akshay Paul, and Gert Cauwenberghs, "A 256x256 6.3 pj/pixel-event query-driven dynamic vision sensor with energy-conserving row-parallel event scanning," *IEEE Custom Integrated Circuits Conference (CICC)*, 2021

Jun Wang, Akshay Paul, Dinghong Zhang, Jiajia Wu, Yuchen Xu, Yimin Zou, Chul Kim, and Gert Cauwenberghs, "1024-Electrode hybrid voltage/current-clamp neural interface system-on-chip with dynamic Incremental-SAR acquisition," *IEEE Symposium on VLSI Circuits*, 2020

Abraham Akinin, Akshay Paul, Jun Wang, Alessio Buccino, and Gert Cauwenberghs, "Biopotential measurements and electrodes," *Neural Engineering*, Springer 2020

Akshay Paul, Abraham Akinin, Min S. Lee, Matthew Kleffner, Stephen R. Deiss, and Gert Cauwenberghs, "Integrated In-Ear Device for Auditory Health Assessment," *41st Annual International Conference of the IEEE Engineering in Medicine and Biology Society (EMBC)*, April 2019

Akshay Paul, Stephen R Deiss, David Tourtelotte, Matthew Kleffner, Tao Zhang, and Gert Cauwenberghs, "Electrode-skin impedance characterization of in-ear electrophysiology accounting for cerumen and electrodermal response," *9th International IEEE/EMBS Conference on Neural Engineering (NER)*, March 2019

ABSTRACT OF THE DISSERTATION

Biosensing In-Ear Systems: Expanding Opportunities for Mobile Health Monitoring and Brain-Computer Interfaces

by

Akshay Paul

Doctor of Philosophy in Bioengineering

University of California San Diego, 2023

Professor Gert Cauwenberghs, Chair

The importance of health sensing continues to grow in light of an aging global population, the prevalence of chronic illness, a dramatic rise in mental health disorders, and a healthcare system with gaps in equal coverage for everyone. Wearable sensing technologies have greatly expanded health monitoring and human-computer interface applications, bridging the gaps between traditional clinical instrumentation and urgent need for remote, daily healthcare. Noninvasive electrophysiology tools in particular seek to measure signals from the brain and body at conventional sensing locations such as the scalp,

but require bulky instrumentation and cumbersome setup procedures, limiting prolonged use in real-world settings. As an appealing alternative, electrophysiological sensing within the ear provides continuous physiological and cognitive state monitoring in an unobtrusive form factor. The proximity of the ear to the central nervous system and the high density of exocrine glands in the ear canal motivate the integration of multiple sensing modalities including electroencephalography (EEG), electrodermal activity (EDA), and metabolite detection into a single in-ear device. The work in this dissertation extends the capabilities and amplifies the impact of in-ear sensing systems addressing several of their limitations including electrode performance, manufacturing scalability, and low-power acquisition hardware. A primary aim of this work is to enhance in-ear sensors to support higher electrode count, offering reliable, long-term wearability, user comfort, and straightforward fabrication methods to benefit investigation of physiological signals in a broader subject pool. Another primary aim of this work is to provide high-performance data acquisition hardware to meet the needs of mobile health monitoring from multimodal sensor arrays. First, new methods for the development of in-ear sensors are presented which deliver user-generic dry-contact electrodes made from standard printed circuit boards (PCBs). Electrodes are characterized using electrochemical impedance spectroscopy (EIS) and a series of in-vivo electrophysiological studies. The second part presents a complete and versatile wireless electrophysiology data acquisition system (weDAQ) that is demonstrated for in-ear EEG and on-body electrophysiology as an open-source resource for the biomedical community. Subsequently, a neural interface system-on-chip (NISoC) integrated circuit (IC) is presented which substantially lowers the power and improves signal integrity through a

new correlated double sampling (CDS) technique. Finally, the sensing system is evaluated for use with subjects for auditory steady-state response (ASSR), electrodermal activity (EDA), and attention state classification (vigilance), demonstrating its utility as a versatile, mobile health monitoring platform.

Chapter 1

Outline

This dissertation aims to elucidate the health sensing opportunities of ear-worn devices by focusing on the design and implementation of multimodal sensor systems for the investigation of physiological and cognitive biomarkers including electrophysiology towards the functional validation of in-ear mobile health monitoring. To prevail in this endeavor the research presented pursues a synergistic approach combining three key aspects: electrophysiological examination of brain and body biomarkers, multimodal sensor arrays, and versatile bioinstrumentation.

Chapter 2 presents a review of the emerging field of hearables with an emphasis on health and wellness sensing. It begins with a brief overview of the current state of health in the US and globally, and the projected demands for healthcare in the near future. Critical unmet needs are highlighted in the realm of health monitoring specifying limitations in current standards of care and available tools. This section then introduces sensing from the ear as an alternative to conventional locations showcasing the wealth of signals detectable

while considering tradeoffs. Current approaches from literature for in-ear sensing are briefly reviewed and limitations are identified. A strategy is proposed for expanding in-ear health monitoring that includes new sensor development, data acquisition hardware, and combined paradigms of biosignal detection.

Chapter 3 discusses the utilization of in-ear electroencephalography in conjunction with an integrated means of presenting sound stimuli for the assessment of auditory health. A 3D printed earpiece custom-fitted to the user with a new bead-style, Ag-AgCl set of electrodes is developed to provide high-density recording of brain activity. Sound is delivered through the device into the auditory canal by means of an air conduit attached to an external transducer. In this section, the auditory steady-state response (ASSR) from the auditory cortex is examined with a uniform white noise amplitude modulated sound stimulus. Characteristic spectral features in the EEG from subjects hearing the stimulus are correlated to audition and auditory health of the subject. This section presents tools and methodology laying the groundwork for a mobile auditory health assessment system.

Chapter 4 presents an in-ear sensor device designed in the footprint of a custom-fitted hearing aid with high-density electrodes spanning 3 key regions of the ear. The device is demonstrated for performing in-ear impedance scanning of the electrode-skin interface. Experimental results show the variation in impedance across the 3 regions of the ear with the lowest values arising from the ear canal and the highest from the concha cymba. Sampled over time, an average of electrode-skin impedance mapped onto the 3D surface of the in-ear device reveals spatial patterns across the ear. Further, an electrodermal activity monitoring study is conducted with the subject exposed to an acute stimulus following a baseline

period of rest inducing an increase in skin conductivity measured at the conventional palm locations and observed in the ear from canal electrodes. Clinically relevant applications of electrodermal activity monitoring from the ear can include emotional status, flight-or-fright response, stress, and other physiological states.

Chapter 5 presents novel electrode sensor designs for reliable, scalable, and high-density in-ear sensor arrays. This section demonstrated the feasibility of leveraging turn-key conventional printed circuit board techniques for producing robust in-ear sensors with minimal manual processing and assembly. The first design instantiation is the *Crocodile v1*, a user-generic 16-electrode in-ear sensor array formed simply by mating 2 PCB together and inserting into the ear canal. A second iteration of the PCB-based sensor design sees the *Crocodile v2*, with integrated reference and driven-right-leg channels for 18 total electrodes, and an integrated ZIF connector for interfacing with standard FPC ribbon cables. The *Crocodile v2* notably has degrees of freedom between its 3 mating sub-PCBs which allows for an anatomically tunable fit between the ears of the same subject and between the ears of different subjects, improving electrode-skin contact, sensing coverage, and user comfort. Finally, this section highlights the integration of a universal electrode harness into custom-fitted hardshell earpieces in order to maximize user comfort, mechanical fit, and multimodal sensor integration. The flexible electrode harness is demonstrated to fit well inside the earpieces of different subjects and supports integration of additional sensors such as accelerometers, IR LED emitters and receivers, temperature sensors, and more.

Chapter 6 presents a versatile data acquisition system developed for wearable health monitoring applications including in-ear sensing called weDAQ. The system was

designed to accommodate a larger number of channels and a higher sampling rate than other comparable wearable DAQs. The weDAQ was demonstrated to measure vital biosignals from in-ear and on-body sensors including EEG, EMG, ECG, EOG, EDA, and movement tracking. In conjunction with a WiFi access point, several weDAQ units were demonstrated to form a body-sensor-network to synchronously stream data wirelessly from multiple areas of the body across multiple subjects to a single lab streaming layer server port. Moreover, this section discusses the impact of the open-source resources made available to the research community.

Chapter 7 highlights development and validation of an integrated circuit BioADC for low-power application in neural interfaces, general health sensing, and as an electrochemical sensor amplifier. With a small 1 mm-squared footprint the chip designed in a 65-nm CMOS process offers adequate measurement capabilities for recording of in-ear signal but at a fraction of the power consumption. Designed with an input multiplexer that enables correlated double-sampling, low frequency noise and offset is effectively removed from the measurement.

Chapter 8 presents an attention state decoding paradigm from signals measured with in-ear devices. EEG is captured from in-ear electrodes during a vigilance task which assesses a subject's reaction time and visual attention. A common-spatial pattern algorithm is then deployed with spectral filter banks to extract features from recorded in-ear EEG data during the vigilance task to train models for detection of attention state.

Chapter 9 summarizes the contributions of this thesis and explains the future directions of the research effort.

Chapter 2

In-Ear Health Sensing

2.1 Introduction

In light of an aging global population, the prevalence of chronic illness, and a dramatic rise in mental health disorders, our already imperfect health care system is at a critical point [51, 65]. Chronic diseases are the leading cause of death and disability in the US afflicting 60% of the population [28, 37, 67, 104, 107]. The goal of health care in a general sense is to reduce mortality and morbidity in the population it serves [49, 63]. Health sensing is instrumental in the prevention and early detection of disease which can reduce suffering and medical cost [30, 81]. Electrophysiology tools in particular seek to measure signals from the brain and body at conventional sensing locations such as the scalp or the chest [8]. For chronic diseases, these biosignals should be chronically monitored. Sensors in the context of health can have one or more of the following 6 objectives, to: monitor, track, warn, regulate (support), and control (intervene). For the scope of this

work, health sensing will consider the first 3 of these objectives.

2.1.1 Clinical Health Monitoring

Clinical electrophysiology tools are an indispensable part of patient in-take and continuous care during a visit to the hospital [8]. Common electrophysiology tools are electrocardiogram (ECG) which measures electrical activity from the heart with 12 or more electrodes placed on the patient's chest [22]. Electroencephalography (EEG) involves placement of electrodes on the scalp to measure electrical activity from the brain [112] and electromyogram (EMG) measures muscle activity from electrodes placed on the muscle groups of interest [58]. Upon discharge from the hospital however, this vital stream of information stops because these clinical tools are not designed to leave with the subject as they resume life in their natural environment such as at home or in the office. Bulky instrumentation and cumbersome setup procedures are in-part responsible for the limited prolonged use of these tools in real-world settings.

2.1.2 Wearable Technologies

Wearable technologies which seek to bring sensors and acquisition hardware into a streamlined integration that can be worn by a subject via attachment to the skin, clothing, strapped around a limb, or a number of other means [109]. Wearables greatly expand health monitoring and human-computer interfaces by improving the usability and applicability of body sensing tools in the real-world environment [46,73]. They help bridge the gaps between clinical tools and the urgent need for remote health care. Examples of wearables in the

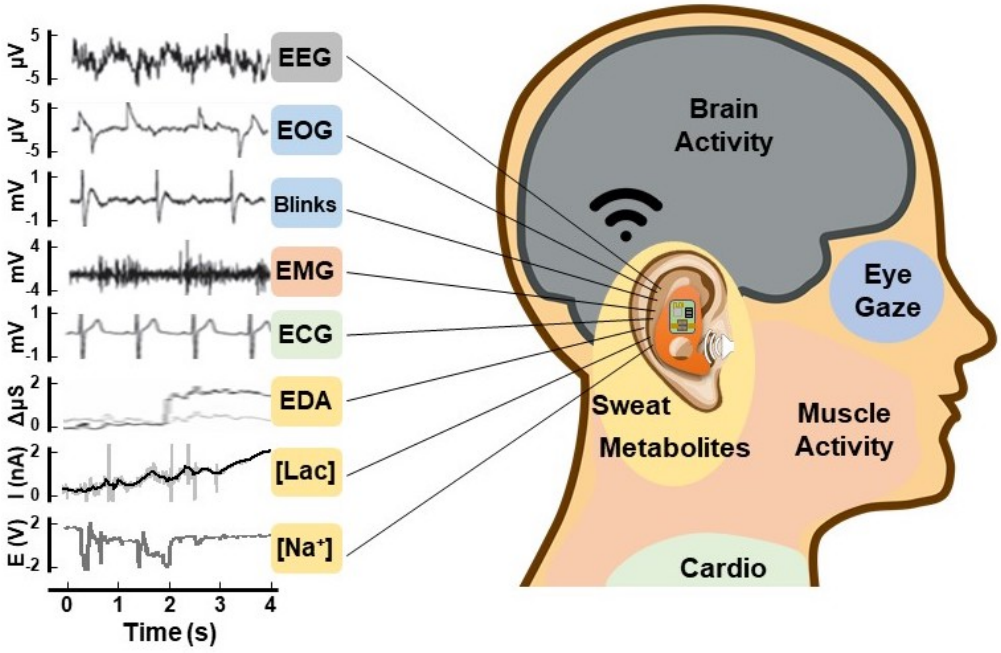

Figure 2.1: An overview of biosignals directly measured from the ear made possible by the co-location of several signals of interest originating from the brain, eyes, body, and skin processes.

market that are improving lives include the Dexcom G7 which continuously monitors blood glucose levels to warn users and the Apple Watch with integrated sensor providing heart rate, blood oxygenation, and ECG, amongst other useful biomarkers [29, 50]. Such devices have partially demonstrated the utility of mobile health monitoring to aging in-place for the elderly, chronic condition tracking, and facilitating medical treatment compliance [91].

2.2 Multi-modal In-Ear Sensing

As an appealing alternative to standard locations, sensing within the ear provides continuous physiological and cognitive state monitoring in an unobtrusive form factor. The proximity of the ear to the central nervous system and the high density of exocrine glands in the ear canal motivate the integration of multiple sensing modalities including electroencephalography (EEG), electrodermal activity (EDA), and metabolite detection into a single in-ear device [59, 61]. Brain activity measured as in-ear EEG reflects changes in alpha band power (8-12 Hz) shown to modulate when subjects open or close their eyes and is positively correlated with relaxation or meditative states [68]. These sensors can also detect eye blinks and eye movements by tracking the ocular dipole as subjects change their gaze direction [72]. Muscle activity from the face, jaw, and neck is robustly detected from the ear because of the proximity these sensors have to these muscle groups but also because the amplitude of EMG signals can be orders of magnitude larger than EEG [71]. Clenching of the masseter jaw muscle, movement of the head, and certain facial expressions have been demonstrated to be detected from in-ear sensors. These signals can be leveraged by brain-computer interface applications for speech recognition, non-verbal cues, and gesturing.

At least 3 kinds of sweat glands are present inside the ear with relatively high density compared to the rest of the body including apocrine, eccrine, and ceruminous glands [52]. While apocrine glands are found all over the body and are activated primarily by heat, eccrine glands are controlled by the autonomic nervous systems via sympathetic

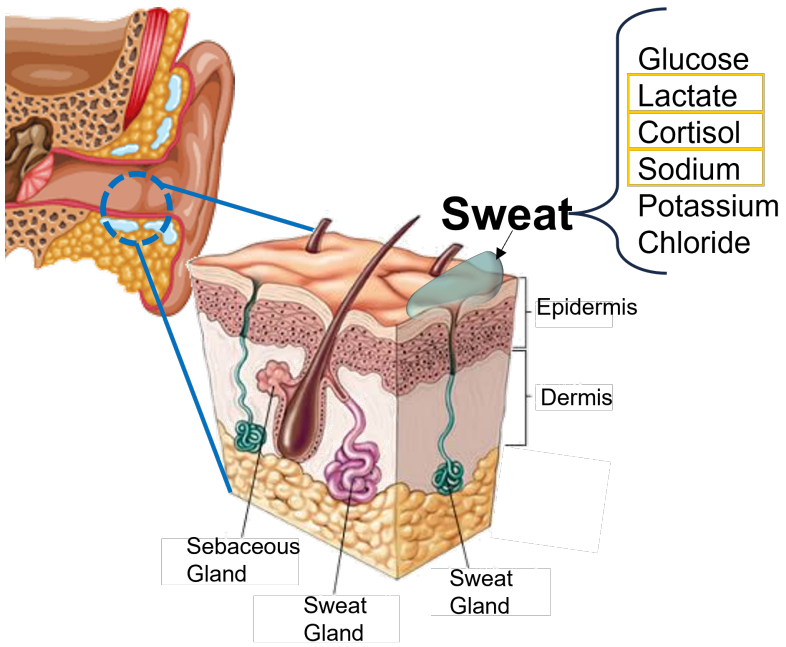

Figure 2.2: The ear canal has a high-density of exocrine glands including sweat, sebaceous, and ceruminous glands.

innervations [93]. Activation of these glands corresponds to deep inspiration, mental stress, fright, and local tactile stimulation (emotional sweating), resulting in acute changes in skin conductivity, also known as electrodermal activity [16]. Effective measurement of EDA requires the density of these glands be high enough to produce a quantifiable change in skin conductivity which is conventionally only found on the palms of the hands or the underside of the feet [15]. This work shows the detection of the EDA signature from the ear canal as well, given the high density of eccrine glands present.

The ear canal therefore is seen to produce measurable amounts of sweat as a result of these glands being present with high density [92]. Metabolites normally detectable in sweat from other parts of the body are also shown to be found in-ear [7]. Of particular

interest to our team of collaborators is the measurement of lactate, cortisol, and sodium levels in the sweat [88,97,110]. Lactate is a metabolite found in sweat correlated to exertion and fatigue, cortisol is a hormone, high levels of which have been correlated with stress, and sodium is an ion present in sweat representative of a subject's hydration status [9, 86]. Multiple of these sensing modalities can be integrated to offer greater functionality where biosignals of interest are conveniently co-located. This concept is supported by the various biosignals introduced above that have been captured from in-ear devices.

Contemporary in-ear devices in the field have focused primarily on support for EEG [40, 42, 82]. Some have been validated for EOG [13, 39], very few for EDA [76], and none for metabolite sensing at the time of this review. Although capable in-ear platforms, most in-ear devices in the field have long wires and only a limited number of electrodes (most with ≤ 8 electrodes per ear). In addition, the fabrication of these devices is complicated, with very limited details of fabrication methods disseminated. Addressing several of their limitations including electrode performance, manufacturing scalability, and low-power acquisition hardware is a primary focus of this work.

2.2.1 Emphasis of this Work

The emphasis of this dissertation is organized in 2 primary aims: (1) to enhance in-ear sensors to support higher electrode count, offering reliable, long-term wearability, user comfort, and straightforward fabrication methods to benefit investigation of physiological signals in a broader subject pool; and, (2) to provide high-performance data acquisition hardware to meet the needs of mobile health monitoring from multimodal sensor arrays.

Chapter 3

Auditory Health Assessment with Integrated In-Ear EEG

3.1 Introduction

Clinical assessment of the human auditory system is an integral part of evaluating the health of a patient's cognitive processes. Conventional tests performed by audiologists include the Auditory Steady State Response (ASSR) and the Auditory Brainstem Response (ABR), both of which present an audio stimulus to the patient in order to elicit a change in brain state measurable by electroencephalography (EEG) techniques. Spatial monitoring of the electrophysiological activity in the auditory cortex, temporal cortex, and brain stem during auditory stimulus evaluation can be used to pinpoint to location of auditory dysfunction along the auditory pathway. However, given the obtrusive nature of conventional auditory evaluation techniques and the lack of information about sound transduction and

cochlear dynamics usually irrecoverable by EEG, a better approach is needed to improve its clinical utility. Here, we present an in-ear device for auditory health assessment that integrates a sound engine for stimulation and high-density dry-electrode EEG for real-time simultaneous recording of brain activity. This system provides ease-of-use and patient comfort. We also investigate the auditory transfer function of the hearing system as an intricate convolution of the tympanic membrane, middle ear bones, and the cochlear subsystems.

3.1.1 Auditory System

The human auditory system utilizes mechanical and electrical processes to sense, filter, and amplify sound pressure waves to electrical impulses in the brain. Dysfunction and disease can impact the performance of any or all portions of the auditory pathway, producing serious and often, confounding pathology. In the cases of patients presenting symptoms of tinnitus, for example, dysfunction can occur at the cochlear hair cells, in the auditory nerves, the brainstem, or even in the auditory cortex. Localization and isolation of the cause and location of the disease state is difficult with conventional ASSR and ABR techniques because information is lost [52].

The frequency domain representation of the time dependent acoustic wave at the ear, $a_{in}(t)$, is

$$A_{in}(j\omega) = \mathcal{F}\{a_{in}(t)\} \tag{3.1}$$

where $\mathcal{F}$ denotes the Fourier Transform. The acoustic pressure wave at the entrance of the

cochlea is then:

$$A_{co}(j\omega) = H_{tym}(j\omega)\, H_{oss}(j\omega)\, A_{in}(j\omega) \tag{3.2}$$

where H_{tym} and H_{oss} represent the transfer functions describing the transduction of the auditory signals in the tympanic membrane and ossicles of the middle ear. The inner hair cells in the cochlea then *channelize* this into thousands of different channels of progressive frequency. Their outputs along the auditory nerve thus convey a high-dimensional ($N \approx 30,000$) sample of the spectrum

$$[A_{co}(j\omega_0), A_{co}(j\omega_1), ... A_{co}(j\omega_N)] \tag{3.3}$$

for subsequently complex processing in the auditory cortex. Thus if we are interested in measuring physiological benchmarks of audition (as opposed to behavioral and cognitive feedback tests), we must interrogate the auditory cortex response. However, despite recent advances, we are only able to distinguish macroscopic signals generated by the brain when we perform non-invasive, wearable electroencephalography (EEG). The signals recorded at each surface electrode have undergone many non-linear transformations from that cochlear 'bus' through the cortical layers of processing, and the local fields evoked by their neural activations are significantly spread through volume conduction. The EEG signal E_i at any particular surface electrode i:

$$E_i(j\omega) = \sum_{n=1}^{N} c_{in}\ A_{co}(j\omega_n) \tag{3.4}$$

where c_{in} are linear coefficients of the spectral maps on the EEG recording surface (normally the scalp, and here specifically, the ear canal) compounding the cochlear/auditory transfer

function and the observable resulting brain response. Since this mixture does not retain any distinguishable frequency information we must modulate the input signal A_{co}'s spectrum narrowly and apply the techniques of frequency domain system identification [2].

3.1.2 ASSR and EEG

The auditory steady state response (ASSR) is a valuable test because it provides audiologists an assessment of a subject's hearing as a function of frequency. The nature of the stimulus, a repeating set of tones or broadband noise stimulus that is modulated in amplitude by a lower frequency, elicits robust auditory cortex activity which can then be measured in a non-invasive manner from externally placed electrodes. Further, because the steady state auditory stimulus is often presented for extended period of time, on the order of several minutes, the resulting oscillation recorded from the brain are generally subject-state independent. The capability to directly measure the physiology, as opposed to subjective behavioral feedback by an engaged patient, is another major reason for the use of ASSR in auditory assessment of infant and non-responsive subjects [52].

3.1.3 In-Ear EEG

Recent efforts have been made to improve auditory evaluation that utilize precisely engineered stimulation sound profiles to efficiently evaluate hearing across a wide range of frequencies. In-ear EEG has been demonstrated to be an effective alternative to scalp EEG for certain sensing applications, including auditory stimulus response [32, 53, 54]. Furthermore, dry-contact electrodes in the ear canal [113] have proven effective in picking up

skin conductivity in addition to auditory EEG signals [69], permitting extended biomedical use [34, 100] in continuous health monitoring. The main advantages of in-ear dry-electrode EEG over conventional scalp EEG are improved user comfort, reduced body area contact, discretion [94]- [20], and closer proximity to auditory processes [32, 53, 54, 113].

3.1.4 Aim of study

In this study, we aimed to demonstrate the feasibility of a fully integrated in-ear device, capable of presenting auditory stimuli, recording brain activity, and providing enhanced details about the state of a subject's auditory health.

Further, we provide a mathematical model for sound transduction in the human auditory system, laying the foundation for improved localization of auditory dysfunction from EEG measurements.

3.2 Methods

3.2.1 Data and Subjects

Data was gathered for the studies presented here as part of an ongoing study assessing the performance of in-ear electrophysiology as a wearable health sensing platform and an alternative for conventional geometry EEG. Auditory evoked potentials were measured in 32 trials from each ear of 2 healthy subjects, following experimental procedures in Institutional Review Board approved protocols.

3.2.2 Integrated Ear Molds

Shells

Custom-fitted earpieces were fabricated for the subjects' ears using advanced 3D printing techniques and microelectronics assembly (Figure 4.1). Ear impressions used to produce the precisely fitting earpieces were taken by an licensed audiologist and transformed into a 3D digital point clouding using a laser scanner. A standard two-part molding compound used for the custom fitting of hearing aids was injected past the secondary bend of each subject's ear canals and out on to the meatus and concha. The point cloud data was imported into 3D CAD software to create the smooth surface entities of the earpiece and were precisely fitted with hole features for the electrodes to maintain high-density and uniform spacing.

Electrodes

Earpieces were fitted with 17 custom fabricated dry-contact Ag/AgCl electrodes, each with a diameter of 2 mm. A flexible 30 AWG insulated wire was soldered to each electrode and embedded into the lumen of the earpiece. Of the 17 electrodes, 8 serve as in-canal sensors, 8 as concha cavum and cymba sensors, and 1 as a non-sensing driven-right-leg (DRL). Electrodes protrude slightly past the surface of the earpiece and are spaced far enough apart to prevent inadvertent shorting. A small cantilever fitted internally to each electrode provides an adequate spring force to ensure proper electrode-skin contact during wear.

Figure 3.1: The earpieces fabricated from 3D CAD models of the subject's ear shown here embedded with 17 Ag-Ag/Cl electrodes each. A air tube comes through the lumen of the earpieces the provide sound directly the ear canal.

Audio

Auditory stimuli were generated in MATLAB using standard audiology practices. Specifically, steady-state sound stimuli were generated using broadband uniform white noise amplitude modulated 100 percent by low frequencies ranging from 10 to 100 Hz (Figure 3.2). A Blackman window algorithm was utilized to create the amplitude modulation pattern. Sound stimulus was presented to subjects at 75 dB through an air tube for 6 minutes. An air tube sound transducer was used to ensure precise control over stimuli intensity and frequency, and not prevent microphonic interference.

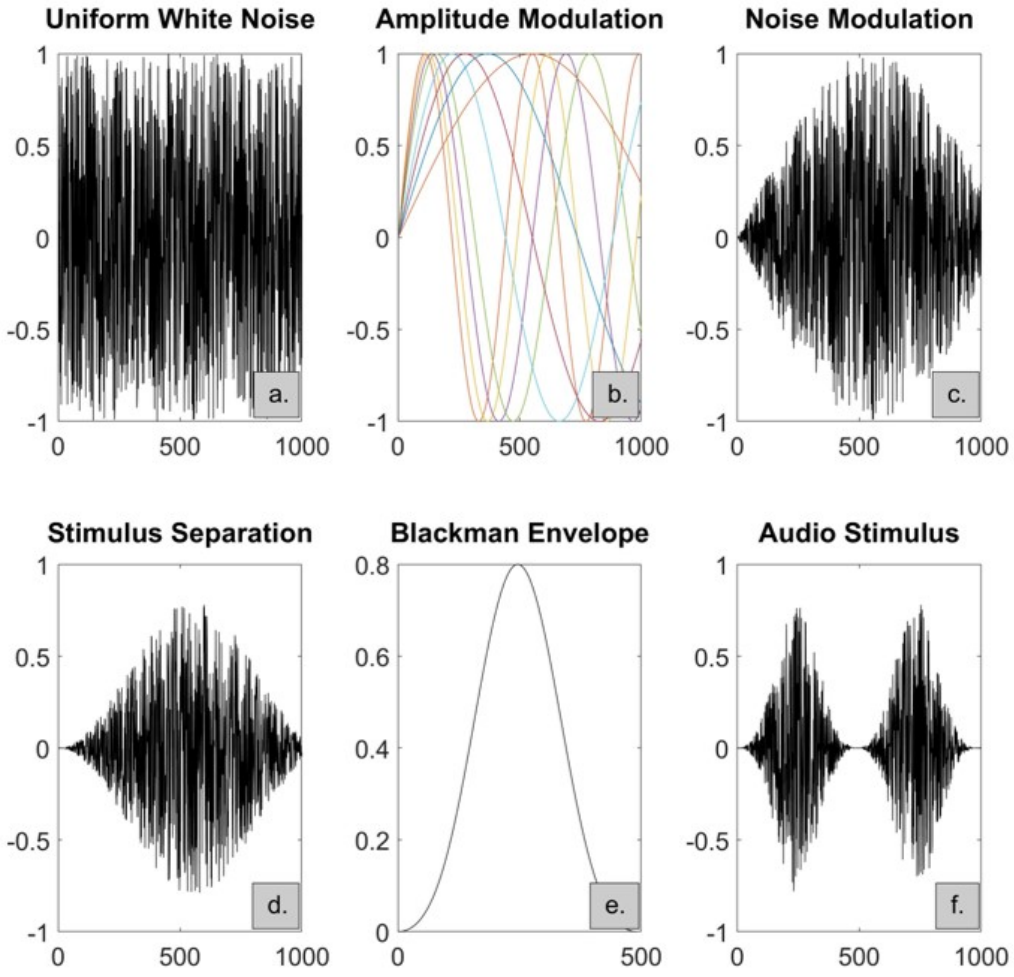

Figure 3.2: Auditory sound stimuli were designed for the ASSR study in a series of steps following the conventional audiology process for audio engineering stimuli.

3.2.3 Acquisition Systems

Real-time measurements of skin conductance activity at multiple sites on the body were managed simultaneously by a low-noise, multichannel biosignal amplifier and analog-to-digital converter (ADC) (Texas Instruments ADS1299) [80]. Four ADC chips were utilized on a custom designed printed circuit board (PCB) capable of 32-channel recording with

on-board filtering, bias drive, and current sources. With 16 custom wet or dry configurable electrodes for the ear and 4 conventional adhesive gel electrodes placed on the palm and fingers, skin conductance was mapped in these areas.

Mapping of skin conductance in the ear canal was achieved by programmatically selecting pairs of electrodes and passing a fixed alternating current across using the ADC's programmable gain amplifier (PGA). A pull-up and pull-down current source was connected to the positive and negative electrodes, respectively, and the resulting voltage measured by the channel amplifier was recorded. The next permutation of the two-electrode configuration was selected and the process was repeated.

3.2.4 Setup of ASSR

Auditory steady state responses from the auditory cortex of test subjects were measured binaurally from the in-ear devices for 8 stimulus frequencies (20, 30, 40, 50, 70, 80, 90, and 100 Hz). Audio was present at 75 dB for exactly 6 minutes per frequency tested. EEG measurements were recorded at a sampling frequency of 1,000 Hz across all 32 channels and streamed wirelessly to the Linux computer. Using EEGLAB, saved data was bandpass filtered from 2 to 100 Hz to remove unwanted high frequency signals and reduce noise. The power spectral density (PSD) of the EEG data was calculated to evaluate the subject's hearing response to the steady state sound stimulus. Peaks in the PSD were generally observed at 60 Hz, representing line noise in North America, at 10 Hz, the EEG alpha band, and the stimulus AM frequency.

3.3 Results

The auditory steady state trials performed at the test frequencies produced characteristic power spectra, as measured by the in-ear EEG. The baseline EEG recording taken with a still subject receiving no auditory stimulus results in a PSD with a strong 60 Hz peak, as expected, but with no other discernible peaks above 20 Hz. The EEG data is band-pass filtered between 2 and 120 Hz, so no spectral information was observed beyond 120 Hz. High amplitudes are observed for frequencies lower than 20Hz, which is normal and expected for EEG because of the strong alpha band (8 Hz–12 Hz) generated in the brain during eye closure, and as a consequence of $1/f$ noise.

When the subject was presented with a 100 Hz amplitude modulated broadband noise stimulus for a sustained 6 minutes, a clear peak in the EEG PSD at 100 Hz is observed (Figure 3.3). The same characteristics peak is seen at 90 Hz in the PSD of EEG recordings from the 90 Hz amplitude modulated auditory stimulus. Note that both 100 Hz and 90 Hz peak are clearly of greater power than the PSD noise level, with the very strong 60 Hz line noise peak shown as a reference. Peaks at 80 Hz and 70 Hz in the EEG PSD, each corresponding to its respective auditory stimulus frequency, display a noticeably diminished peak power, despite the sound level (75 dB) of the auditory stimulus being presented to the subject remaining constant across all stimuli.

An auditory stimulus with amplitude modulation of 60 Hz was forgone for obvious reasons of interference from line noise. Peaks at 50 Hz and 40 Hz in the PSD also clearly showed a measured response from the subjects' auditory cortex. These peaks are clearly

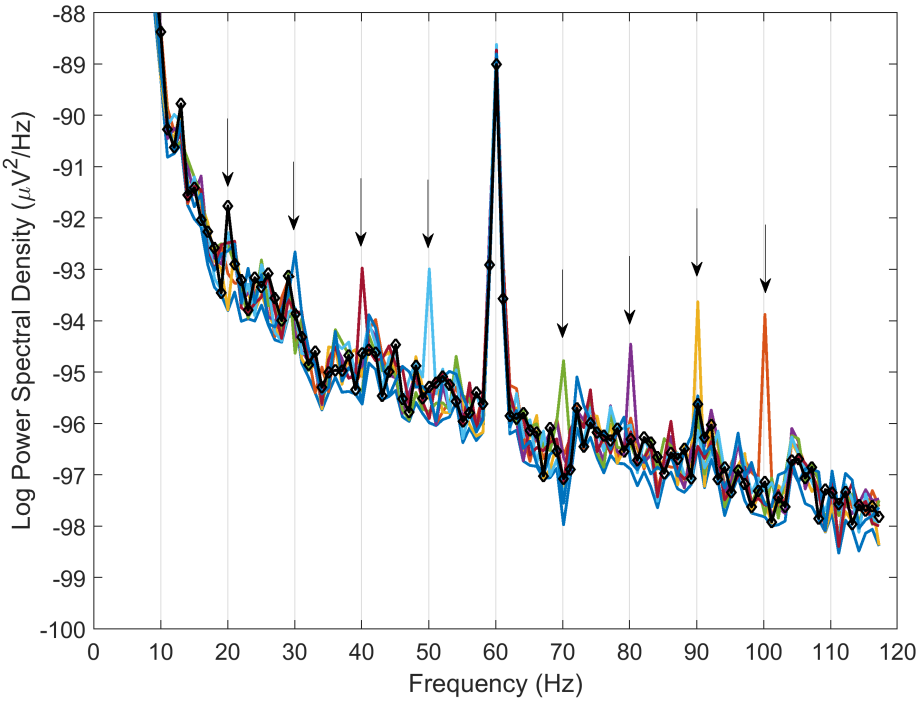

Figure 3.3: The result of the ASSR test frequencies with the top being baseline—no sound presented. Below that is 100 Hz, 90 Hz, 80 Hz, 70 Hz, 50 Hz, 40 Hz, 30 Hz, and 20 Hz responses to amplitude modulated steady state auditory stimuli.

defined above the PSD noise level, but are still less in power than the higher frequency amplitude modulation frequencies. Diminished further in power are 30 Hz and 20 Hz peaks, with the 20 Hz auditory response barely above the PSD noise level. Finally, a 10 Hz amplitude modulation was tested but is not discernible in the results because of high power seen in this low frequency region from the subjects' eyes being closed (alpha waves).

In parallel to in-ear EEG, conventional scalp EEG recordings were made using a commercial 30-electrode headset. PSDs calculated from EEG recordings made during the 40 Hz and 90 Hz auditory stimuli (Figure 3.4) depict a clear peak, above the noise floor

at their respective stimulus frequencies. These scalp EEG results are consistent with the expectations from a conventional ASSR study.

3.4 Conclusion

The EEG PSD shows stability over an extended recording session with different auditory frequencies being presented and the occasional change in subject state. The in-ear EEG is able to consistently measure the steady-state brain activity arising from the subjects' temporal lobes in response to the presented auditory stimuli. This system is able elicit and detect steady-state responses with confidence in the test frequency range of 20 to 100 Hz, producing a PSD with comparable performance and frequency features as a commercial scalp EEG device. The negligible changes observed in overall PSD noise level and consistent amplitude of the 60 Hz peak, used here as a reference, suggests the absence of microphonic interference from the integrate sound transducer and resilience of the system to changes in electrode-skin conditions overtime.

Deconvolving the auditory stimulus amplitude modulation frequency from the resulting EEG PSD peak by diving in the frequency domain would provide useful information regarding the auditory transfer function, as discussed earlier. The perceived linear relationship in ASSR between sound and oscillations in the auditory cortex could be further expanded to account for the dynamics of the tympanic membrane, the middle ossicles, the cochlear transduction, and the middle brain stem latency. In fact, the ASSR tests performed in this study could even elucidate the involvement of the brain stem in the

auditory pathway as seen by the higher power in EEG PSD from amplitude modulation frequencies greater than 70 Hz, a most likely evidence of a middle brain stem latency.

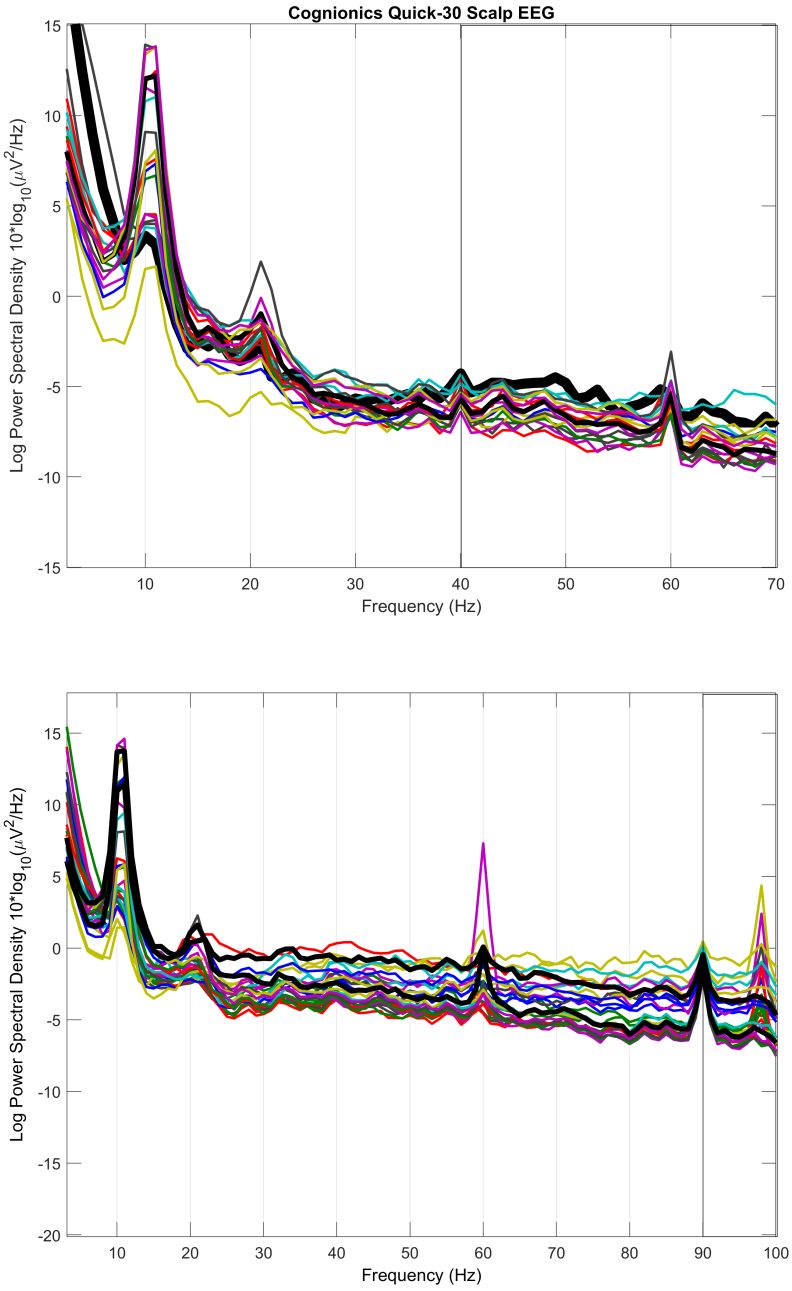

Figure 3.4: Power spectral density (PSD) of scalp EEG recordings made during the ASSR in-ear study using a commercial, Cognionics Quick-30 dry-contact electrophysiology system. Two PSDs are shown here for comparison to the in-ear EEG PSD shown in Fig. 3.3.

Chapter 4

Electrode-Skin Impedance Characterization of In-Ear Electrophysiology Accounting for Cerumen and Electrodermal Response

4.1 Introduction

Conventional electroencephalography (EEG) requires placement of several electrode sensors on the scalp and, accompanied by lead wires and bulky instrumentation, makes

for an uncomfortable experience. Recent efforts in miniaturization and system integration have enabled smaller systems, such as wearable, in-ear EEG devices that are gaining popularity for their unobtrusive form factor. Although in-ear EEG has been demonstrated in recent works, dynamics of the ear and ear canal that directly affect electrophysiological measurements have been largely ignored. Here, we present a quantitative analysis of electrode-skin impedance for dry-contact in-ear EEG that accounts for cerumen (earwax) and electrodermal (sweat gland) response. Custom fitted earmolds with 16 embedded electrodes were developed to map the skin conductance in the ear canal of 3 subjects. In the presence of cerumen, the measured average dry-contact impedance in the ear canal was 86% higher than canals removed of cerumen. Electrodermal activity was also found to play a role in electrode-skin impedance, showing up to 25% decrease in dry-contact impedance in response to tactile stimulation. The better understanding of the dynamics of in-ear conditions serves to improve consistency and accuracy of in-ear electrophysiology.

Electroencephalography (EEG) has long been the standard for measuring electrical signals generated in the brain. It is an indispensable tool used by neuroscientists and medical practitioners for detection of brain states, neurological disorders, motor control and coordination. The applications for EEG both inside the laboratory and in the consumer market continue to grow in our increasingly technology-connected society, but the utility and wider acceptance of this technique is often limited by the uncomfortable scalp electrodes and accompanying wires [32]. The basic setup of the EEG apparatus has not changed in decades, so it comes as no surprise that efforts have been made to improve the comfort and usability of the technique.

Recently, there has been work demonstrating in-ear electrophysiology that offers comparable performance to conventional EEG systems with much improved comfort, wearability, and discretion [19, 53, 54]. These devices often use standard wet electrodes or dry electrodes, which have been validated in use on the scalp or the skin. However, what these studies have neglected to consider is the dynamics of conductance at the electrode-skin interface caused by the unique properties of the ear canal that are not observed elsewhere in the body [34]. Specifically, the prevalence of cerumen (earwax) in the ear canal, humidity, and high density of apocrine glands create a complicated environment for electrodes and merits investigation [52, 100].

The aim of this study was to quantitatively evaluate the skin conductivity in the ear canal and investigate the impact of cerumen on electrophysiological measurements recorded in this environment. A secondary goal was to investigate the effects of systemic galvanic skin response on conductivity in the ear and ear canal. The focus of the study is on dry-contact characterization of the electrodes for long-term use with minimal preparation avoiding the need for cumbersome in-ear gel application. For reference, additional gel-based wet-contact measurements are included.

4.2 Methods

4.2.1 Data and Subjects

Data gathered for these set of studies is part of a larger study evaluating ear-based wearables as alternatives for scalp-based electrophysiology and palm-based galvanic skin

responses. Physiological responses during normal daily activities were measured from subjects in a non-invasive, unobtrusive manner. In this study, skin conductance (SC) measurements were performed over a large portion of the ear canal and concha. Galvanic skin response (GSR) was measured in parallel from conventional palm-based sensors for correlation assessment. In total, data was collected from 24 trials in each ear of 3 healthy subjects.

Subjects were instructed to refrain from cleaning their ears for a minimum of two weeks before experiments were conducted to maintain normal levels of cerumen. In subsequent control experiments, cerumen was removed from the ears of subjects using an over-the-counter earwax removal solution (Murine System) and following the products recommended use protocol.

4.2.2 Ear Molding

Ear impressions were made by a licensed audiologist at Dietsch hearing center (San Diego, CA) for each of the subjects involved in the study. The standard two-part impression material was injected into the ear canal, past the secondary bend, out through the auditory meatus, and onto the concha depression. Three-dimensional laser scanning techniques were used to create editable CAD representations of each subject's ear mold. This enabled the design and fabrication of custom fitted, in-ear electrode sensing devices best suited for comfort, conformability, and electrode-skin contact in each subject (Figure 4.1).

Specialized 21-gauge (Ag/AgCl) electrodes were fitted uniformly in predetermined regions of interest across the ear molds attached to fine gauge, insulated wire in the lumen

of the device. A total of 17 electrodes were fitted with 8 to span the region of the ear canal, another 7 covering the concha cavum, 1 in the concha cymba, and 1 non-recording, driven-right-leg (DRL) electrode, also in the concha cymba. Each electrode sat above the surface of the ear mold over a countersink feature that acted as a well to contain electrolyte gel administered to the electrode-skin interface through embedded micro silicon tubes. Electrolyte gel was kept contained between the surface of each electrode and the skin spanning the opening of the countersink.

4.2.3 Equipment and Measurement

Real-time measurements of skin conductance activity at multiple sites on the body were managed simultaneously by a low-noise, multichannel biosignal amplifier and analog-to-digital converter (ADC) (Texas Instruments ADS1299) [18, 20, 80, 94]. Four ADC chips were utilized on a custom designed printed circuit board (PCB) capable of 32-channel recording with on-board filtering, bias drive, and current sources (Figure 4.2). With 16 custom wet or dry configurable electrodes for the ear and 4 conventional adhesive gel electrodes placed on the palm and fingers, skin conductance was mapped in these areas.

Mapping of skin conductance in the ear canal was achieved by programmatically selecting pairs of electrodes and passing a fixed alternating current across using the ADC's programmable gain amplifier (PGA). A pull-up and pull-down current source was connected to the positive and negative electrodes, respectively, and the resulting voltage measured by the channel amplifier was recorded. The next permutation of the two-electrode configuration was selected and the process was repeated.

4.2.4 Electrode-Skin Contact Configuration

The custom ear electrodes designed for this study are capable of both dry and wet contact with the subject's skin. To assess the effects of contact type on electrode-skin impedance, three contact configurations were tested. For *Dry* contact, dry earpiece electrodes were fitted into the subject's ear. The *Dry-settled* configuration was the same, except impedance measurement was performed after a few minutes. The *Wet* contact configuration involved application of commercial electrode gel (Spectra Gel, Parker Laboratories, New Jersey) either directly to the electrodes or through embedded silicon tubes, depending on the earpiece.

4.2.5 Setup for Galvanic Skin Response Study

The palm and fingers of the human hand is an ideal place to measure the galvanic skin response because of the presence of a high concentration of eccrine sweat glands and the relative convenience of electrode placement. Standard clinical gel electrodes were placed between to palm and first knuckle on the inside face of the index and middle fingers. Skin conductance measurements from the hand served as a suitable comparison to the in-ear measurements for this study.

To achieve a baseline tonic skin conductance level, subjects fitted with hand and ear electrodes were positioned in a relaxed position, not actively engaged in any task or complex thoughts for 10 minutes. After the baseline, a quick pinprick stimulus was administered by the subject at time 0. Skin conductance was measured for up to 4 minutes after stimulus,

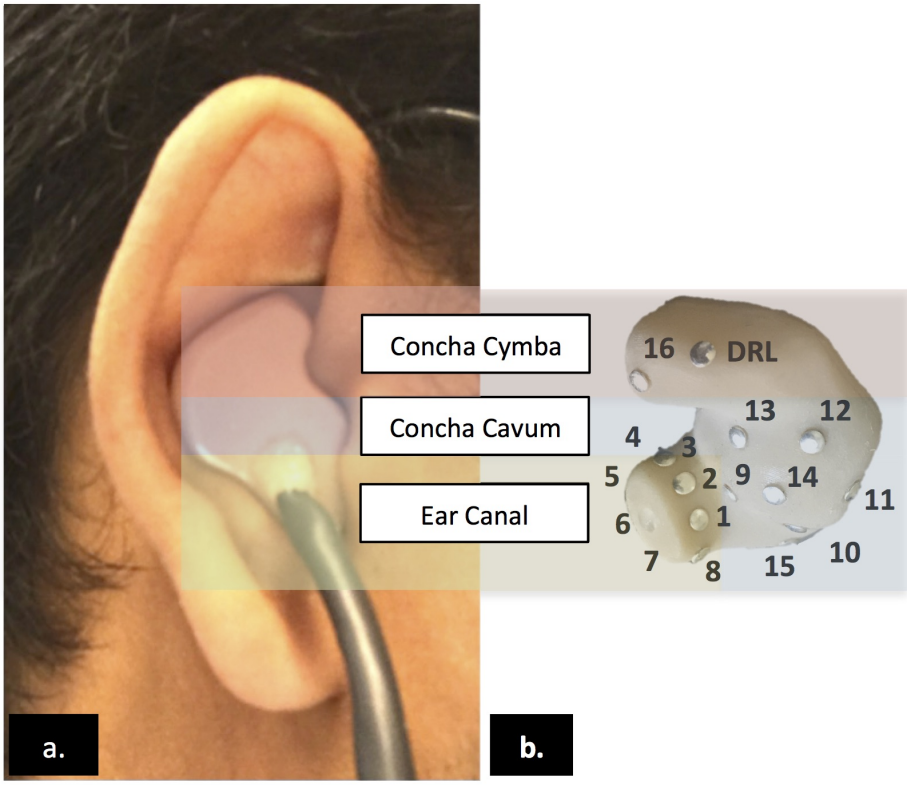

Figure 4.1: Shown on the left is one of the custom earpieces built specifically for the subject pictured. On the right, conductance measurements of different regions of the ear in contact with the earpiece are mapped to corresponding regions on a 3D model.

capturing any phasic change in skin conductance response.

4.3 Results

Impedance values recorded across 16 channels in the ear (Figure 4.3) show marked variation under 3 electrode-skin contact conditions: *Dry*, *Dry-settled*, and *Wet*. Time zero dry contact impedance values in the ear canal (channels 1-8) and concha (channels 9-16) average 1 MΩ and 8 MΩ, respectively. After allowing the dry electrodes to settle in for

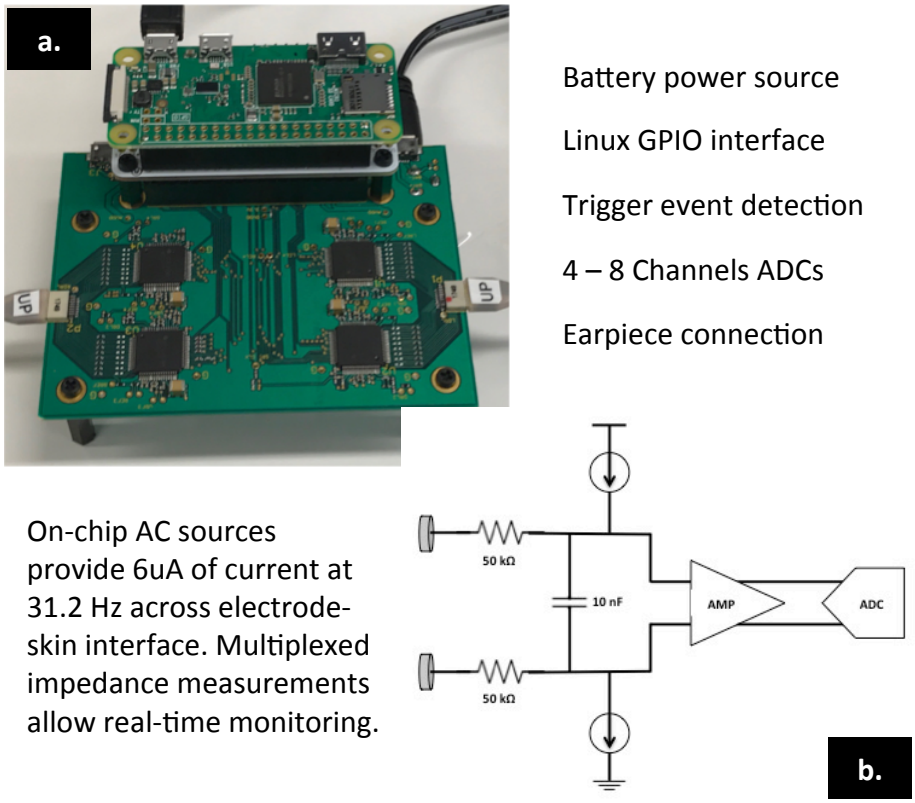

Figure 4.2: Acquisition system and impedance circuit diagram.

2 minutes, dry-contact impedance are reduced by 50% on average across channels. Wet electrode impedance were considerably lower than both dry configurations, as expected, 565 kΩ and 600 kΩ on average in the ear canal and concha, respectively.

Assessment of electrode-skin contact type in the ear based on impedance showed marked difference between the 3 configurations used. Dry contact electrodes in the ear canal (channels 1-8) had an average impedance of 1 MΩ and in the concha (channels 9-16) of 8 MΩ. Repeating this measurement after 2 minutes, produces impedance values 50% lower on average across channels. A known behavior of dry contact electrodes, a few minutes of direct contact with the skin dramatically reduces initial contact impedance. In

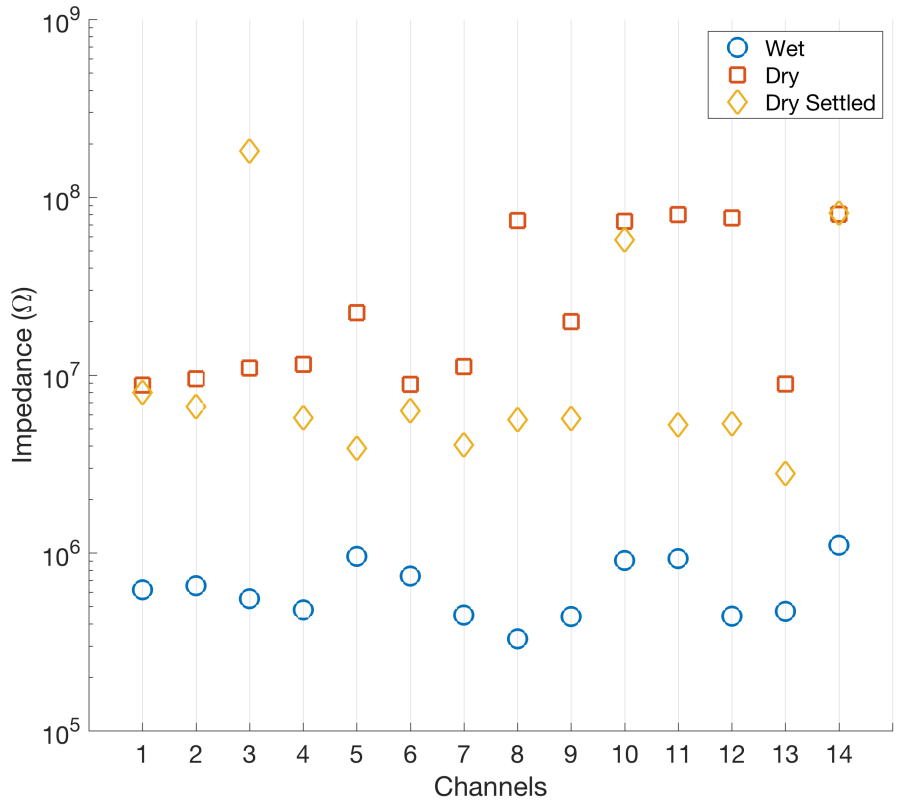

Figure 4.3: Impedance values recorded across 16 channels in the ear show marked variation under 3 electrode-skin contact conditions: *Dry*, *Dry-settled*, and *Wet*.

third configuration, wet contact electrodes, impedance values were significantly lower than both dry configurations, as expected, with ear canal reporting 565 kΩ and the concha 600 kΩ on average.

Alternating current measurements in the ear also showed a considerable difference in electrode impedance when measured in the presence of cerumen and after its removal (Figure 4.4). Dry contact electrodes in a subject's ear with normal cerumen reported impedance values of 4.12 MΩ on average across channels in the ear canal. After removal

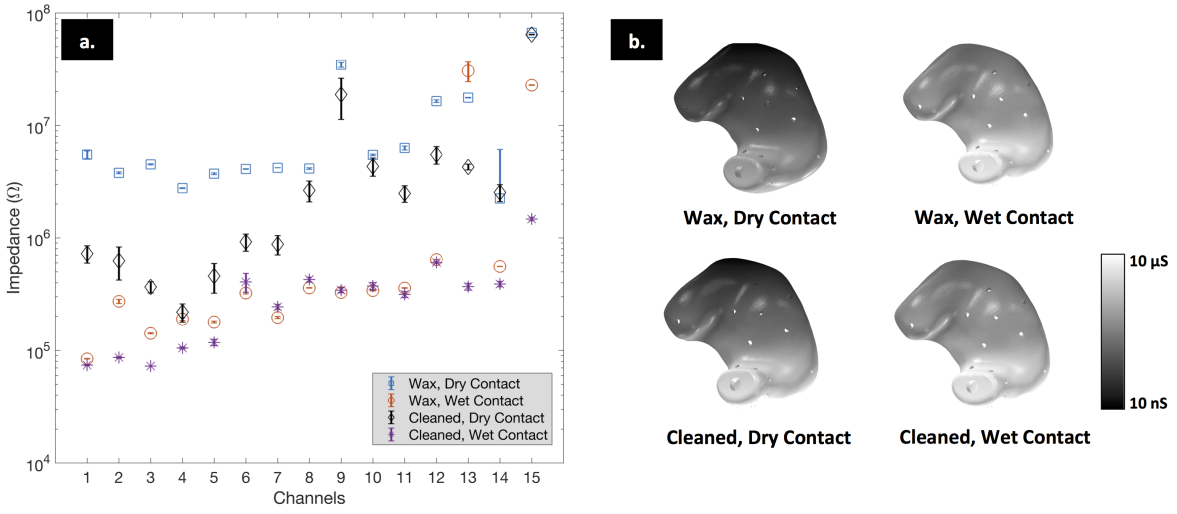

Figure 4.4: Alternating current measurements in the ear also showed a considerable difference in electrode impedance when measured in the presence of cerumen and after its removal.

of cerumen from the subject's ears, impedance decreased by 86.% to 574 kΩ on average. With wet electrodes, removal of cerumen also shows the same trend in impedance reduction. Wet electrodes, with cerumen, measured 213kΩ and without, 112kΩ for a 47% decrease in impedance.

Finally, electrodermal activity in response to a stimulus was observed on the palm and in the ear canal of subjects (Figure 4.5). On the palm, 2 minutes before the stimulus, a steady impedance of 880 kΩ was recorded. One second after the stimulus, a 3.5% impedance decrease is observed, followed by a sharp 47.2% decrease at 2 seconds after stimulus. From the onset to this minimum takes 1 second, and from minimum to when the palm impedance recovers to its normal value takes 5 seconds, for a total electrodermal response lasting 6 seconds. In the ear canal, electrodermal activity was observed, with a response starting

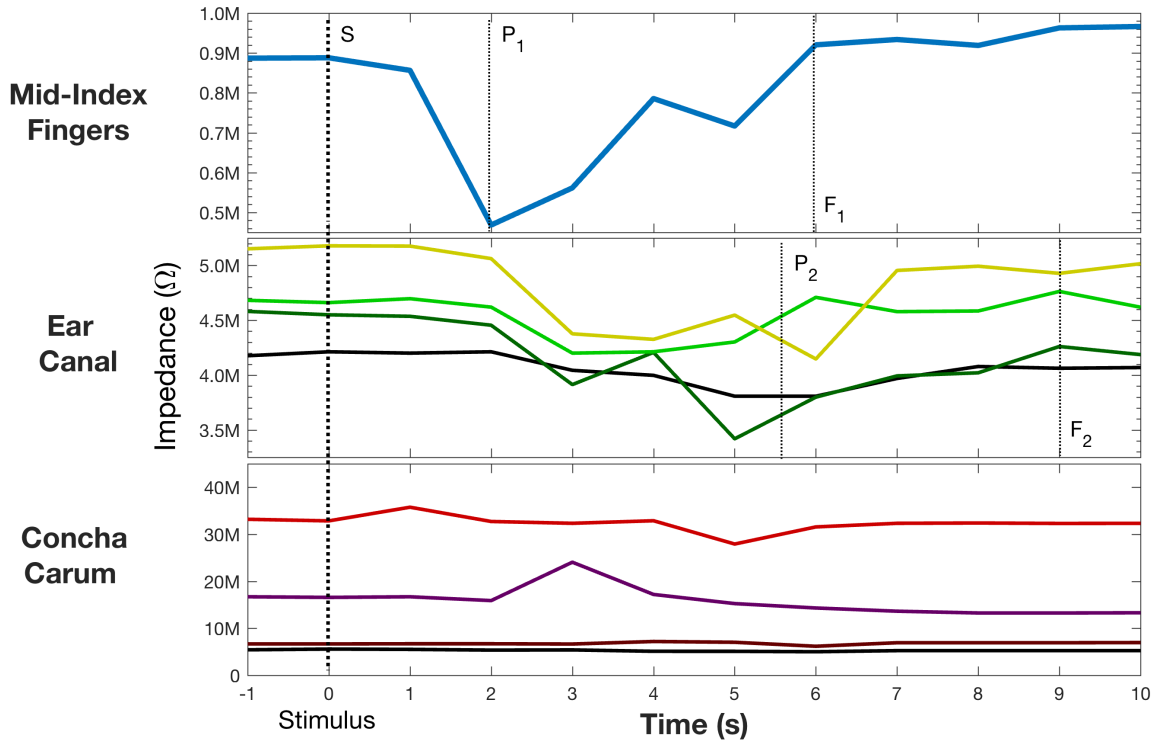

Figure 4.5: Regional dependence of electrodermal response. Skin impedance was monitored on 3 regions of the body: (Top) Middle and Index fingers, (Middle) Ear canal, and (Bottom) Ear Concha.

2 seconds after stimulus and reaching impedance minimum at approximately 5.5 seconds after stimulus, sustained at minimum for a second or more on some channels. Impedance in the ear canal recovers to nearly normal approximately 9 seconds after stimulus, for a total electrodermal response last about 7 seconds. In the concha, the third region monitored during this study, no obvious electrodermal activity was observed.

Onset of electrodermal activity in the ear canal was delayed compared to the palm by at least 1 second. Response duration was also 40% longer in the ear canal compared to the palm and recovery to normal impedance levels was slower and less complete in ear.

The concentration of apocrine sweat glands in the outer ear canal and both apocrine and eccrine sweat glands in the external auditory meatus and concha are the likely the reason for the observed electrodermal activity in the ear. The latency in response and sustained response in comparison to the palm could be explained by the relative distance between the ear and the finger pinprick. Also, the ear canal in these tests is partially occluded, potentially causing an increase in the time taking for sweat to evaportate and humidity to normalize, when compared to the unobstructed hand.

4.4 Conclusion

Investigating the dynamics of the ear and ear canal for ear-based electrophysiology shed light on some of the underlying physiological factors that influence recording. Specifically, for subjects with higher concentrations of cerumen, in-ear electrodes will see considerably greater impedance than for subjects with no or removed cerumen. The concentration and location of cerumen can also vary over time because of the natural flow of the substance from the middle ear to the acoustic meatus, creating a measurement environment far less consistent than the scalp. The in-ear environment has been not been found to be prohibitive to EEG, rather special consideration must be made to account for its dynamics to ensure high signal fidelity and repeatability.

Chapter 5

Scalable Printed Circuit Board Electrode Arrays as Reliable Sensors

5.1 Introduction

To enable continuous, mobile health monitoring, body worn sensors need to offer comparable performance to clinical devices in a lightweight, unobtrusive package. This work presents a complete wireless electrophysiology data acquisition system (weDAQ) that is demonstrated for in-ear EEG with user-generic dry-contact electrodes made from standard printed circuit boards (PCBs). Each weDAQ device supports 16 channels, driven right leg, impedance scanning, 3-axis accelerometer data, local storage, high sampling rates, and adaptable data transmission modes. The weDAQ wireless platform supports body sensor networks (BSN) capable of aggregating multiple biosignal streams (EEG, EMG, EOG, etc.) by supporting simultaneous connectivity of multiple worn devices over the

802.11n WiFi protocol. Each channel achieves 28dB of gain over 70Hz bandwidth with a noise level of 0.92 μVpp and CMRR of 110.8 dB. In-ear and forehead EEG measurements taken from subjects captured modulation of alpha brain activity, EOG characteristic eye movements, and EMG from jaw muscles. The small footprint, performance, and flexibility of the weDAQ lay the foundation for online brain computer interface (BCI) experiments and smart, multimodal biosignal monitoring.

Brain activity monitoring has significant implications for a variety of clinical and health applications, including disease diagnosis [84] and neurofeedback regulation [74]. Recent advancements in brain-computer interface (BCI) technology have enabled a broader range of everyday applications, such as motion control [4] and cognitive status monitoring [44], through the measurement of critical brain biomarkers. Noninvasive sensing using electroencephalography (EEG) continues to be a focus of study in order to increase the applicability and effectiveness of BCI in real-world applications. While full scalp cap systems and wet electrodes are still the de facto norm for EEG recordings, modern EEG systems incorporate dry contact electrodes and a reduced form factor to improve user comfort and wearability [36, 66]. However, due to the bulky and cumbersome setup of scalp-based EEG equipment, real-world EEG applications are limited. In-ear EEG systems originated as a novel sensing modality for capturing brain signals in a discrete, unobtrusive, and comfortable manner [32]. Though a few in-ear EEG systems have been developed [40, 41, 68], several aspects of developing a practical in-ear EEG system remain unresolved. These include a robust, one-size-fits-all, or user-generic, electrode-ear interface, a high-throughput acquisition system in a compact package, and distributed, wireless transmission capability

for untethered binaural measurement [32].

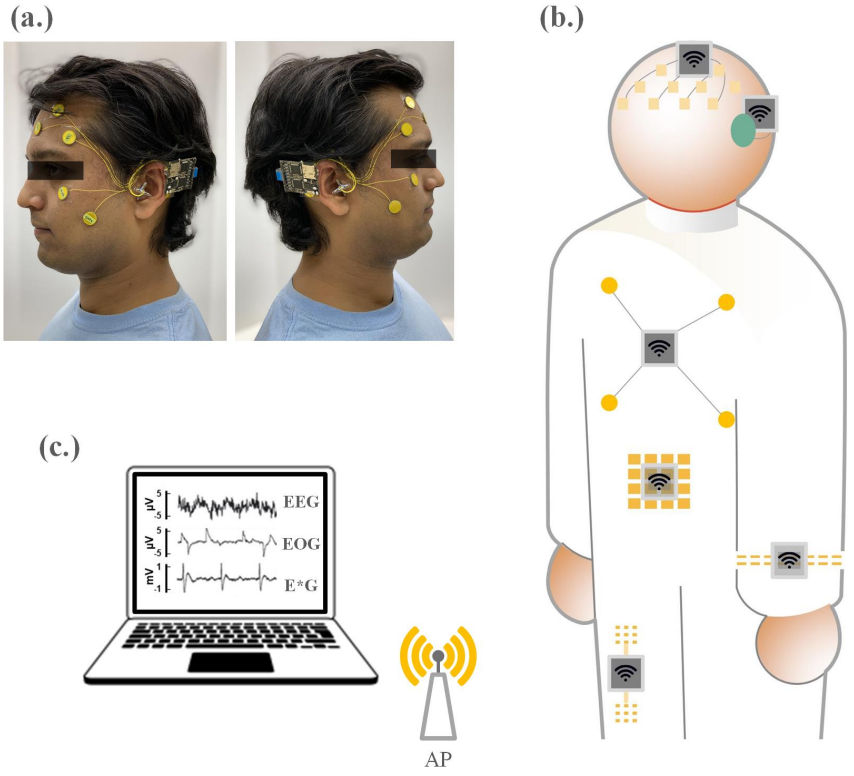

Figure 5.1: Overview of weDAQ system and user-generic PCB electrodes shown on-body. (a) Subject wearing 32, in-ear and surface, dry PCB electrodes supported by 2 weDAQs, (b) concept of multimodal weDAQ body sensor network (BSN), (c) live streaming of multiple weDAQ device streams.

The present study describes a fully wireless in-ear EEG data collection device (weDAQ) equipped with user-generic dry-contact electrodes. In this demonstration, we achieved binaural, high-density EEG sensing using 32 in-ear electrodes, 6 forehead EEG, 2 EOG, and 2 EMG electrodes, all constructed from standard printed circuit boards (PCBs) (Figure 6.1). Different types of brain-related electrophysiological signals were used

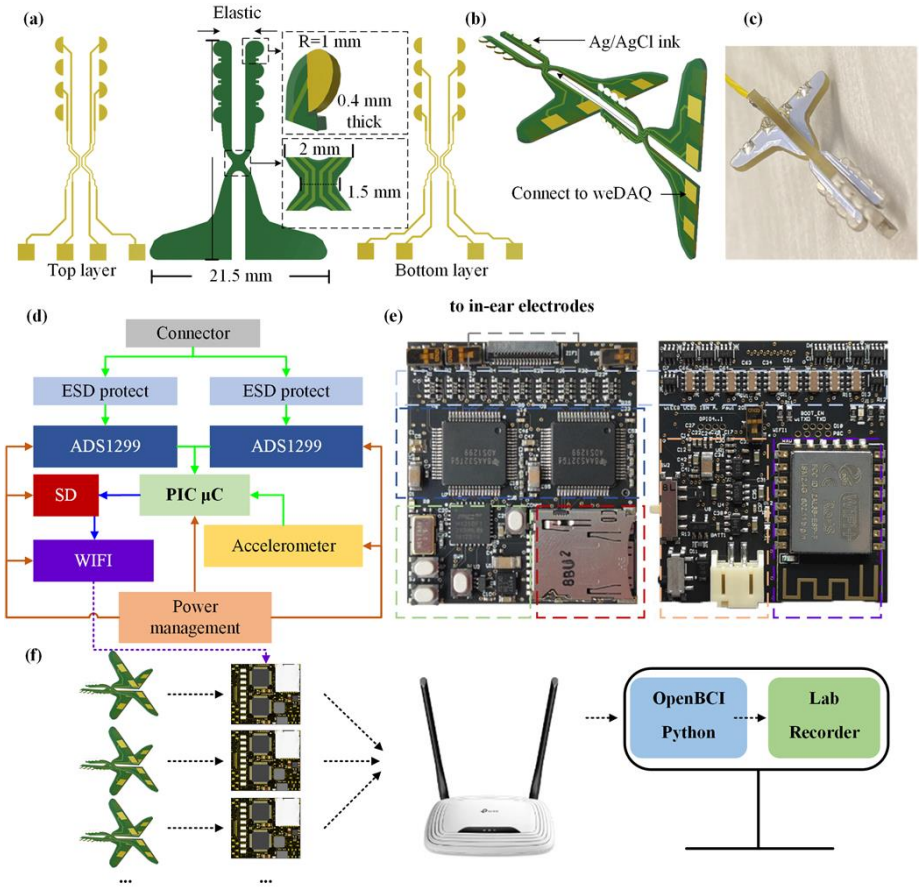

Figure 5.2: Detailed diagram of user-generic dry PCB electrodes, the weDAQ system, and the wireless streaming network.

to characterize the in-ear electrophysiology acquisition system across multiple users in a binaural arrangement, including electrode-ear impedance, alpha modulation, eye movements and blinks, and facial muscle activity. The high electrode count in each ear offers potential benefits for motion artifact mitigation with independent component analysis techniques and a higher spatial resolution for mapping brain activity and electrodermal activity (EDA) across the ear canal [40, 55, 56, 69]. The higher electrode-skin impedance experienced by in-ear EEG devices also necessitates the very high input-impedance and sub-microvolt

range noise floor of the amplifier utilized in the weDAQ, providing a platform for further investigation of in-ear physiology [3, 69, 89].

Each weDAQ provides 16 electrophysiology channels sampled up to 2 kHz. Comprised of low-cost, commercially available components and a system circuit we make open source (github.com/apaulworks), the weDAQ, and accompanying electrodes, were designed to be accessible and scalable (Figure 6.6). The corresponding firmware and software written for this system has provisions for smart sensing and data compression. Multiple weDAQ devices will simultaneously connect and stream data on the 802.11n WiFi protocol when configured in BSN mode. The data transmission interval, packet size, and local storage usage can then be algorithmically controlled to optimize for signals of interest, bandwidth, and battery life. Continuous or intermittent impedance scanning modes are provided to automatically identify and switch off poor contacting electrodes which generate noise and waste power. In addition, the reference and driven ground channels on each weDAQ can be configured on-the-fly to any electrode in the array to optimize sensitivity and change referencing scheme [69].

5.2 Hardware Methods

5.2.1 In-Ear and Surface Electrodes

The in-ear apparatus was comprised of the 2 planar "crocodile" PCBs, mated together to form the 3D structure shown in Figure 6.6a,b. Each crocodile has 8 semi-circular silver (Ag) plated electrodes with a diameter of 2 mm and a 0.4 mm thickness.

The jaws of the crocodile are made flexible because of the narrow design of the helix (Figure 6.6a) to fit snugly and comfortably inside the ear canal. Following mating, the 3D apparatus is connectorized with 30-AWG wire, coated with Ag-AgCl ink (Creative Materials, MA, USA), and cured at 80°C for 30 minutes. For this work, the coating was made on each semi-circular Ag contact separately to form 16 individual electrodes, but it is possible to short all neighboring channels on a flange with a wider ink coating, to form 4 larger effective electrodes. The Ag electrodes can also be bleached directly with oxidizing chlorine solution to form the AgCl layer, if ink is unavailable. Surface disk electrodes had a diameter of 1 cm and were made using the same PCB process as the in-ear electrodes. Ag-AgCl ink was deposited onto the disk's Ag electrode contact and cured at 80°C for 60 minutes [48]. Again, 30 AWG wires were used for connectorizing and the back of the electrode was coated in polyimide (this gives gives the Ag electrode a yellow appearance) to insulate the connection. Surface disk electrodes were attached to the skin using transparent double-sided medical tape (3M, MN, USA).

5.2.2 Electrode Placement

As mentioned above, electrodes were placed into each ear using 2 crocodile 3D in-ear devices. The 4 flanges of each in-ear device were oriented in superior, anterior, inferior, and posterior directions. On the forehead, 6 dry contact disk electrodes were positioned in the F7, F8, Af7, Af8, Fp1, and Fp2 standard EEG locations (Figure 6.1). An additional 2 disk electrodes were positioned under the left and right eye for EOG and 2 more disk electrodes were positioned on the left and right masseter jaw muscles [79]. Reference

and DRL electrodes were placed on the right mastoid bone behind the ear. Wire routing was manage behind the ear and long the temples with the same transparent double-sided medical tape used to mount the disk electrodes and weDAQ.

5.2.3 Data Acquisition

The weDAQ device incorporates new and existing system designs [68,69,85] centering around the ADS1299 bioinstrumentation IC (Texas Instruments, TX, USA). A 32-bit PIC microcontroller (MircroChip, AZ, USA) coordinates over an SPI bus with 2 8-channel ADS1299 ICs, an ESP8266 WiFi module (Espressif, China), an accelerometer, and the SD flash memory. Power comes from a 3.7V reachargeable LiPo battery which has a smaller footprint than the weDAQ.

Device configurations are sent over the air from the a python user interface to each weDAQ device. A referential (pseudo-monopolar) montage was configured with a single reference shared by all 16 channels per board. Gain was set to the maximum of 24 and common-mode bias sensing was performed on select channels before driving the dedicated driven right leg (DRL) electrode. Sampling was performed at 2kHz and data was both streamed live over the WiFi connection through an access point (AP) to lab streaming layer (LSL) and saved locally on the SD card. Data streamed into LSL was processed, visualized, saved in real-time on a laptop connected to the same AP. We utilized 3 weDAQ boards to support the binaural and facial electrodes, using 42 out of 48 available channels.

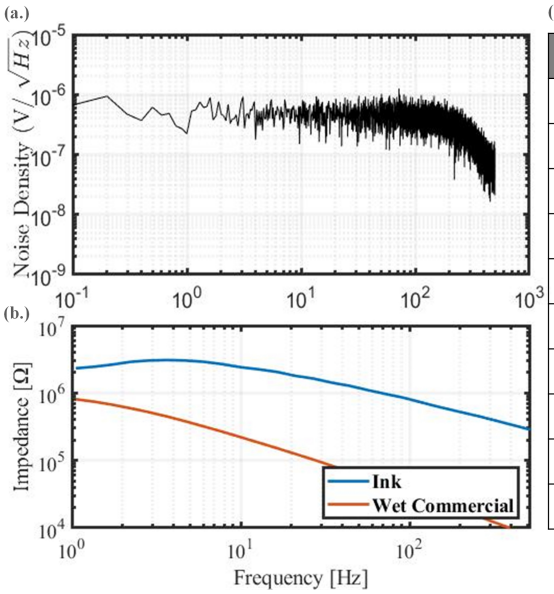

(c.)

Parameter	Measured Value
Noise	0.92 μV_{rms} (70-Hz BW)
CMRR	110.8 dB
SNR	46.0 dB
Sampling Rate	2000-Hz
Maximal Gain	28 dB
Transmit Rate	54 Mbps
SD Write Speed	512 kbps
Bandwidth	Up to 72 Mbps
Power Consumption	50 - 660 mW
Reliability	< 0.001% drop

Figure 5.3: (a) The input-referred noise spectra for the weDAQ measured with maximum device gain of 24 at 1kHz sampling. (b) Electrode impedance spectroscopy (EIS) crocodile dry contact Ag-AgCl electrodes. (c) Performance metrics for the weDAQ.

5.3 Experimental Methods

5.3.1 Experiment Protocol

Three categories of electrophysiological signals were recorded using the weDAQ, crocodile in-ear PCB electrodes, and surface disk PCB electrodes, as shown in Figure 6.1a: EOG, EMG, and EEG. For EOG, the subject was asked to blink at a 1 Hz metronome beat for 1 minute. Subsequently, EOG of eye movements was measured in 5 cycles, where for each cycle, the subject directed their eye gaze from center to left then back to center, center to right then back to center, center to up then back to center, and center to down then back to center, taking 1 beat to move gaze and another the hold before the next

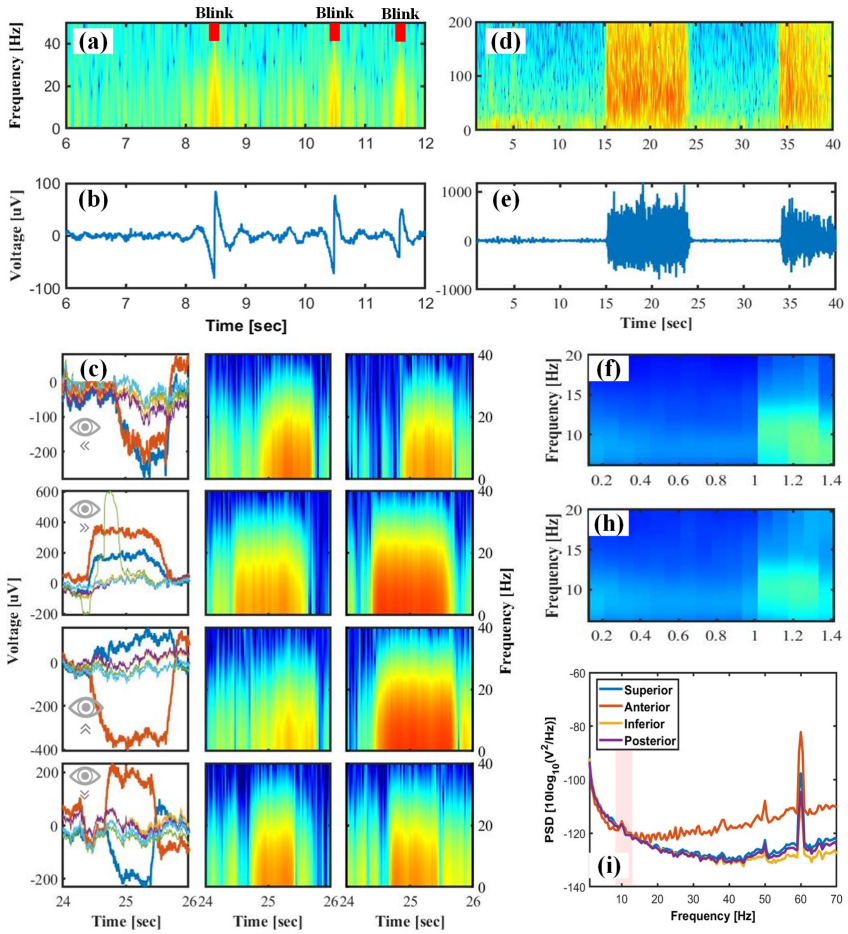

Figure 5.4: (a) Eye-blinks spectrogram, (b) Eye-blinks time-series, (c) 4 eye movements; 4 in-ear channels (sky blue, gold, purple, and green), 1 forhead EOG (blue), and 1 facial EOG (orange); spectrograms for in-ear (left) and facial (left), (d) EMG spectra, (e) EMG time-series, (f) EEG alpah.

movement. For EMG, jaw clenching was measured during 10 seconds periods of clenching followed by 10 seconds of relaxing the jaw, for 2 cycles. Finally, for the EEG study, alpha band modulation was recorded with the subject instructed to keep their eyes closed and relaxed for 1 minute, followed by an eyes open period. The study was approved by the UC

San Diego Institutional Review Board.

5.3.2 Data Analysis

Data was imported from LSL into EEGLAB [23] for analysis and bandpass filtered using channel-specific cutoff frequencies suitable for each electrophysiological modality. Spectrograms were generated for EOG channels during eye blinks and during jaw clenches from EMG channels. For eye movement analysis, in-ear channels were compared to forehead and facial EOG channels by measuring the voltage deflection seen at the onset and offset of the eye movement in the time series data; spectrograms were also generated for this comparison. Alpha modulation in the brain was also compared using spectrograms taken from in-ear EEG channels and forehead EEG channels a few minutes before the onset of the eyes closed task. Out of the 32 in-ear channels, only 25 lasted for the duration of the testing because of breakage in the fine gauge connection wire or delamination of the Ag/AgCl ink during insertion. To simplify data processing for the alpha modulation study and accommodate for the few offline channels, electrodes along each of the four flanges of the crocodile device where averaged to produce 4 effective channels per ear along the abscissa and ordinate axes.

5.4 Results

In benchtop testing of the weDAQ system, noise measured over 70-Hz bandwidth was 0.92 μV_{rms} (Figure 5.3a). Maximal gain achieved from the ADS1299 chips was confirmed

to be 28 dB and common-mode rejection (CMRR) was measured at 110.8 dB (Figure 5.3c). During multiple device streaming over WiFi, the weDAQ system was able to support at least a 2 kHz sampling rate with less than 0.001% measured data drops. The WiFi streaming bandwidth in close proximity to the access point (6 feet away) was confirmed to be 54 Mbps with 2 devices on the BSN. Power consumption during normal full streaming mode for each weDAQ was measured to be approximately 660 mW and as low as 130 mW during the dark-mode, in which the WiFi connection is present but data transmits intermittently, writing mostly to the local SD card. During low-power mode, which saves data locally and transmits over WiFi only on demand, used approximately 50 mW of battery power.

The user-generic dry PCB electrodes where performant to impedance, noise, and mechanical fit criteria throughout the experiments for in-ear and forehead and facial placements. Electrode impedance spectroscopy (EIS) was performed on-body for these Ag-AgCl electrodes and compared to wet commercial Ag-AgCl electrodes (Figure 5.3b). Results reveal DC impedance of 2.2 MΩ which linearly slopes downward from 2 MΩ at 10 Hz down to approximately 300 kΩ at 50Hz. EIS performed on used electrodes after the electrophysiology experiments showed no significant change. Electrode performance for both in-ear and disk PCB electrodes remained consistent over multiple days with physical contact between the electrode and the skin matching fiducial markers. Some electrode failed because of improper handling at the wire connection or at the ink cap when storing the devices.

Eye blinks were detected from both in-ear and forehead EEG channels, as well as

on the EOG facial channels (Figure 5.4). Figure 5.4a shows the characteristic spectral signature of eye blinks and the corresponding time series data recorded. Eye movements were also detected from in-ear and facial EOG channels with varying success. Specifically, facial EOG channels detected eye movements robustly seen as the blue and orange time traces in column 1 of Figure 5.4c. Leftward eye movements created synchronous negative voltage deflection and rightward created synchronous positive voltage deflections across both in-ear and facial disk electrodes. Upward eye movements created apposing deflections in the facial EOG electrodes and the opposite apposing deflection was seen for downward eye movement, as expected. Upward and downward eye movements however, were not detected well from in-ear channels as seen in row 3-4 of column 1 Figure 5.4C.

Muscle activity from the jaw was detected robustly from the facial EMG electrodes, but was also picked up across some forehead and in-ear channels for intense muscle clenching events. Figure 5.4d,e show the characteristic spectral signature for intense muscle activity at 15 and 35 seconds and relaxed jaw from 0 to 15 and 25 to 35 seconds. The corresponding time series data for the EMG activity shows strong electrical activity measured up to 1 mV.

Alpha modulation was observed well from both in-ear and forehead EEG electrodes. Figure 5.4f shows the spectrogram for in-ear electrodes and Figure 5.4h for the forehead electrodes during eyes open until time 1 and eyes closed after. Figure 5.4i presents the power spectral density of all 4 in-ear electrodes from the right side, where a clear peak in the alpha band is detected during the eyes closed task.

5.5 Conclusion

We presented a low-profile user-generic and portable in-ear EEG instrumentation device with versatile capabilities for biosensing over the body. The electrodes were easy to make and reliable for measurements of in-ear and forehead EEG, EOG, and EMG. The weDAQ system captured biosignals from multiple devices at a high sampling rate and data quality that may be comparable to clinical systems. We were able to capture in-ear EEG signal during an alpha modulation task, as well as, eye blinks and eye movements. Facial electrodes also captured eye movements and muscle activity from the jaw very well, as was expected. This work paves the way for high-channel count, fast sampling body sensor networks for mobile health sensing and intelligent closed-loop brain computer interfaces.

Chapter 6

A Versatile In-Ear Biosensing System and Body-Area Network for Unobtrusive Continuous Health Monitoring

6.1 Introduction

Brain activity monitoring has significant implications for a variety of clinical and health applications, including disease diagnosis [84] and neurofeedback regulation [74]. Recent advancements in brain-computer interface (BCI) technology have enabled a broader range of everyday applications, such as motion control [4] and cognitive status monitoring [44], through the measurement of critical brain biomarkers. Noninvasive sensing using

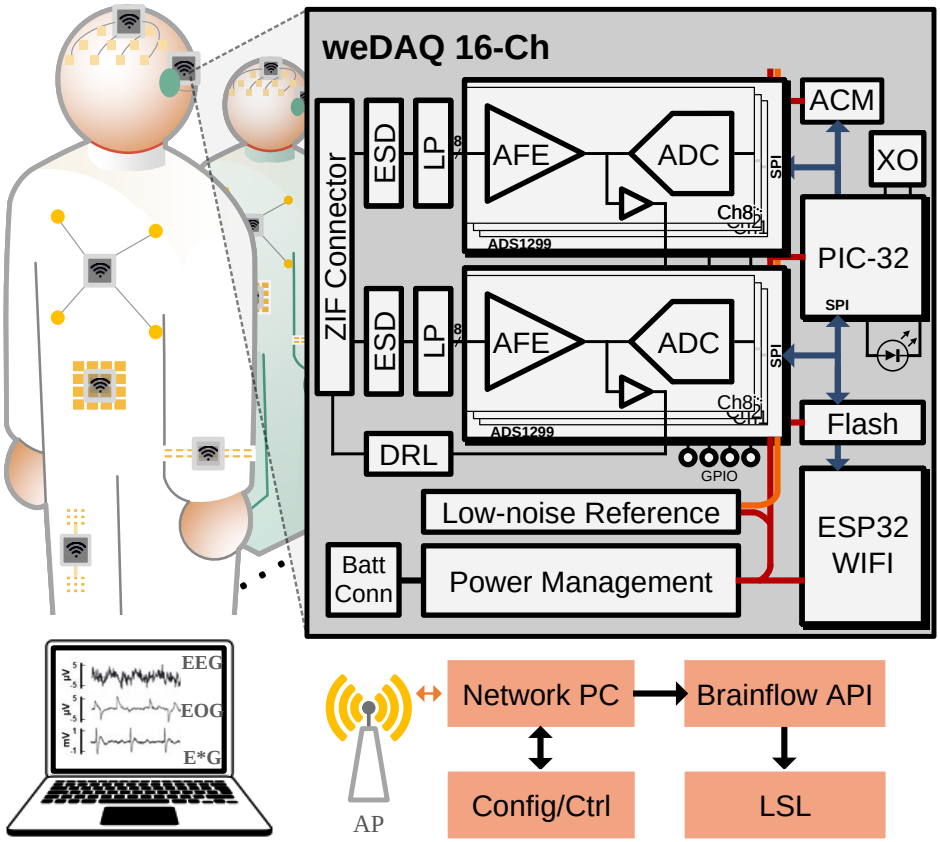

Figure 6.1: Wireless electrophysiology data acquisition (weDAQ) in the setting of a body-sensor network where multiple devices are deployed onto a subject or cohort of subjects.

electroencephalography (EEG) continues to be a focus of study in order to increase the applicability and effectiveness of BCI in real-world applications. While full scalp cap systems and wet electrodes are still the de facto norm for EEG recordings, modern EEG systems incorporate dry contact electrodes and a reduced form factor to improve user comfort and wearability [36, 66]. Notable open-source efforts have put forward cost-effective acquisition platforms for scalp-based EEG brain monitoring [64, 99]. However, scalp-based

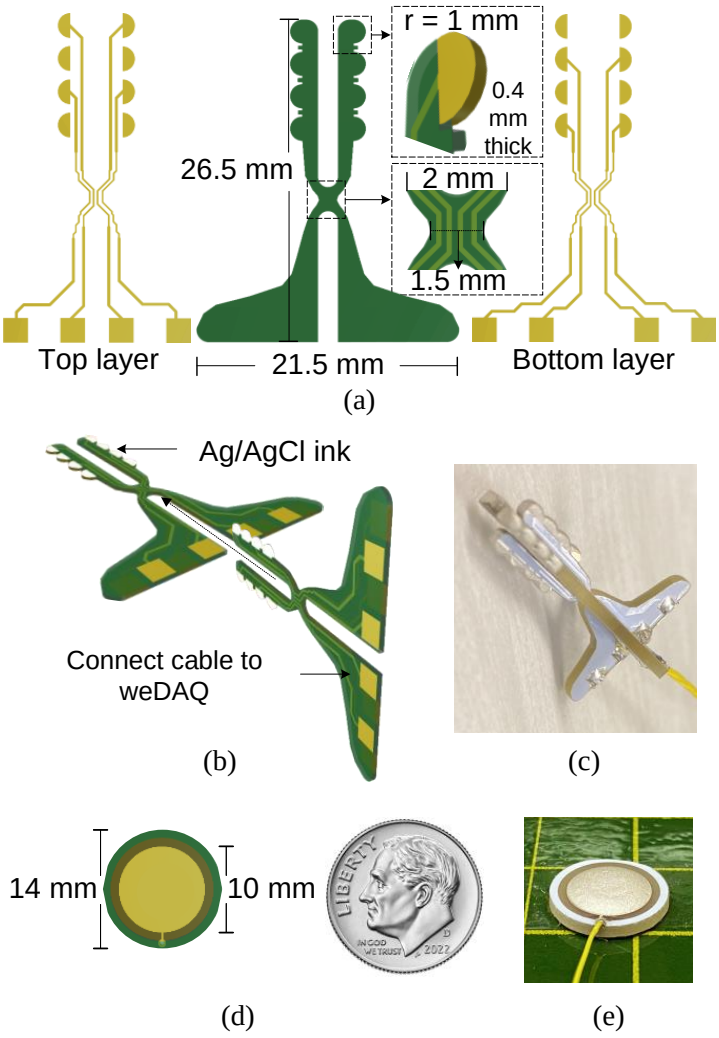

Figure 6.2: (a) Copper metal layers and overall dimensions of the "crocodile" PCB in-ear electrode. (b) Assembly of 2 8-electrode crocodiles into a single, 16-electrode 3D in-ear apparatus with 4 flanges. (c) Fully assembled crocodile with Ag plated electrodes coated with a cured layer of Ag/AgCl

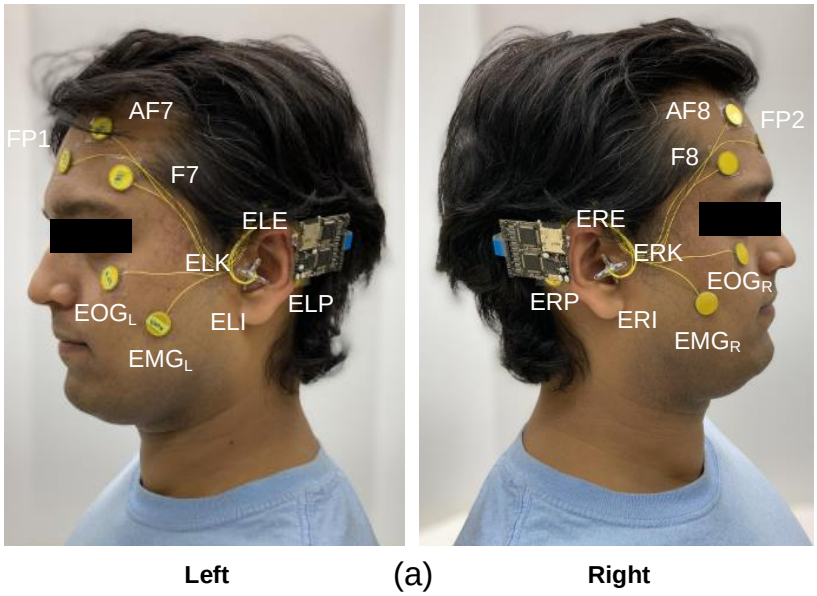

Figure 6.3: An untethered subject wearing in-ear crocodile and surface disk electrodes supported by 2 weDAQs.

EEG equipment still tends to be bulky and sensing from other locations on the body remains challenging as options for open-source wearable electrophysiology sensors is limited.

In-ear EEG originated as a novel sensing modality for capturing brain signals in a more comfortable, discrete, and unobtrusive manner from regions of the ear and ear canal [31, 53]. These in-ear systems can take various forms but in general have been comprised of custom-fitted earpieces embedded with dry-contact electrode materials with wired [42, 54, 113] and wireless [38, 40, 68] acquisition hardware, or as a generic fitting earpiece, with wired [10, 95] and wireless [32, 59] acquisition hardware. Only a limited number of in-ear systems however, have demonstrated a complete wearable earpiece with a wireless interface [41, 47, 87].

In-ear sensing is currently limited by electrode count, scalability of manufacturing, and intricate earpiece preparations [82]. A higher electrode count in each ear would offer potential benefits for motion artifact mitigation with independent component analysis techniques and a higher spatial resolution for mapping brain activity and electrodermal activity (EDA) across the ear canal [40,55,56,69]. In-ear sensing has also been limited by the sampling rate available from wearable acquisition systems [61]. Certain electrophysiological experiments such as those involving fast event-related potentials (ERPs) [77], like the auditory brainstem response (ABR) [14], or biosignals with large bandwidths such as those found in electromyogram (EMG) [57], have not been demonstrated well from in-ear or wearable sensing systems, in part, because they necessitate a faster sampling rate (i.e. > 500 Hz) than those found conventionally in wearable recorders [3]. The utilization of in-ear sensing in mobile applications has been constrained by insufficient bandwidth of the wireless protocols implemented limiting measurement resolution. Expansion of in-ear sensing to accommodate additional sensing modalities and to enable incorporation into larger body-worn recording networks necessitates a high bandwidth wireless network. Despite recent efforts for around-the-ear sensing [45] and hearable platforms [83], open-source electrode designs and acquisitions hardware for in-ear monitoring still do not exist.

Therefore, the following aspects of a practical in-ear EEG system remain underdeveloped: (1) a low-cost, scalable one-size-fits-all earpiece with high density dry electrodes, (2) a configurable, high-throughput acquisition system in a compact package, and (3) wireless transmission capability for untethered binaural measurement at high sampling rates.

The present study describes a wearable, wireless electrophysiology data acquisition

system (weDAQ) with body-area network (BAN) capability (Fig. 6.1) and novel user-generic dry-contact electrodes (Fig. 6.2) that together, create a versatile, open-source platform for in-ear and on-body health sensing. Here we expand the hardware characterization and electrophysiology demonstration for this platform, originally introduced in [71]. To achieve low-cost, scalable electrodes, standard printed circuit board (PCB) manufacturing was utilized to produce a high electrode-count earpiece. The same process provides dry disk electrodes for surface measurement on the skin [19, 20]. To enable untethered monitoring, the weDAQ was designed with a high bandwidth wireless interface, small form factor, and configurable, low-noise ADCs to support fast sampling of multiple channels. Associated firmware for the system provides flexible configuration of multiple weDAQs on the BAN including transmission modes, dynamic rerouting of reference and driven-right-leg (DRL) active ground channels, and electrode-skin impedance monitoring. The electrodes were characterized using electrochemical impedance spectroscopy (EIS) and the wireless acquisition hardware was characterized for input-referred noise, data transmission reliability, and power consumption. Finally, a series of electrophysiological studies were conducted across multiple users including binaural in-ear and facial monitoring (Fig. 6.3) of eye blinks, alpha modulation, eye movements, and jaw muscle activity. An exercise electrophysiology study was also conducted capturing electrocardiogram and electromyogram from multiple subjects simultaneously. Performance of the platform is compared to state-of-the-art and commercial systems. In an effort to lower the barrier to entry for new research on in-ear sensing and wearable health monitoring, all hardware and software is provided as open-source (github.com/apaulworks) with compatibility to other open-source electrophysiology

tools such as, OpenBCI, EEGLAB, and NeuroPype.

The paper is organized as follows: Section II further describes the user-generic in-ear and surface PCB electrodes, the weDAQ system, and the wireless body-area network. Section III provides the specifications for the electrophysiological experiments. Section IV presents hardware performance results for the weDAQ and the electrodes, and experimental results from the electrophysiology recordings. Section V provides a discussion for the design choices made and comparison of results from this work to the state-of-the-art. Section VI summarizes the work and lists the next steps for development.

6.2 Hardware Implementation

6.2.1 In-Ear and Surface Electrodes

The in-ear apparatus is comprised of 2 planar "crocodile" PCBs, mated together to form a 3D structure shown in Fig. 6.2(a,b). Each crocodile has 8 semi-circular silver (Ag) plated electrodes with a diameter of 2 mm and a 0.4 mm thickness. The jaws of the crocodile are made flexible because of the narrow design of the waist to fit snugly and comfortably inside the ear canal. Following mating, the 3D apparatus is connectorized with 30-AWG wire, coated with silver/silver chloride (Ag/AgCl) ink (Creative Materials, MA, USA), and cured at 80°C for 30 minutes (Fig. 6.2(c)). The coating can be made to extend over neighboring semi-circular Ag contacts on each jaw of the crocodile to create larger effective electrodes, and a mask can be used for each Ag contact to form up to 16 individual electrodes. The Ag electrodes can also be bleached directly with oxidizing chlorine solution

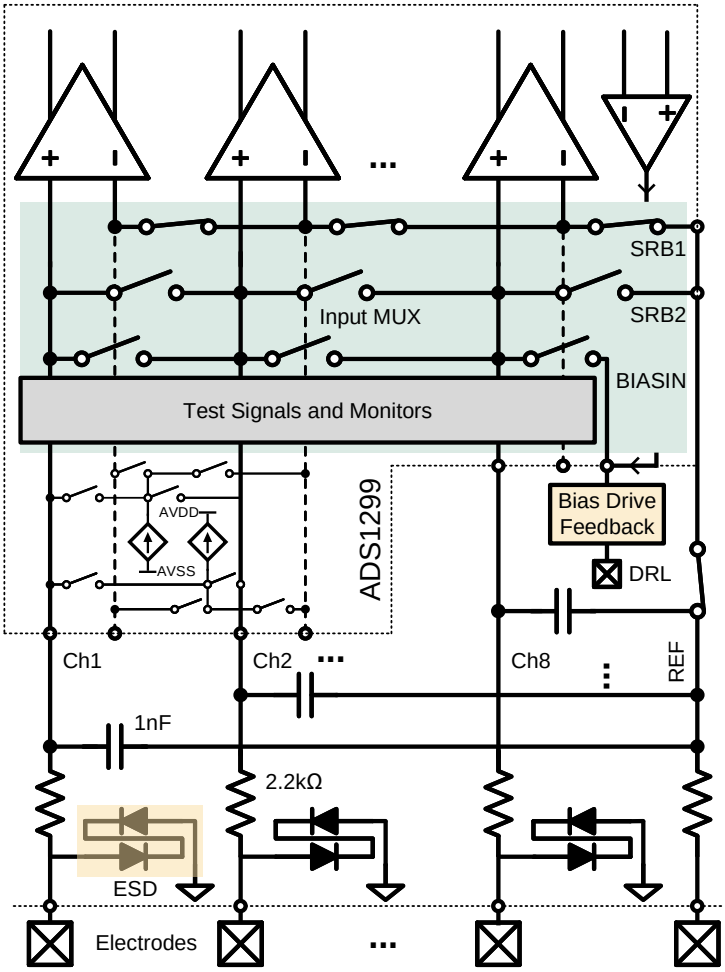

Figure 6.4: Analog front-end of the weDAQ accommodating a variety of electrophysiological signals using both dry and wet electrodes, incorporating electrostatic discharge (ESD) protection, patient-protection resistors, and a low-pass filter.

to form the AgCl layer, if ink is unavailable [48]. Surface disk electrodes had a diameter of 1 cm and were made using the same PCB process as the in-ear electrodes (Fig. 6.2(d)). Ag/AgCl ink was deposited onto the disk's Ag electrode contact and cured at 80°C for 60 minutes [48]. Again, 30 AWG wires were used for connectorizing and the back of the

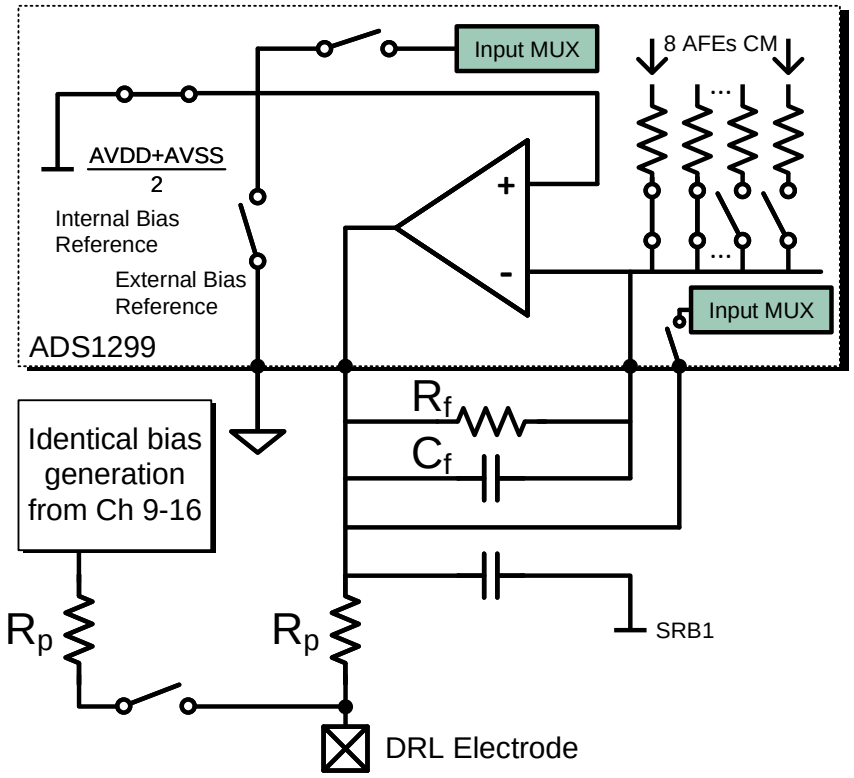

Figure 6.5: Diagram of the driven right leg (bias drive) circuit. The DRL electrode contacting the body is driven by either an internal or externally provided reference voltage and by the common-mode signals from select channel amplifiers.

electrode was coated in polyimide (this gives the Ag electrode a yellow appearance) to insulate the connection (Fig. 6.2(e)). A clear, non-conductive lacquer or potting epoxy can be used to provide insulation and strain relief to the electrode-wire interface. Surface disk electrodes were attached to the skin using transparent double-sided medical tape (3M, MN, USA).

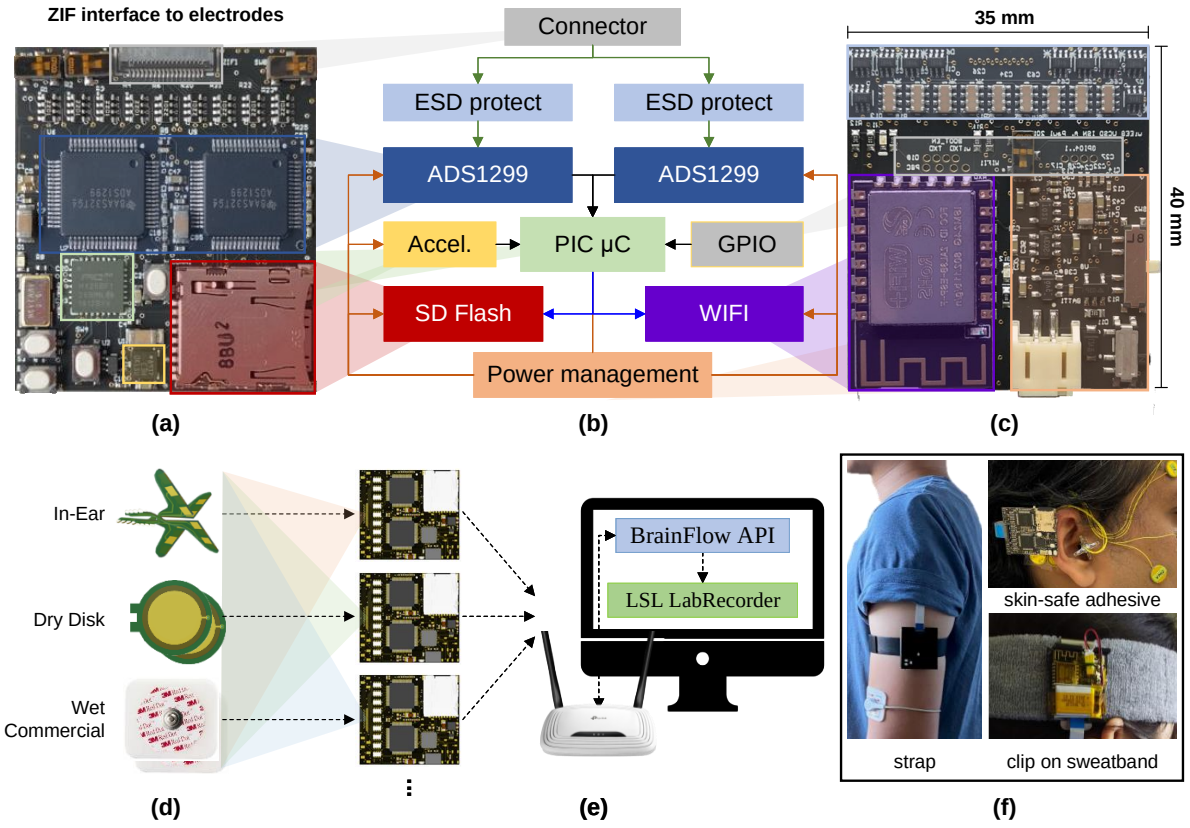

Figure 6.6: (a) Top side of weDAQ board. (b) System-level weDAQ block diagram. (c) Bottom side of weDAQ board. (d) Multiple electrode types shown to be compatible with weDAQ including Ag/AgCl in-ear, dry silver flat disk, and wet commercial.

6.2.2 weDAQ System Overview

Sensors are interfaced to the weDAQ on a 18-pin locking zero insertion force (ZIF) connector compatible with standard flat flexible cable (FFC) ribbons (Fig. 6.1). To match the number of sensing channels available, 16 pins map to the inputs of the analog front-ends (AFE), 1 pin is a dedicated reference (SRB1), and the last pin is reserved as a dedicated body ground, (DRL). As shown in Fig. 6.4, each sensing path features a TVS diode array

for ESD protection, a 2.2-kΩ resistor for patient protection, and a 1-nF capacitor for a low-pass filter with f_c = 72.5 kHz. The dedicated reference and DRL paths also have the patient protection resistor. The DRL features feedback circuit depicted in Fig. 6.5 is optimized for on-body electrophysiological sensing [69], where R_f is 1 MΩ and C_f is 1nF. The DRL electrode can be driven by a summing of the common-mode signals from any combination of channel AFEs on a single ADS1299 chip by configuring the *bias sensing* register or by both chips by closing the on-board switch between the 2 bias drive paths (Fig. 6.5).

The dedicated reference electrode can be disconnected from the SRB1 path by an on-board switch to allow for remapping of the reference to a different electrode from amongst those connected on the sensing input paths. This remapping of electrodes is accomplished by leveraging the highly configurable input MUX of the ADS1299 to switch any sensing electrode to a new reference using the SRB2 path in the event of poor contact or disconnection of the original dedicated reference, or for the case of measurement re-referencing. The same can be done for the remapping of the body ground from the dedicated DRL electrode to any of the available sensing electrodes using the BIASIN path, at the cost of giving up a sensing channel. The weDAQ system further utilizes the current sources and switches available on each channel of the ADS1299 to enable in-band electrode-skin impedance measurements before and after recordings, or out-of-band impedance scanning during sustained recordings. On-chip test signals and monitors can also be configured by software to calibrate and optimize the weDAQ for a given sensing application and user input.

The weDAQ device incorporates new and existing system designs [68, 69, 85] with commercial off-the-shelf (COTS) components in a small 3.5-cm x 4.0-cm 4-layer PCB centering around the ADS1299 bioinstrumentation IC [80] (Texas Instruments, TX, USA) (Fig. 6.6(a-c)). A 32-bit PIC microcontroller (MicroChip, AZ, USA) coordinates over an SPI bus with 2 8-channel ADS1299 ICs, an ESP8266 WiFi module (Espressif, China), an accelerometer, and the SD flash memory (Fig. 6.6(b)). Power comes from a 3.7-V rechargeable LiPo battery which is regulated to produce a 3.3-V digital supply and the 2 analog supply rails, +2.5 V (AVDD) and -2.5 V (AVSS). The weDAQ can support up to a 2-kHz sampling rate across its 16 channels.

6.2.3 Body Area Network

The weDAQ devices use the 802.11n WiFi protocol to stream data. Firmware for the weDAQ system was implemented carefully on both the PIC mircocontroller and the ESP WiFi module to allow scalability of the BAN network (Fig. 6.6(e)), enhance reliability of the data recording, and optimize power consumption for a given application. The code base utilizes, in part, open source resources including OpenBCI and Brainflow. There are 3 main operating modes for weDAQ which are orchestrated by the custom firmware that include a half-duplex streaming mode (*HDX mode*), a unidirectional streaming mode (*simplex (SPX) mode*), and a non-transmit, local-write only mode (*dark mode*). The main advantages of the SPX mode are significant power savings by duty-cycling the WiFi modem and a decreased percentage of data drops at higher transmission rates. The SPX mode checks intermittently for new user configurations sent from a PC while providing continuous

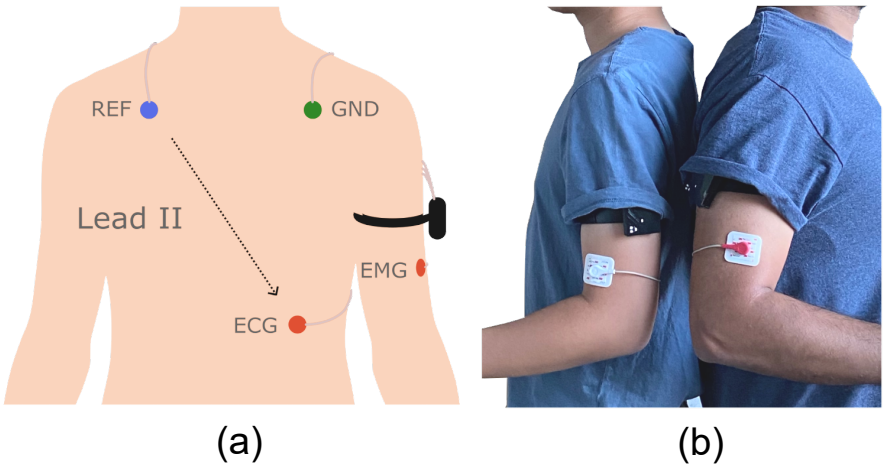

Figure 6.7: (a) Diagram of electrode placement for Lead-II ECG and Biceps EMG. (b) Photo taken during exercise experiment of 2 independent, untethered subjects being monitored by weDAQ devices on armbands as they are seated, standing, and lifting heavy objects.

monitoring of the subject.

6.3 Experimental Methods

6.3.1 Physiological Recording Configuration

Device configurations were sent over the air from a Python user interface to each weDAQ device. A referential (pseudo-monopolar) montage was configured with a single reference shared by all 16 channels per board (Fig. 6.4). Gain was set to the maximum of 24 and common-mode bias sensing was performed on select channels before driving the dedicated DRL electrode (Fig. 6.5). Sampling was performed at 1 kHz and data was both

streamed live over the WiFi connection through an access point (AP) to lab streaming layer (LSL) and saved locally on the SD card. Data streamed into LSL was processed, visualized, and saved in real-time on a laptop connected to the same AP. We utilized multiple weDAQ boards to support the binaural, facial, chest, and arm electrodes.

6.3.2 Electrode Placement

As mentioned above, electrodes were placed into each ear using 2 crocodile 3D in-ear devices. The 4 flanges of each in-ear device were oriented in superior (ExE), anterior (ExK), inferior (ExI), and posterior (ExP) directions. The flanges here serve to prevent the crocodile from ingressing too far into the ear canal but care should be taken when inserting anything into the ear canal. Optionally, as shown in Fig. 6.2(c), the 4 neighboring electrodes on each of the 4 jaws of the apparatus are shorted by the ink, creating a larger electrode surface area.

On the forehead, 6 dry contact disk electrodes were positioned in the F7, F8, Af7, Af8, Fp1, and Fp2 standard EEG locations (Fig. 6.3). An additional 2 disk electrodes were positioned under the left and right eye for EOG and 2 more disk electrodes were positioned on the left and right masseter jaw muscles [79]. Reference and DRL electrodes were placed on the right mastoid bone behind the ear. Wire routing was managed behind the ear and along the temples with the same transparent double-sided medical tape used to mount the disk electrodes and weDAQ.

Subjects were fitted also with wet Ag/AgCl electrodes (3M RedDot) on the chest in the standard Lead II ECG configuration with the reference placed near the right collar

bone, the sensing electrode at the bottom left edge of the ribcage, and the driven ground placed at the subject's left collar bone (Fig. 6.7). Another electrode was placed on either the right or left biceps, depending on the subject's preference. On the same arm, an additional weDAQ was mounted comfortably with an adjustable band to support the body measurements.

6.3.3 Experiment Protocol

Electrophysiological signals were recorded from 3 subjects using the weDAQ, crocodile in-ear PCB electrodes, and surface disk PCB electrodes, which included electroocoulogram (EOG), EMG, and EEG. For EOG, subjects were asked to blink at a 1 Hz metronome beat for 1 minute. Subsequently, EOG of eye movements was measured in 5 cycles, where the subjects directed their eye gaze from center to left then back to center, center to right then back to center, center to up then back to center, and center to down then back to center, taking 1 beat to move gaze and another to hold before the next movement. For EMG, jaw masseter muscle activity was measured during 10-second periods of clenching followed by 10 seconds of relaxing the jaw, for 2 cycles. Finally, for the EEG study, alpha band modulation was recorded with the subjects instructed to keep their eyes open and relaxed for a short period, followed by an eyes-closed period of 1 minute. The study was approved by the UC San Diego Institutional Review Board.

To further demonstrate the BAN, an exercise study was also performed with 2 independent, untethered subjects, each fitted with a weDAQ and electrodes on the chest and arm for mobile ECG and EMG (Fig. 6.7). First, a resting Lead II ECG was recorded as

a baseline from both subjects simultaneously. Then, subjects were instructed to perform a short interval of a high-intensity exercise while their ECG was again recorded simultaneously. Muscle activity was tracked from the biceps while the subjects were instructed to lift, hold, and release a heavy object at timed intervals. Finally, EMG was monitored as the subjects rapidly lifted and released a heavy object to track burst muscle activity.

6.3.4 Data Analysis

Data was imported from LSL into EEGLAB [23] for analysis and bandpass filtered using channel-specific cutoff frequencies suitable for each electrophysiological modality. Spectrograms were generated for EOG channels during eye blinks and during jaw clenches from EMG channels. For eye movement analysis, in-ear channels were compared to forehead and facial EOG channels by measuring the voltage deflection seen at the onset and offset of the eye movement in the time series data; spectrograms were also generated for this comparison. Alpha modulation in the brain was compared using spectrograms taken from in-ear EEG channels and forehead EEG channels leading up to and during the onset of the eyes-closed task. To accommodate for channel offset and other variability, recordings from the 4 electrodes along each of the four flanges of the crocodile device were averaged.

6.4 Experimental Results

6.4.1 DAQ

In benchtop testing, the weDAQ performance was characterized across multiple sampling rates up to a maximum 4 kHz per channel. Input-referred noise (IRN) was measured with channels shorted to a reference DC voltage in a 10-second interval and with the electrodes connected (Fig. 6.8(a)). As expected for the configurable gain settings (i.e. 1, 2, 4, 6, 8, 12, and 24), IRN decreased with increasing gain across all tested sampling rates, and increased for a given gain setting as sampling rate increased (Fig. 6.9(a)). Over a 1000-Hz bandwidth (2 ksps) and gain 24, an IRN of 0.52 μV_{rms} and IRN density of 23 $nV/\sqrt{Hz}$ were measured. Signal-to-noise ratio (SNR) was calculated to be 98.1 dB at a sampling rate of 2 kHz and gain of 24 for a 10 Hz input test signal (Table 6.1). Common-mode rejection ratio (CMRR) with a 60-Hz input signal was calculated to be 110.8 dB on average across channels and dynamic range (DR) was calculated to be 105.5 dB (Fig. 6.9(b)), for the same sampling rate and gain. A summary of weDAQ benchmark results are provided in Table 6.1.

6.4.2 BAN

During testing of the BAN, we observed the WiFi network was able to support at least 4 weDAQ devices simultaneously streaming a total of 64 channels at 2 ksps. Reliability of the wireless stream was assessed using packet timestamps and parity checking to detect data drops or corruption. Fig. 6.9(c) shows the percentage of drops seen over a 1-hour

Table 6.1: weDAQ Performance Benchmarks

Data Acquisition	
Sampling Rate	2000 Hz
Maximal Gain	27.6 dB
Noise (1000-Hz BW)	0.52 μV_{rms}
SNR	98.1 dB
CMRR	110.8 dB
Dynamic Range	105.5 dB
Power	0.171 W
Wireless	
Transmit Rate	54 Mbit/s
SD Write Speed	512 kbit/s
Energy Efficiency	5.5 nJ/bit
Reliability	$< 0.005\%$ drop

period of streaming for the 3 transmission modes. During SPX streaming at 2 ksps, data drops averaged 0.005 %, and 0.75 % for HDX mode. In comparison, the dark mode which uses the wireless network only intermittently, experienced less than 0.0006 % data loss or corruption. The WiFi streaming bandwidth in close proximity to the access point (10 feet away) was confirmed to be 54 Mbps with the 4 streaming devices on the network.

Power consumption showed only a gradual increase with respect to sampling rate from 250 Hz to 4 kHz for all transmission modes (Fig. 6.9(d)). Each of the transmission modes showed a distinct separation in power usage across sampling frequencies. Specifically, at the 2-kHz sampling rate, HDX mode used the most power with 0.447 W (27.9 mW/ch), SPX mode in the middle with 0.224 W (14.0 mW/ch), and dark mode using the least with 0.171 W (10.7 mW/ch).

6.4.3 Electrodes

The user-generic dry PCB electrodes were performant to impedance, noise, and mechanical fit (i.e. remaining in good contact with the skin) criteria throughout the experiments for in-ear and forehead and facial placements. Electrochemical impedance spectroscopy (EIS) was performed on-body for these Ag/AgCl electrodes and compared to wet commercial Ag/AgCl electrodes (Fig. 6.8(b)). Results reveal DC impedance of 2.2 MΩ which linearly slopes downward from 2 MΩ at 10 Hz down to approximately 300 kΩ at 50 Hz. Phase for the ink electrodes starts close to 0° at DC compared to the commercial electrode at -30°. Both electrodes demonstrate a phase that decreases (becomes more negative) with respect to frequency, reaching approximately -60° and -80° at 500 Hz for ink and commercial, respectively.

EIS performed on ink electrodes after multiple days of electrophysiology experiments showed no significant change. Electrode performance for both in-ear and disk PCB electrodes remained consistent for the approximately 1-hour experiments performed on several days. Placement and alignment of the electrodes over the multiple days of experiments was aided by the use of fiducial markers on the subjects' skin to maintain comparable recording conditions between days and subjects. Some electrodes failed because of improper handling at the wire connection or at the ink's surface when storing the devices.

6.4.4 Eye Blinks and EMG

Eye blinks were detected from both in-ear and forehead channels, as well as, on the facial channels. Fig. 6.10(a) shows the recorded time series data and corresponding spectral signatures characteristic of eye blinks. Muscle activity from the jaw was detected robustly from the facial EMG electrodes, but was also picked up across some forehead and in-ear channels for intense muscle clenching events. Fig. 6.10(b) shows the corresponding time series data for the EMG activity shows strong electrical activity measured up to 1 mV and the characteristic spectral signature for intense muscle activity at 15 and 35 seconds and relaxed jaw from 0 to 15 and 25 to 35 seconds.

6.4.5 Alpha Power Modulation

Alpha modulation was observed well from both in-ear and forehead EEG electrodes. Fig. 6.11(a) shows the spectrogram for in-ear electrodes and Fig. 6.11(b) for the forehead electrodes during eyes open until 1 minute and eyes closed after. Power in the alpha band is observed to rise shortly after the subject closed their eyes at 1 minute. In-ear EEG and forehead EEG channels had on average equivalent power both before and after the 1 minute mark.

6.4.6 EOG of Eye Movement

Eye movements were also detected from in-ear and facial EOG channels with varying success. Specifically, facial EOG channels detected eye movements robustly seen as the

blue and orange time traces in Fig. 6.12. Leftward eye movements created synchronous negative voltage deflection (Fig. 6.12(a)) and rightward created synchronous positive voltage deflections across both in-ear and facial disk electrodes (Fig. 6.12(b)). Upward eye movements created apposing deflections in the facial EOG electrodes (Fig. 6.12(c)) and the opposite apposing deflection was seen for downward eye movement (Fig. 6.12(d)), as expected. However, upward and downward eye movements were not detected well from in-ear channels (Fig. 6.12(c,d)).

6.4.7 Multi-Subject Exercise

During exercise monitoring, the weDAQ BAN clearly captured ECG and EMG signals from the subjects simultaneously throughout the study. In Fig. 6.13(a), the resting ECG waveform shows a distinct difference in resting heart rate between the 2 subjects. Subject 1, in black, had a R-R interval of 1.10 s for a resting heart rate of 54.5 bpm compared to Subject 2, in blue, with a R-R interval of 0.83 s for a resting heart rate of 72.3 bpm. During exercise, Subject 1 presented a heart rate 108 bpm and Subject 2 presented a 96 bpm heart rate. The P-QRS-T signatures were clearly presented and differentiable from the live ECG data stream. In Fig. 6.13(b), during sustained lift-and-hold activity, Subjects 1 and 2 both presented clear muscle activity seen in the EMG recording. In the burst lift-and-release activity, Subject 2 muscle activity was clearly detected and smaller in duration and amplitude than their lift-and-hold EMG recording. Subject 1 reported to having to use less muscle power to lift and release the object than during the hold activity, which could explain the diminished EMG activity seen here.

Table 6.2: Comparison with Electrophysiology Recording Systems

	[68]	[41]	[47]	[96]	[38]†	[90]	[40]	This work
Channels	32	64	2	16	8	8	-	16
Sampling Rate	1000 Hz	1000 Hz	1000 Hz	-	250 Hz	500 Hz	1000 Hz	2000 Hz
Input Range	4.5 V_{pp}	0.1 V_{pp}	0.8 V_{pp}	0.9 V_{pp}	-	-	0.3 V_{pp}	4.5 V_{pp}
Bandwidth	100 Hz	1-500 Hz	0.5-100 Hz	0.5-100 Hz	100 Hz*	-	350 Hz	1000 Hz
IRN	1 μV_{rms}	1.6 μV_{rms}	0.4 μV_{rms}	0.27 μV_{rms}	-	1 μV_{rms}*	<1 μV_{rms}*	0.52 μV_{rms}
IRN Density	100 $nV/\sqrt{Hz}$	70 $nV/\sqrt{Hz}$	57 $nV/\sqrt{Hz}$*	26 $nV/\sqrt{Hz}$	-	-	-	23 $nV/\sqrt{Hz}$
ADC Bit Resolution	24 bits	15 bits	11 bits	10 bits	24 bits	24 bits	24 bits	24 bits
Wireless	WiFi	Bluetooth	BCC‡	BCC‡	Bluetooth	WiFi	Bluetooth	WiFi
Power	-	46 mW	12.3 mW	16.1 mW	-	-	-	228.1 mW
Energy / Sample	-	1.4 µJ	61.8 µJ	10.1 µJ	-	-	-	7.1 µJ
Ref Channel MUX	Yes	-	No	No	Yes	-	-	Yes
Grounding	Active	Passive	Passive	None	Active	None	-	Active
Impedance Scanning	Yes	Yes	No	No	Yes	Yes	Yes	Yes

Values for each system presented in this table represent the configurations and metrics demonstrated in the corresponding references. It may be possible these systems have different performance metrics under different configurations but the values from the referenced works are taken as-is.
*Estimated value. †Reference used the OpenBCI Cyton board [64]. ‡ Body-coupled communication (BCC) is shown in the references requiring a wired connection to the body.

6.5 Discussion

The weDAQ demonstrated performance results comparable to current custom or commercially available electrophysiology recording systems (Table 6.2), with advantages in sampling rate, input range, measurement bandwidth, and wireless transmission bandwidth. The weDAQ does however consume more power primarily because of the WiFi module but still offers all-day wearability with small LiPo batteries and power-saving transmission modes. Specifically, the SPX streaming mode provided a balance of high sampling rate

with minimal streaming data loss and greater energy efficiency compared to normal HDX streaming thanks to duty cycling of the wireless transmission. The dry PCB electrodes presented were reliable over several days, maintaining phase integrity and a 50 Hz impedance of approximately 1 MΩ. The crocodiles outperformed comparable devices (Table 6.3) in electrode count and fabrication scalability. In-ear crocodile electrodes performed well in the electrophysiology testing compared to the dry disk electrodes placed on the forehead and face. The crocodile electrodes connected with the weDAQ captured eye blinks, jaw EMG activity, and alpha power modulation in the brain. For detection of eye movements however, electrophysiological signals captured from in-ear channels were considerably less conclusive than facial and forehead place EOG channels but blinks were still well captured. Although sometimes considered an artifact in EEG measurements, the detection of eye blinks can serve as a reliable marker for sleep staging and validation of the sensing system while streaming [17, 75]. The deployment of multiple streaming weDAQ devices on the BAN was further demonstrated for monitoring multiple subjects during the exercise physiology experiment in which Lead II ECG and biceps EMG activity were well captured.

WiFi was chosen because it supports up to 25x the transmission bandwidth of Bluetooth and is more amenable to forming the BAN. Operating on the 802.11 protocol allows use in nearly all settings and modification of the firmware by the end users. Whereas devices operating on the 802.15 medical body-area network (MBAN) are restricted to usage in only healthcare facilities and must register for approval. We were also able to implement different modes of transmission by leveraging in-house and open-source firmware resources for WiFi to save power and better suit the application-specific needs of in-ear sensing or

on-body health monitoring.

In terms of general usability of the weDAQ, we found the device to be plug-and-play in most cases. Connection to the WiFi network on device start-up and data streaming can be affected by other traffic on the network but simple fixes have been to use a dedicated access point on a channel with less traffic. Using 3D printed enclosures, the weDAQ can be easily mounted to almost any part of the body with either a clip, strap, or adhesive tape (Fig. 6.6(f)). In-ear electrodes were easy to assemble and worked reliably for the duration of the study and were even seen to work after several months of storage. Crocodile devices fit snugly into the ears of subjects tested and remained electrodes remained mechanically stable. In some cases of subjects sweating or moving vigorously, the electrodes were observed slipping out of the ear canal but generally stayed in place.

Finally, we chose to make the weDAQ and PCB electrodes out of COTS components and provide all associated designs open-source to the community as a high-performance tool kit to lower the barrier of entry into niche research areas like in-ear EEG. End users can further enhance the versatility of this sensing platform by tuning the hardware, software, and firmware to fit their specific needs. The weDAQ and accompanying electrodes are well suited to conduct electrophysiological studies involving multiple subjects and/or the need for subjects to move around. For example, studies involving students in classrooms that seek to monitor neural markers for cognitive engagement and social behavior under naturalistic conditions [24, 78], or studies seeking to monitor brain dynamics and motion artifacts during walking [62] or while using multi-modal sensors to track drivers and passengers in a car [12], would benefit from BANs with wearable recording units.

Table 6.3: Comparison with State-of-the-Art Ear EEG Systems

	[68]	[41]	[47]	[32]	[38]	[35]*	[40]	This work
Electrode Count	17	6	4	-	-	10	6	16†
Electrode Material	Ag/AgCl	Ag	-	Ag-Fabric	Ag paint	Ag/AgCl	IrO_2	Ag/AgCl
Electrode Contact	Dry	Dry	Dry	Wet	-	Dry	Dry	Dry
Reference	In-Ear	In-Ear	In-Ear	Behind Ear	External	External	In-Ear	In-Ear
Electrode Area	3.15 mm^2	60 mm^2	-	40 mm^2	-	-	9.6 mm^2	4.40 mm^2
Impedance 50Hz	20.42 $k\Omega\,cm^2$	226.44 $k\Omega\,cm^2$	-	-	-	10 kΩ‡	1.1 $k\Omega\,cm^2$	52.78 $k\Omega\,cm^2$
Earpiece Style	Custom	Generic	Custom	Generic	Custom	Generic	Custom	Generic
Scalable	No	Yes	No	No	No	Yes	No	Yes
Sound Occluding	Yes	No	Yes	Yes	Yes	No	No	No

* This device is worn around the ear, not in-ear. † Earpiece provides silver-plated pads for up to 16 electrodes. ‡ Impedance is listed in reference without area of electrodes.

6.6 Conclusion

We presented a low-profile user-generic and portable ExG instrumentation device with versatile capabilities for in-ear and on-body biosensing. The electrodes were easy to make and reliable for measurements of in-ear and forehead EEG, EOG, and EMG. The weDAQ system captured biosignals from multiple subjects at a high sampling rate and data quality comparable to clinical systems, including in-ear EEG signals during an alpha modulation task, eye blinks, and eye movements. Facial electrodes further captured eye movements and muscle activity from the jaw. Electrode sensors and weDAQ devices were also demonstrated for multi-subject recording during physical activity. The weDAQ creates a body area network to reliably capture and stream electrophysiological data. The custom scalable firmware and high degree of input configurability have enabled this platform

to perform well in each of these applications. The next steps for weDAQ development include improving energy efficiency, demonstrating the input MUX for dynamic rerouting of reference and DRL, and utilizing out-of-band frequencies for continuous electrode-skin impedance monitoring. For the in-ear electrodes, improvements can be made to include integrated reference and DRL electrodes and to implement a standard connector interface. This work paves the way for high-channel count, fast sampling body area networks for mobile health sensing and intelligent closed-loop brain computer interfaces.

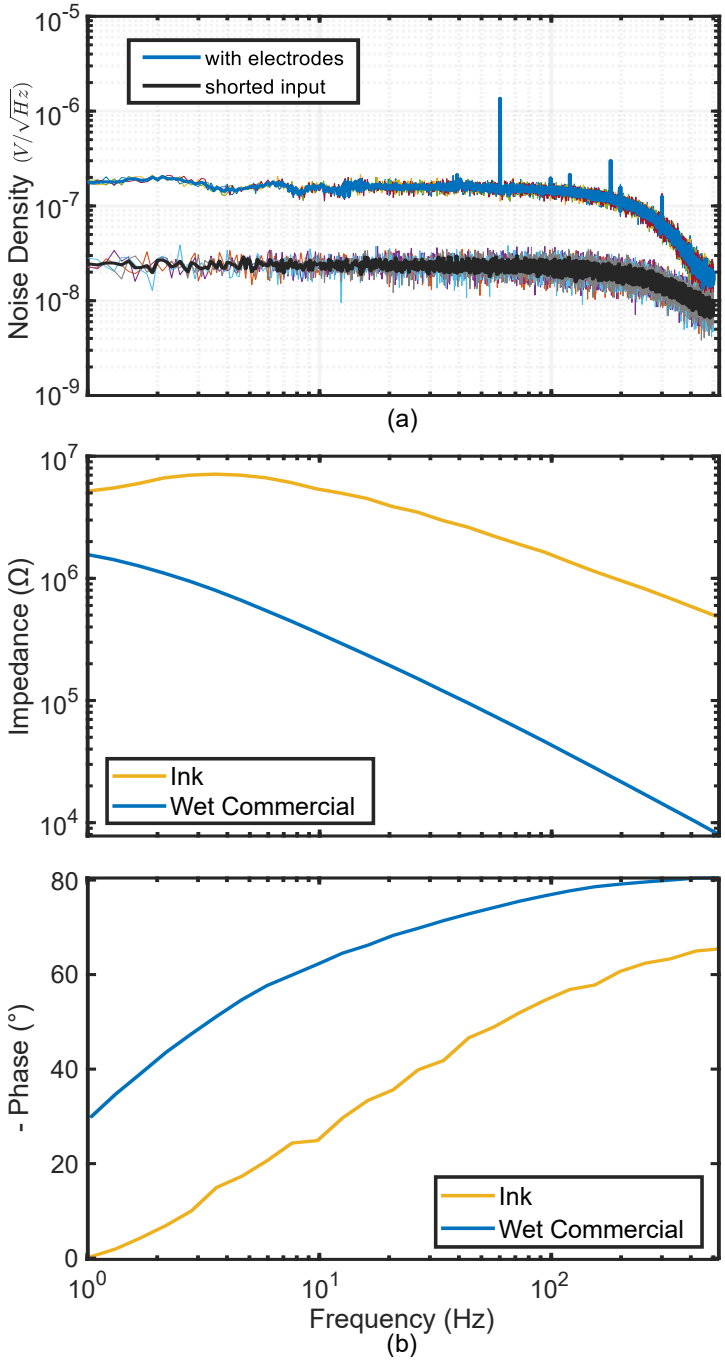

Figure 6.8: (a) Input-referred noise (IRN) spectra for the weDAQ measured with maximum device gain of 24 and 1 kHz sampling rate. (b) Impedance and phase profiles for Ag/AgCl ink applied to the PCB electrodes and commercial, gel Ag/AgCl electrodes.

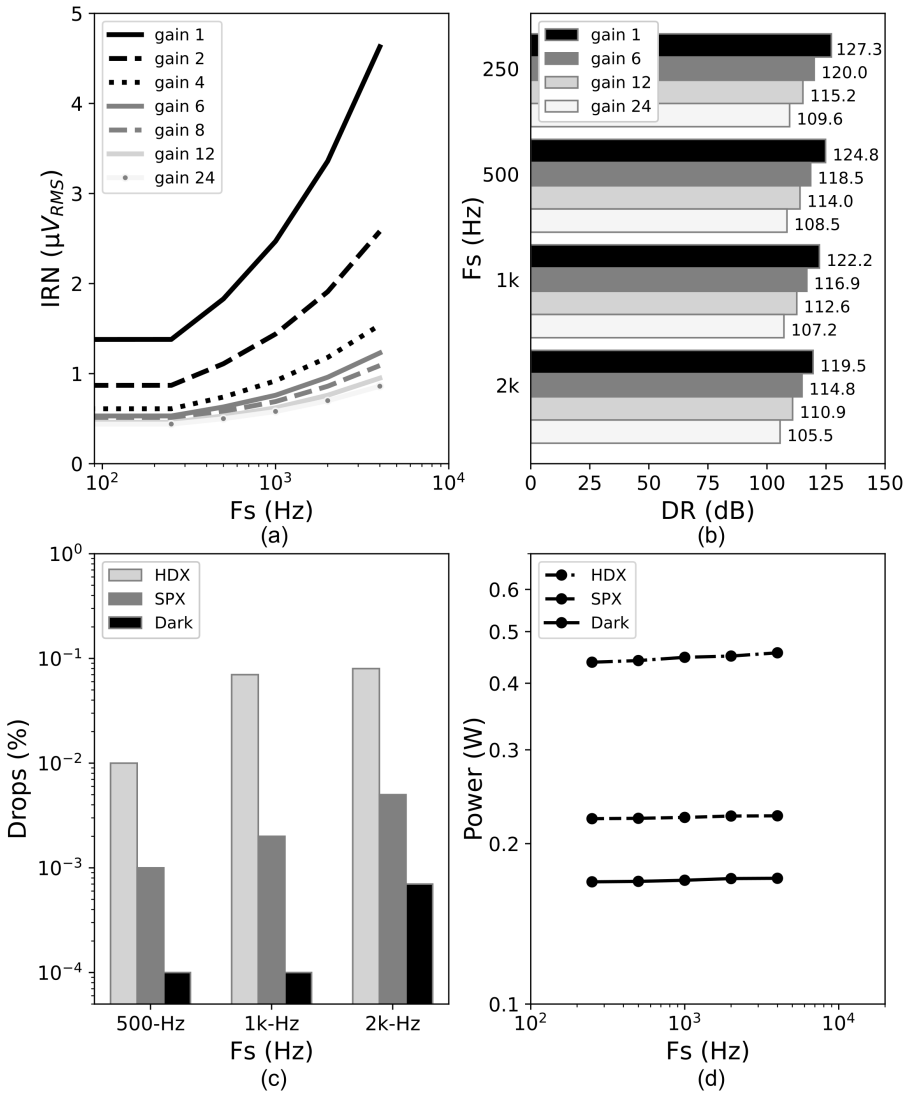

Figure 6.9: (a) Input-referred noise calculated from 0.01 Hz - 70 Hz across sampling frequencies (Fs) up to 4 kHz tested. (b) Dynamic range (DR) across gain settings. (c) Data drops, or corruption, observed for the main modes of operation. (d) Power consumption of the weDAQ.

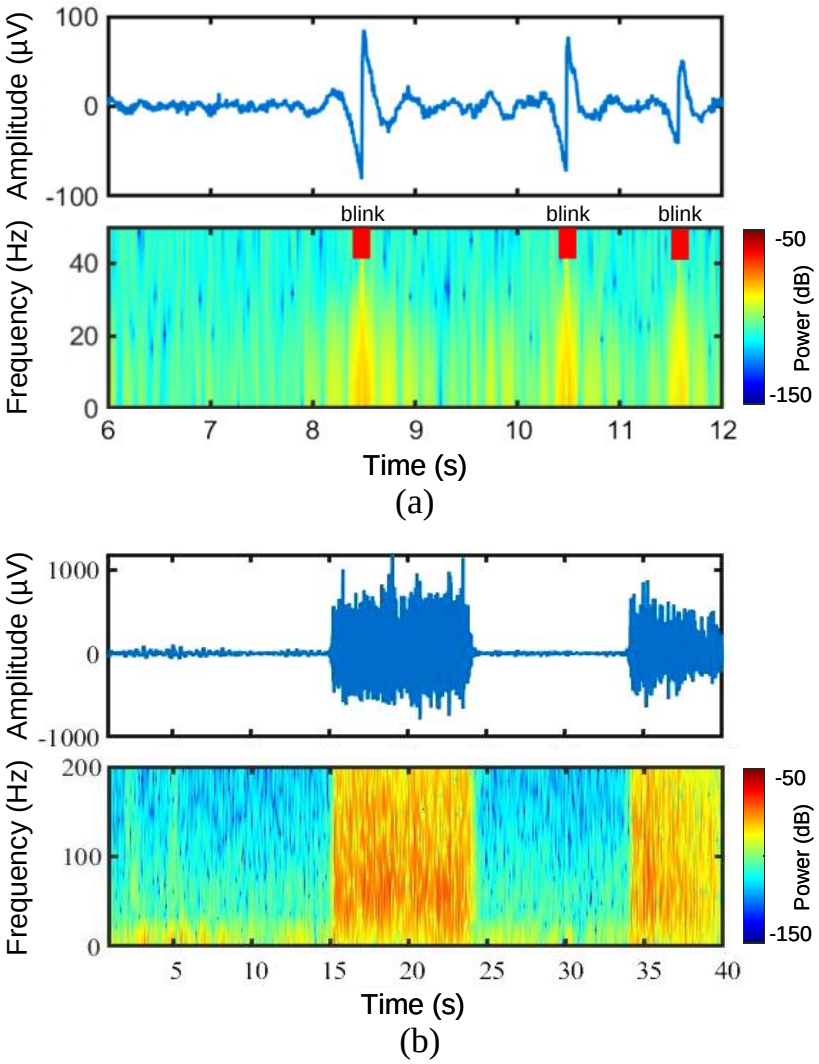

Figure 6.10: The spectrogram and time-series plot (a) of eye blinks and (b) EMG activity of the masseter muscle during jaw clenches, all recorded from in-ear channels.

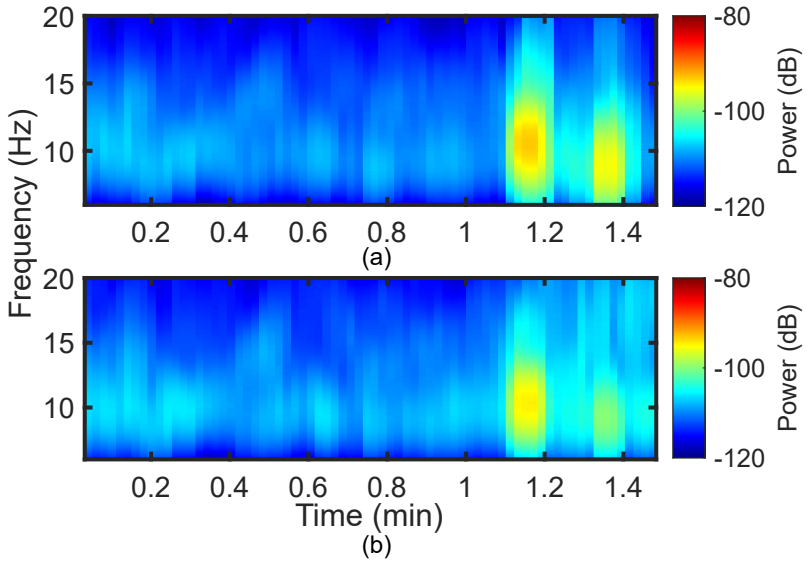

Figure 6.11: Spectrograms of EEG data captured during an eyes-closed alpha-power modulation task from (a) in-ear electrodes and (b) forehead electrodes. A rise in alpha-band power at around 10 Hz is observed for both the in-ear and forehead electrodes at approximately t = 1 min.

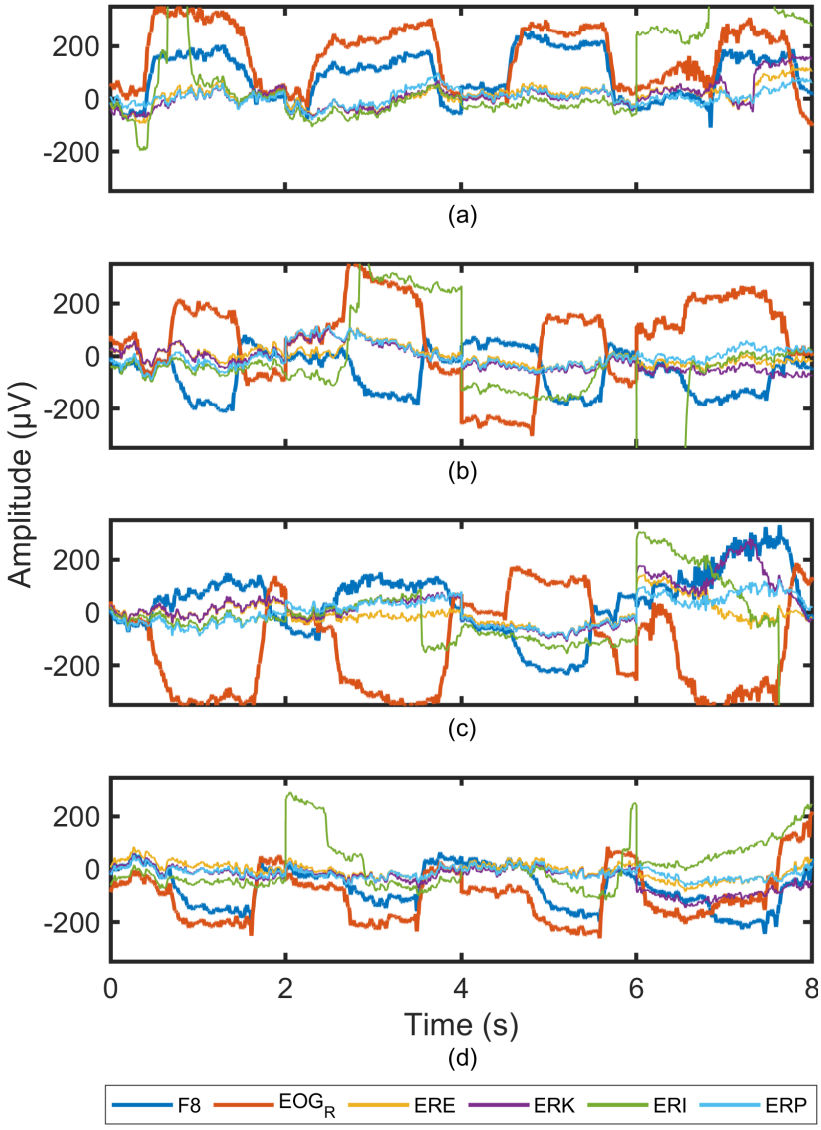

Figure 6.12: EOG activity captured during directional eye movements from center (a) leftward, (b) rightward, (c) upward, and (d) downward. Continuous EOG recording were made from 4 in-ear channels (sky blue, gold, purple, and green), 1 forehead EOG (blue), and 1 facial EOG (orange).

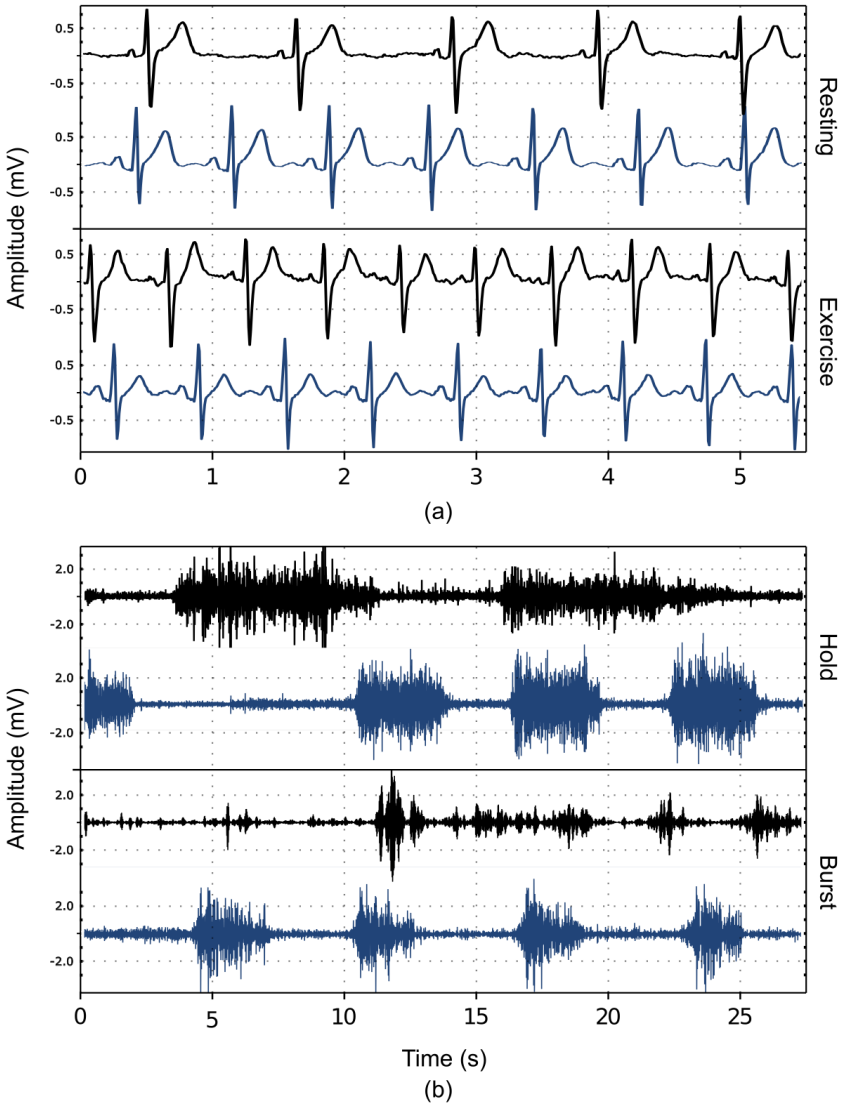

Figure 6.13: (a) ECG recordings were made of subject 1 (black) and subject 2 (blue) while seated and resting for baseline and following a brief period of high-intensity exercise. (b) Subjects were instructed to lift and hold heavy objects before placing them back down.

Chapter 7

Window-Optimized Digital Correlated Double Sampling for Analog Front-End Noise Suppression

7.1 Introduction

Amplifiers play a crucial role in biomedical sensing of elucidating biopotentials originating from the brain and body which often exhibit with small amplitudes and specific frequency ranges. Certain neural signals such as those detectable in the non-invasive electroencephalogram (EEG) have rich low frequency content with amplitudes in the range of 10's of microvolts but, commonly in amplifiers, this range also contains flicker (1/f) noise, in additional to the omnipresent thermal noise, that can further deteriorate signal-to-noise ratio (SNR). Fortunately, a number of noise correction techniques can be

implemented including those based on the principle of correlated double sampling (CDS) which leverages the cyclostationarity of the amplifier noise component over short periods of time to subtract noise from samples. CDS can be effective at reducing low frequency noise but has trade-offs including the addition sampling noise (kT/C), which can depend upon the method of implementation. Here, we explore models for CDS in the analog domain with autozeroed circuits, in the digital domain with delay-subtractor circuits, and consideration of a conventional non-sampling technique of chopper stabilization to compare the effects of each model transfer function on 1/f and thermal noise. This work demonstrates the practical implementation of analog and digital domain CDS on a neural interface system-on-chip (NISoC) and introduces an algorithm for windowed reference weighting to optimize digital CDS performance. Analog CDS was shown to reduce 1/f noise but at the expense of additional thermal noise, as expected, while digital CDS had superior 1/f noise reduction without measurable change to the thermal noise floor of the system. An in-ear electrophysiology study conducted with subjects was shown to benefit significantly from digital CDS, revealing features of the neural signals otherwise obscured by noise in both EEG and electrooculogram (EOG) measurements.

In order for biomedical sensing systems to detect biopotentials from the body, they must maintain a high sensitivity to the signal of interest in a noisy environment. The requirement for high signal-to-noise-ratio (SNR) in such applications guides circuit designers to limit the effects of common noise contributors in amplifiers (Fig. 7.1 such as, thermal, flicker, and sampling noise [43]. However, despite most conventional circuit design mitigation techniques, noise can persist or even worsen due to irregular or dynamic

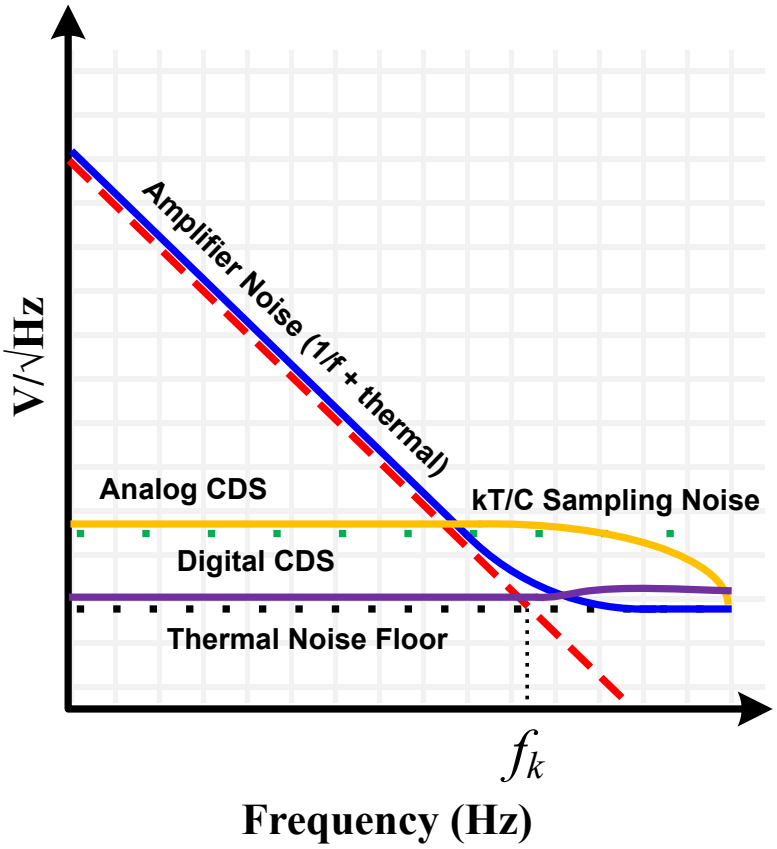

Figure 7.1: Spectral density plot of common noise components for amplifiers and electrodes in electrophysiology measurements.

conditions at the electrode-tissue interface [1, 69].

Thermal noise, also know as Johnson-Nyquist noise, is attributed to the random motion of electrons in electronic systems proportional to temperature and resistance. In amplifiers and analog-to-digital converters, thermal noise, along with sampling noise (kT/C) can be the dominant noise contributor at middle and higher frequencies. Flicker noise ($1/f$ noise) although not fundamental to device operation is common in many electronic systems, exhibiting spectral density that increases with decreasing frequency

according to a $1/f^n$ shape with cutoff f_k. Flicker noise is responsible for diminishing the SNR of biopotentials at lower frequencies. The electrode-skin contact can aggravate noise contributions caused by fluctuations in the high-impedance interface when movement creates mechanical disturbances, build up of triboelectric charge, and injection environmental noise.

7.1.1 Correlated Double Sampling

Correlated double sampling is a method of noise reduction which has been used widely in charge-coupled devices (CCD) imagers but can be applied generally to analog front-ends for the reduction of 1/f noise and thermal noise [98, 106]. In analog CDS, a capacitor in the amplifier feedback loop will be allowed to reset then store the noise seen at the front end with the input electrode disconnected. The input electrode is then reconnected and sampled, allowing for the noise stored onto the capacitor from the first sample to be canceled from the electrode sample. Analog CDS can suffer however, from current injection noise if not allocated sufficient time between samples to settle and, if the reference and sample signals are uncorrelated, an increase in white noise power may be observed [98, 106]. Alternatively, Digital CDS performs the correction post-acquisition and only requires the switching of the input from electrode to internal reference, making it amenable to more architectures [101]. Furthermore, as will be highlighted in this work, the correction algorithm applied to digital CDS can be tailored and optimized for noise removal specific to the amplifier and application.

Analog CDS

Analog Correlated double sampling involves the reset of a capacitor at either the input or in the feedback loop of the amplifier in order to integrate noise present in the amplifier with the input shorted to an internal reference, followed by a reconnection of the input to the external electrode for analog subtraction of noise from the measured signal. The period of the reset and the time between reset and electrode sample will effect the noise correction bandwidth and resulting noise floor.

Digital CDS

Digital CDS involves the alternating sampling for an internal reference voltage and the external electrode signal without an analog reset of the amplifier. The two samples streams are then used post digitization to generate a correct sample set by subtracting the reference samples from the real samples. The reference samples can be subtracted 1:1 or several reference samples surrounding a real sample can be windowed to create an average noise representation.

7.1.2 Biopotentials

Biopotentials are signals generated from electrically active tissues in the body such as the cardiac muscles of the heart and the spiking neurons of the brain. The location on the body where these signals are measured and the methods utilized not only determines which category of biopotentials can be detected but also the magnitude and resolution,

both spatial and spectral, of the signal. The type of target biopotential, the location, material, and invasiveness of the electrodes determine the requirements of the acquisition hardware and place these methods into broadly accepted categories of electrophysiology.

By placing electrodes on the scalp, electroencephalography (EEG) can measure brain signal in the bandwidth from the low hertz to hundreds of hertz, with an amplitude ranging from 10's of microvolts to 100's of microvolts. Although the anatomical coverage of EEG is large, ranging from 10's of square centimeters to the whole brain, the spatial resolution is limited due to with conventional scalp electrode setups. Utilizing small electrodes in high-density arrays can allow for improved spatial resolution or application in tight, non-uniform geometries such as inside the ear canal, but at the cost of higher noise from the electrode skin interface, especially if the electrodes are dry contact [71]. ECoG arrays which are placed closer to or on the surface of the brain will have finer spatial resolution and be able to detect high frequency brain waves with a bandwidth generally of 10Hz to a few kHz.

However, ECoG arrays like EEG, sometimes miss out on important low frequency information from the brain. Slower brain waves such as those found in the delta band have important physiological implications associated with restorative slow-wave sleep (SWS) processes in the brain and body which can have sub-Hz components. Microelectrode array (MEA) based electrophysiology will generally have the finest spatial resolution and the widest spectral bandwidth of 10's of Hz to 10's kHz but overlook important low-frequency signals like K-complexes which are associated with sleep spindles during stage 2 NREM sleep. Acquisition systems would benefit health and wellness research if measurements

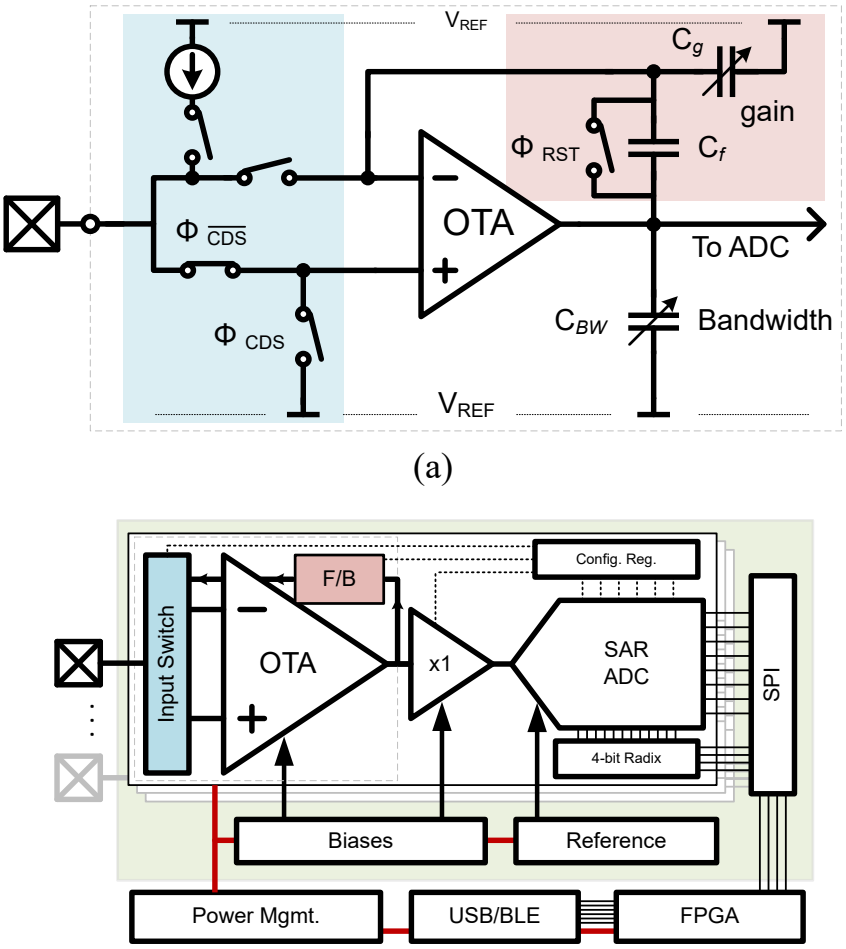

Figure 7.2: (a) The analog front-end of the NISoC [101, 102] has configuration switches controlled by digital timing signals which enable the system to be set in voltage or current clamping modes, and to enable disconnection from the input electrode and connection to an internal reference.

could include this low frequency region.

Here we utilized the Neural Interface System-on-Chip (NISoC) to demonstrate the application of digital CDS to a biomedical amplifier during an electrophysiology recording

[101, 102]. We implemented an algorithm for the post-correction that applied normal window function weights to reference samples neighboring real samples of interest. For the application, we chose in-ear electrophysiology which we have previously demonstrated as being a robust modality for the sensing of EEG, Electrooculogram (EOG), and other electrophysiological signals in a wearable and unobtrusive platform [68–71]. The field of in-ear sensing is gaining interest with the prevalence of personal hearable devices but in-ear still remains a challenging area of the body to sense from given its non-uniform geometry and high electrode-skin impedance due to cerumen, making it an ideal candidate to benefit from enhanced noise mitigation techniques.

Here we expand the conceptual and mathematical models for correlated double sampling and provide a noise analysis on the practical implementation of the CDS techniques on a custom IC neural interface, originally introduced in [cite NISoC].

The article is organized as follows: Section II further describes the circuit models for the CDS techniques. Section III provides the overview for the NISoC IC and specifications for the practical implementation of the CDS techniques. Section IV provides the hardware performance results for the CDS techniques applied to benchtop testing with the NISoC. Section V provides the experimental protocol for the in-ear EEG study and provides electrophysiology results and analysis. Section VI summaries the work and lists the next steps for development and application.

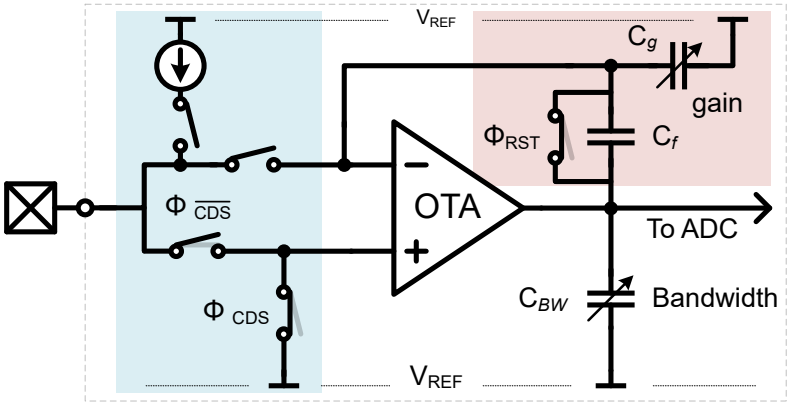

(a)

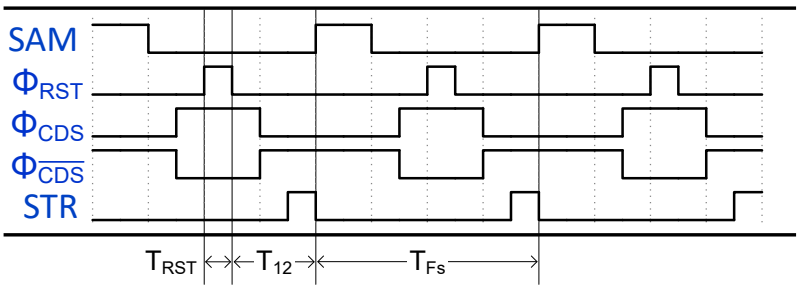

(b)

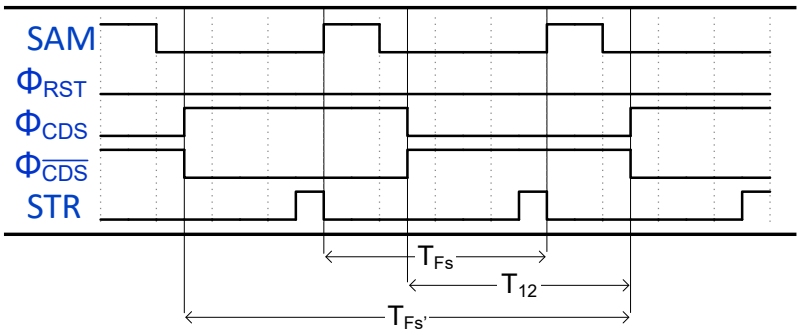

(c)

Figure 7.3: (a) Input configuration of NISoC IC for CDS operation. (b) Analog CDS and (c) Digital CDS timing diagram for switch and sampling control signals.

7.2 Methods

7.2.1 NISoC - Switches and Timing

The NISoC (Fig. 7.2(a)) is a 1mm x 1mm low-power integrated electrophysiology IC designed in 65nm CMOS, with 32 analog front ends and channel-dedicated incremental SAR ADCs. This IC is part of a family of versatile biosensing chips presented previously [43, 101, 102] that was designed with switches at the AFE input configurable for current or voltage clamping modes, and to enable correlated double sampling. The CDS master signal (Fig. 7.3(a)), when high, shunts the non-inverting input to the reference voltage while holding the path to the electrode sensor open. When low, the CDS signal allows for the normal sampling of the electrode sensor path on the non-inverting node at the desired current clamp level. The CDS signal can alternate for every sample-and-hold (SAM) pulse, during which time the actual sensor or reference measurement is made to the ADC, or the CDS signal can be held low for an increased real sampling rate and brought high intermittently for reference sampling. The OTA can be reset by supplying a positive pulse (RST) to the feedback switch to coincide with the CDS signal preceding SAM pulses in order to enable *analog* correlated double sampling, or the reset can be kept low (RST*) after only an initial pulse to enable *digital* correlated double sampling. We focused primarily on the digital double sample operation, during which a reference sample is taken in the sampling period following a real sample with matching gain level and strobed (STR) out through the ADC. Reference samples can be taken as often as every other sampling period, or scheduled intermittently, depending on the type, frequency, and source of the noise being

corrected for. Here, reference samples were taken during every other sampling period and the gain was maintained at the same level for both reference and real samples.

7.2.2 Analog Correlated Double Sampling

Analog subtraction of the noise in the NISoC AFE is achieved in 2 phases (Fig. 7.3(a-b)). First, with the shorting of the input according to ϕ_{cl} to the internal common-mode reference node V_{REF} and then resetting of the AFE feedback according to ϕ_{RST}. Phase 1 allows for storing of the AFE noise while the the input is shorted onto a reset feedback capacitor. Then in phase 2, the input is reconnected to the electrode and the stored phase 1 value is subtracted from the instantaneous noise and offset of the phase 2 measurement in the analog domain. The resulting ACDS corrected sample is then buffered and passed into the SAR ADC per the SAM timing control signal. This mode of operation does not affect the sampling rate of the system nor does it consume any additional measurable power.

7.2.3 Digital Correlated Double Sampling

Real and reference samples stream out from the ADC and into the FPGA with a flag applied to the reference samples, used to separate them from real samples in software (Fig. 7.4). We explored different weighting schemes on the reference samples subtracted from the real samples with the simplest being a single sequential reference sample subtracted from the real sample (Fig. 7.8). The broader schemes relied on the application of weights from window functions to reference samples neighboring the real sample of interest and subtracting a weighted sum of references from the real samples (Algorithm 1). A sweep was

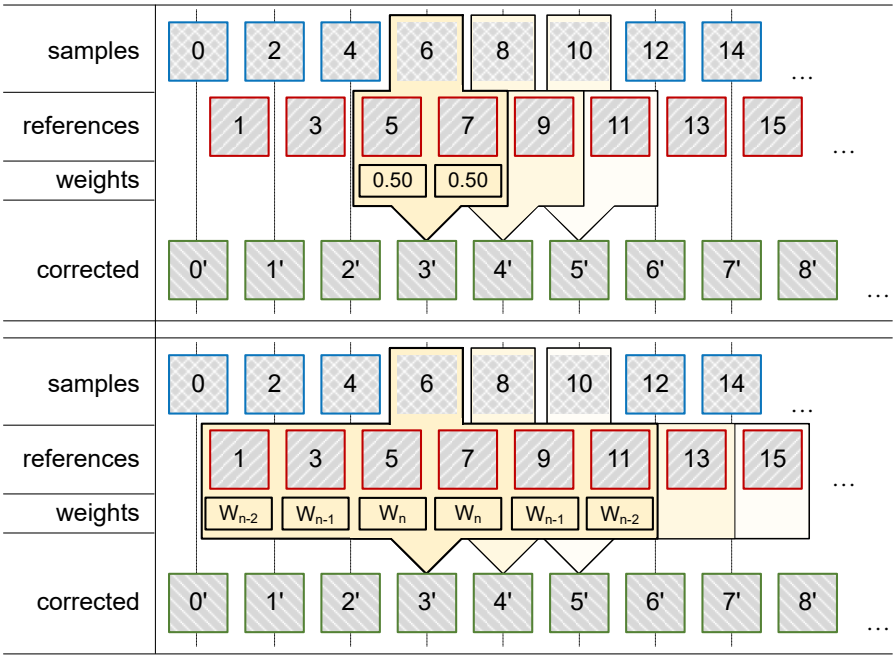

Figure 7.4: Digital CDS split stream relies on external electrode samples with interlaced internal reference samples, which are weighted either with a simple 50-50 ratio or with a more elaborate window function before subtraction to produce the corrected sample stream.

performed on normalized windows (incl. Hanning, Blackman, Kaiser, Dolph-C, Poisson, and Welch) widths to identify optimal noise correction.

7.3 Results

Fig. 7.5 shows the overall effect of the analog and digital CDS operations on the noise of the amplifier. The amplifier noise has clear $1/f$ component that dominates at lower frequencies with flicker noise corner larger than the Nyquist limit for the set sampling rate of 25kHz. Analog CDS is effective at removing the $1/f$ component in the range from 0.05 Hz to approximately 3.5 kHz, after which the noise floor exhibits the downward

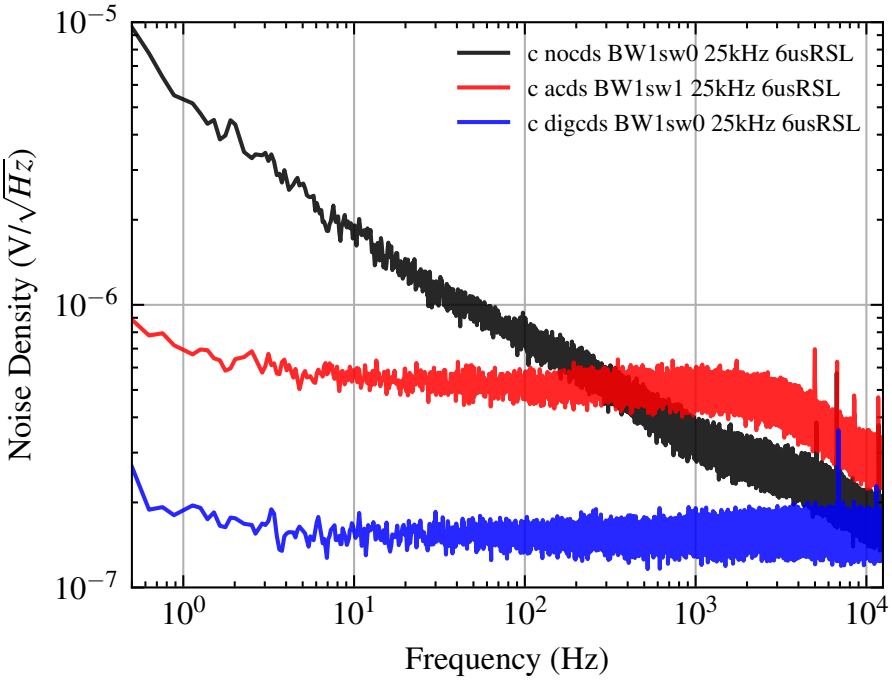

Figure 7.5: Input-referred noise spectral density of NISoC system without CDS correction compared with Analog and Digital CDS modes.

trending flicker shape. There's also significant addition of kT/C noise which raises the noise floor for the analog CDS results far above the white noise floor of the original noise spectra. Specifically, at the crossover frequency of approximately 300 Hz, there's a trade-off in greater white noise for lower $1/f$ noise. In comparison, digital CDS removes a larger amount of the $1/f$ noise component, resulting in a noise floor that is nearly flat from 0.05 Hz to the Nyquist limit. There is no significant addition of the kT/C noise in this mode for the in-band frequencies but the noise floor does trend slightly upward at the flicker crossover frequency without the use of a reference windowing function.

The performance of digital CDS is seen to improve with larger bandwidths at higher sampling rates (Fig. 7.6), as the crossover frequency, which is seen to indicate the low

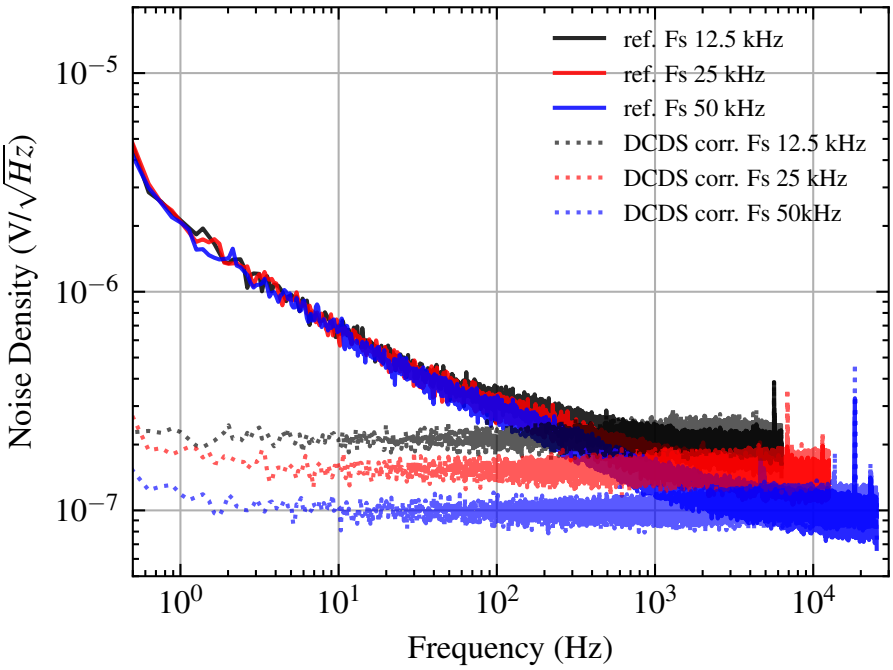

Figure 7.6: Noise spectral density of input-referred digital CDS measurements with 3 NISoC sampling rates: 12.5 kHz, 25 kHz, and 50 kHz.

frequency noise floor level, drops further down the flicker component of the noise spectra. The enhanced performance of digital CDS at higher sampling rates can be attributed to the greater spectral correlation between the reference and sample streams (Fig. 7.7), given that the period τ of the CDS operation naturally decreases with sampling rate. Compared to a sampling rate of 12.5kHz, the fastest rate of 50 kHz has higher low frequency SCC and and higher frequency roll-off. An important consideration for digital CDS is the loss of signal power due to switching of the input, especially at higher sampling rates.

Across input signal frequencies, there is not a significant change in power for a given sampling rate. However, signal percent power was observed to decrease by approximately 0.5% when sampling rate was doubled from 25kHz to 50kHz.

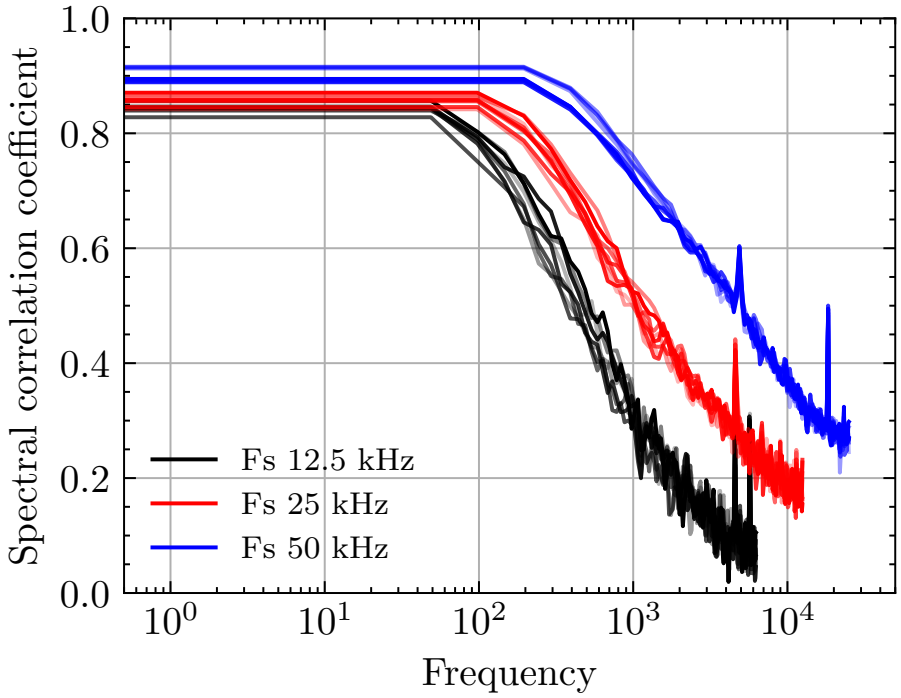

Figure 7.7: Spectral correlation of sample and reference streams in digital CDS for NISoC sampling rates: 12.5 kHz (black), 25 kHz (red), and 50 kHz (blue).

Sequential correction with unity weighted reference samples was effective at reducing noise in the ADC output across a 12.5kHz BW by 53.6%. Correction with equally weighted neighboring reference samples was marginally better with an approximately 55% noise improvement but only for rectangular windows of width 2; any larger caused correction to suffer. The best performing window was the Kaiser-22 at window width of 20, resulting in a 71.1% reduction in noise (Fig. 7.10). The other windows tested scored between 62-69% with peak noise correction occurring at varying window widths but in general, following a trend of rapid improvement and then slow deterioration with increasing window width. The effects of CDS correction on the noise spectra of the ADC's input-referred output can

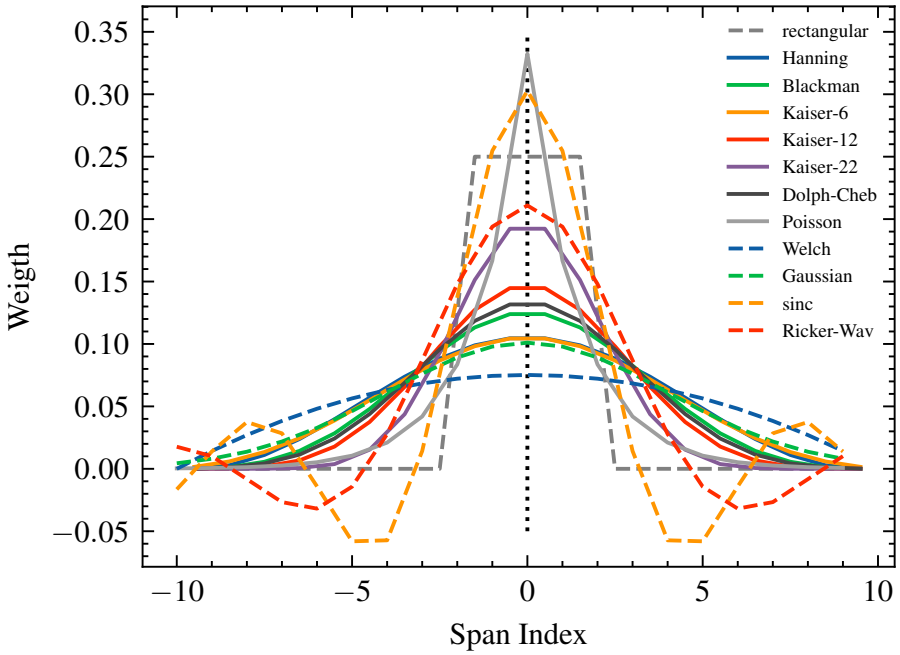

Figure 7.8: Normalized weights across the span of the different windows functions tested. Given a window type and window width, the normalized weights are then applied to the reference samples neighboring the real sample of interest with the middle of the window centering on the nearest 2.

be seen in Fig. 7.5. Specifically, the CDS corrected spectra has substantially reduced 1/f power seen as a flattening of the noise floor from 0 to 1kHz.

7.4 Window-Weighted Digital CDS

$$N_{CDS} = aN_w = 2a\sigma_w^2 \tag{7.1}$$

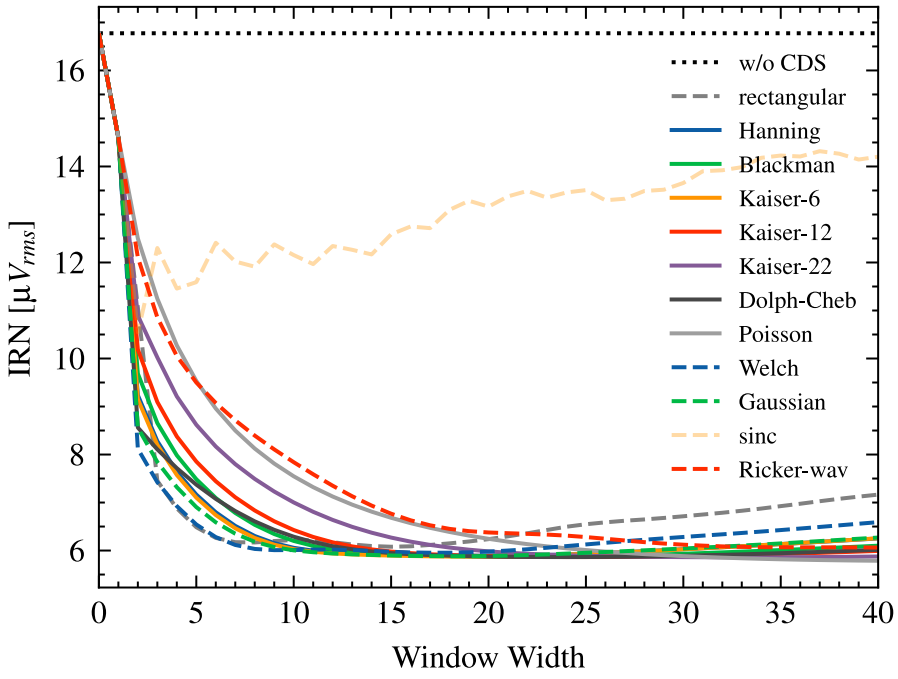

Figure 7.9: Input-refereed noise calculations across a 12.5kHz BW for each window swept across window widths. The best performing window function will reach lowest noise with the smallest width.

$$2a = \frac{N_{CDS}}{\sigma_w^2} \tag{7.2}$$

.

$$(r * h)(t) = \int_0^t r(\tau)h(t-\tau)\,d\tau \tag{7.3}$$

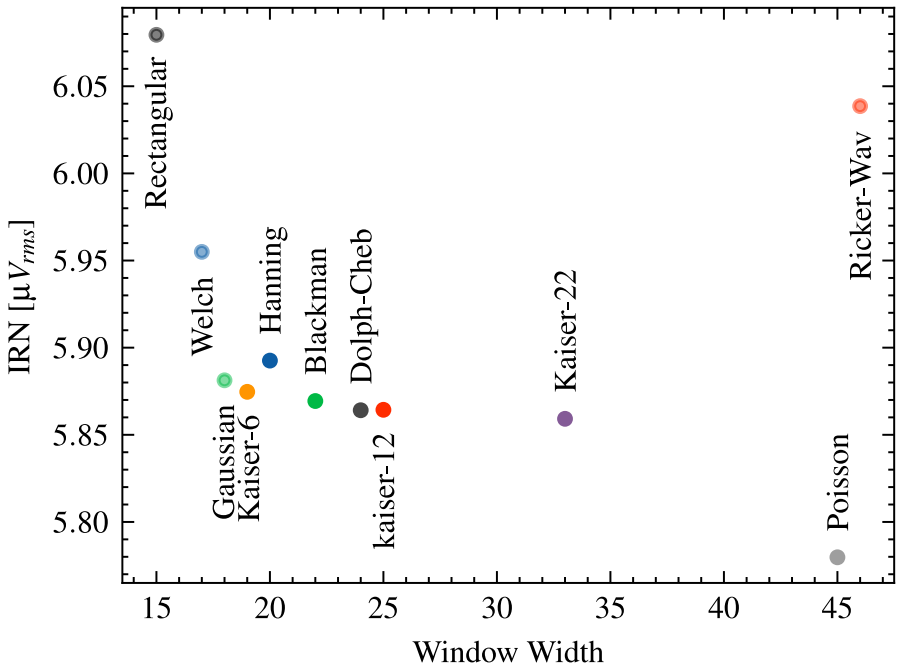

Figure 7.10: Minimum achieved IRN for each window function tested at the corresponding window width of best performance.

Table 7.1: Windowed-Reference Digital CDS Performance Summary

Window	Width	IRN	% Improvement	$2a$
1 Neighbor	1	14.560	24.25	1.515
50-50	2	11.064	56.50	0.870
rectangular	15	6.080	86.87	0.263
hanning	20	5.893	87.66	0.247
blackman	22	5.869	87.76	0.245
kaiser-6	19	5.875	87.73	0.245
kaiser-12	25	5.864	87.78	0.244
kaiser-22	33	5.860	87.80	0.244
dolph-c	24	5.864	87.78	0.244
Poisson	45	5.780	88.13	0.237
welch	17	5.955	87.40	0.252
gaussian	18	5.881	87.71	0.246
sinc	46	6.039	87.04	0.259

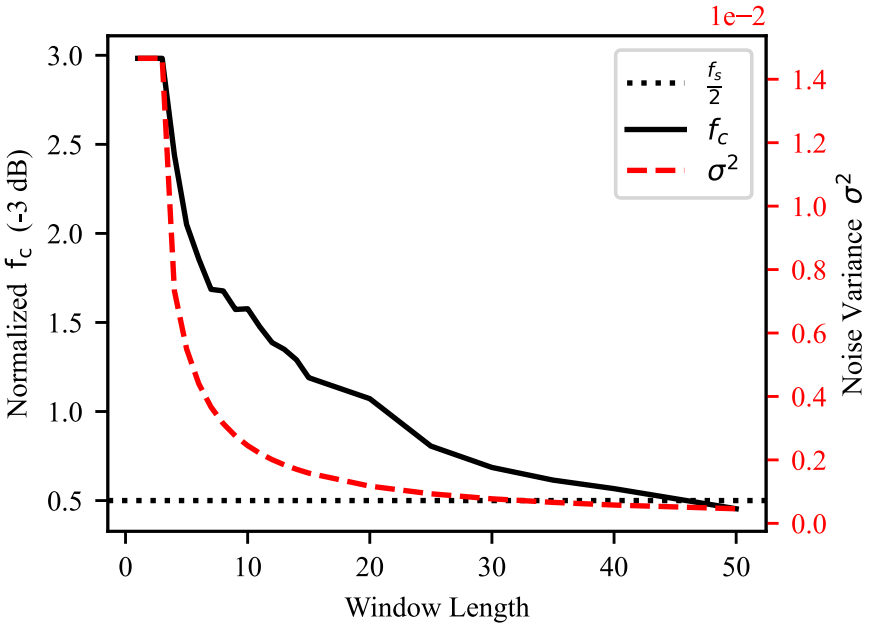

Figure 7.11: Corner frequency and variance of noise of digital CDS signal across Hann widow widths applied to reference samples prior to subtraction.

7.4.1 Window Transfer Function

The Fourier transform of a Hann window $w_\tau(t)$ with length L and for $\tau = 0$ is given by

$$W_0(f) = \frac{sin(\pi L f)}{2\pi L f(1 - L^2 f^2)} \tag{7.4}$$

when applied to S_{CDS} acts a low-pass filter on the reference samples, moving the f_{DS} cutoff frequency to the left.

$$H_{wCDS} = H_{DS} H_{LP} \tag{7.5}$$

$$H_{LP}(n) = \frac{1}{\left(1 + j\frac{\omega}{\omega_c}\right)} \tag{7.6}$$

where $\omega_c = \frac{2\pi}{nT_{12}}$.

$$\bar{u}^2_{CDS} = \frac{1}{2\pi}\int_{-\infty}^{\infty} S_N(\omega)|H_{wCDS}(\omega)|^2\, d\omega \tag{7.7}$$

7.5 Circuit Models

Auto-zeroing AZ

Auto-zeroing is a circuit technique which generally uses a reset switch to neutralize offset at the input of an amplifier prior to or in between measurements.

Delay-Subtraction

Delay-subtraction involves the sampling of noise at the amplifier input and storing the measurement for subtraction of noise and offset from subsequent samples. The time between the noise sampling and subtraction will effect the bandwidth of noise in the resulting sample. The spectral correlation of the noise in the two samples will diminish has the delay time increases, reducing the bandwidth of correction and increasing the kT/C contributions.

The input-referred noise of an amplifier at low-frequency tends to contain both a

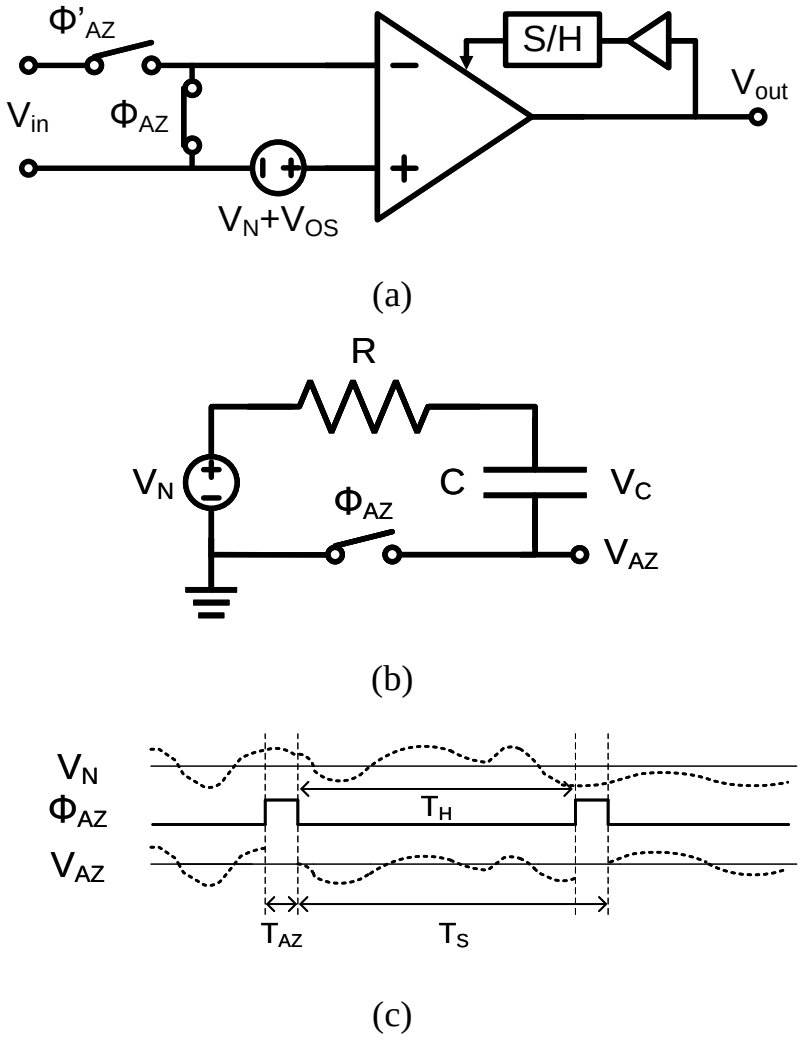

Figure 7.12: (a) Amplifier circuit with basic autozeroing implementation. (b) Simplified autozeroing circuit model with AZ switch and S/H capacitor. (c) Noisy input signal V_N and autozeroed output signal V_{AZ} depicted along with timing diagram for AZ switch control signal.

white and flicker noise component which according to [98] can be written as:

$$S_{\mathrm{N}}(f) = \left(1 + \frac{f_k}{|f|}\right) \; S_0 \tag{7.8}$$

where S_0 is the white noise PSD and f_k is the $1/f$ corner frequency defined as the frequency at which the flicker noise and white noise become equivalent.

7.5.1 Autozeroing

AZ in an analog CDS technique that involves the sampling of noise in order to subtract it from incoming signal containing both the signal of there interest and the undesired noise. The greater the cyclostationarity of the noise component such in the case of DC offset or low-frequency (1/f) random noise, the better AZ will remove the noise. The correlation strength of the noise sampled to the noise present in the subsequent mixture of sample and noise will determine how effectiveness of the AZ correction. In general, AZ acts as a low-pass filter because the lower frequency noise contributions tend to have greater correlation over time than high frequency random noise, and because AZ causes an increase in noise density at higher frequencies as a consequence of the potential aliasing of wideband noise. AZ generally is performed in two steps: (1) internal noise sampling and (2) external signal sample and correction. The first step can involved the disconnection of the amplifier's input from the electrode and the connection of an internal reference clamp voltage such as the common-mode level. This step should also include a reset pulse for the feedback loop of the amplifier. The offset and noise of the amplifier is therefore sampled during step 1 onto a S/H capacitor. In step 2, the input of the amplifier is reconnected

to the external electrode and the external signal which is mixture of the signal of interest and the amplifier noise contributions. As the external signal is sampled onto the same S/H capacitor which contains noise information for the last instance, the resulting measurement is subtracted of the noise and offset.

In Fig. 7.12b., each time the AZ switch closes according to the timing diagram for ϕ_{AZ} (Fig. 7.12c.), the noise signal represented as V_N passes across the resistor R and capacitor C, while V_{AZ} is reset to zero. When the switch opens again follow the short T_{AZ} period, the noise V_N is effectively sampled on C as V_C, while V_{AZ} at the output now reflects the difference between the instantaneous V_N value and V_C:

$$V_{AZ} = V_N - V_C. \tag{7.9}$$

The noise V_N can further be assessed as the PSD $S_N(f)$ of a stationary random noise representation $V_N(t)$ comprised of a baseband component $S_{bb}(f)$, which the autozeroing removes, and a foldover component $S_{fold}(f)$ representing the out-of-band aliased noise.

7.5.2 Auto-zeroing Transfer Function

Assuming the noise into the system $S_N(f)$ is stationary random, the noise power spectra of can be decomposed into two components: the baseband and the foldover,

$$S_{\text{ACDS}}(f) = |H_0(f)|^2 S_N(f) + S_{fold}(f) \tag{7.10}$$

where

$$S_{fold}(f) = \sum_{\left(\substack{n=-\infty \\ n\neq 0}\right)}^{+\infty} |H_n(f)|^2 S_N\left(f - \frac{n}{T_s}\right) \tag{7.11}$$

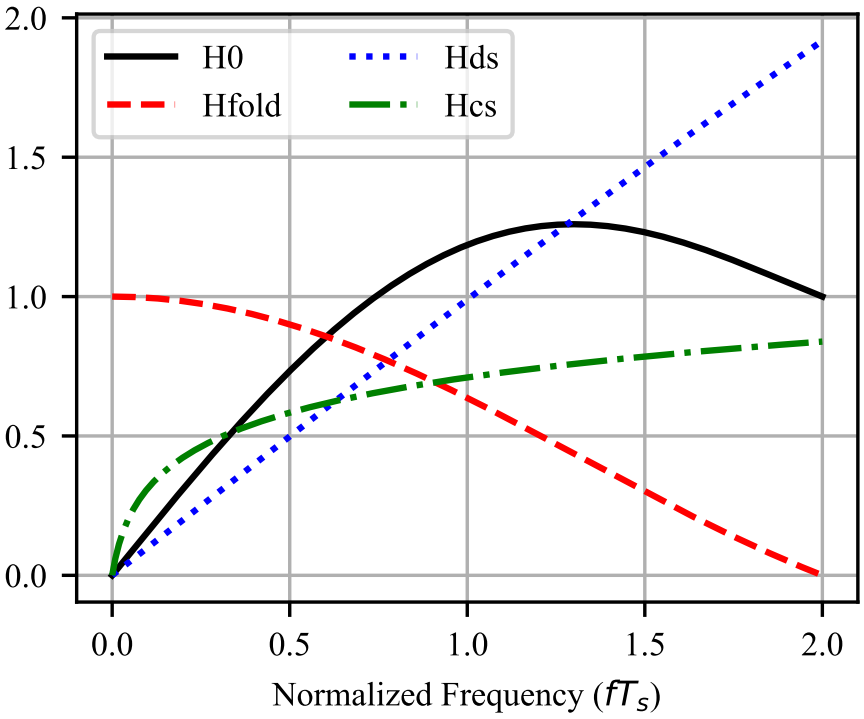

Figure 7.13: Comparison of model transfer functions depicted in bandwidth twice the sampling rate for autozeroed, delay-subtractor, and chopper stabilization.

The baseband transfer function for lower frequencies, $\pi f T_h \ll 1$, $H_0(f)$ acts like a differentiator

$$|H_0(f)| \cong \pi f T_h. \tag{7.12}$$

If the CDS reset time $T_{CDS} \ll T_h$, where T_h is the hold time the noise is allowed to integrate after the analog reset pulse, the foldover transfer functions merge into

$$|H_n(f)|^2 \cong [d \cdot sinc(\pi f T_h)]^2 \tag{7.13}$$

for $n \neq 0$ and $T_{CDS} \ll T_h$.

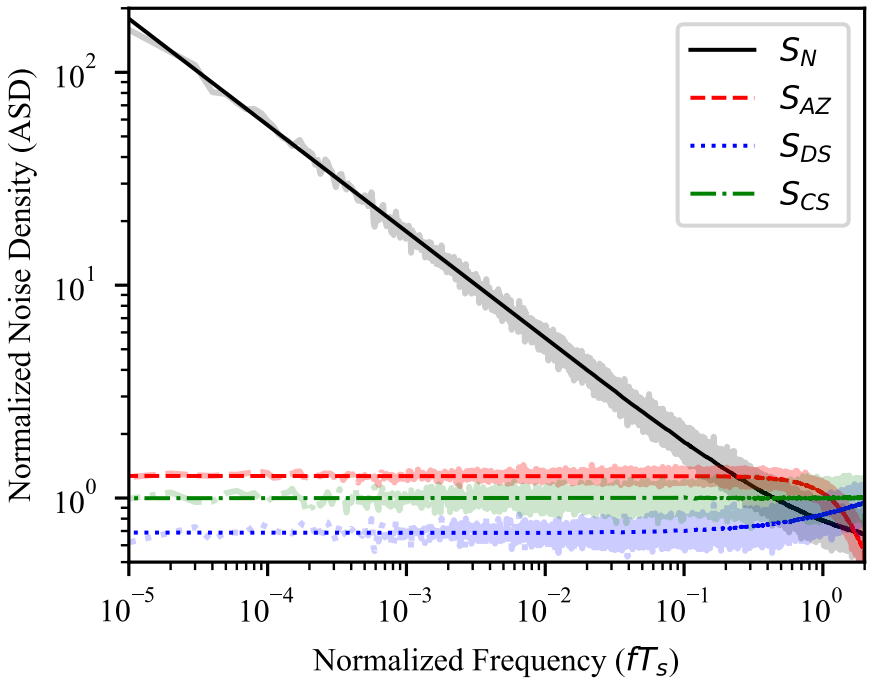

Figure 7.14: Amplitude spectral density of noise correction for CDS models.

The autozeroing transfer functions are plotted in Fig. 7.13 as the baseband H_0 and foldover H_{fold}. Baseband has a the shape of a differentiator up to normalized frequency range of 1, while the foldover function more closely resemble a sinc function. The effect of the squared H_{AZ} transfer functions on the noise at the amplifier's input S_N is shown in Fig. 7.14 as a near complete flattening of the ASD up to the flicker corner frequency f_k. The noise floor however is actually elevated at lower frequency above the white noise normalized ASD level of 10^0.

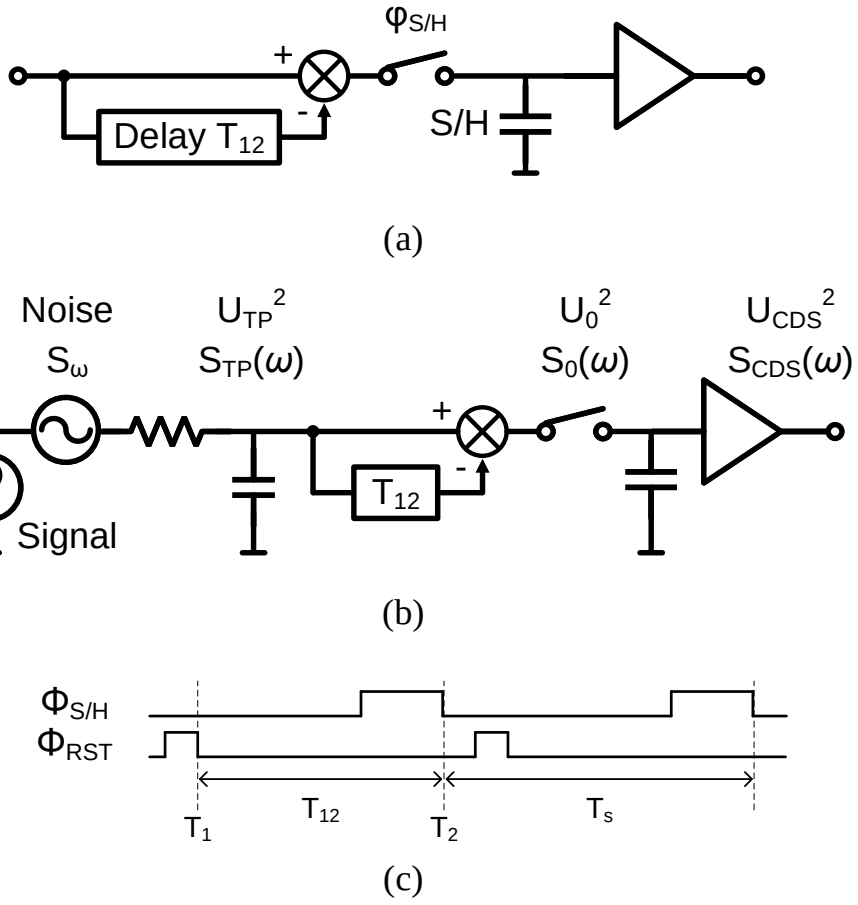

Figure 7.15: (a) Amplifier circuit with basic delay-subtractor implementation at the input. (b) Model of correlated doubling sampling circuit with first-order noise sources. (c) Timing diagram of switch control signals for reset and S/H.

7.5.3 Delay-Subtractor

The delay-subtractor can be described as either an analog or digital CDS technique depending on the domain in which the noise reference sample is held. If noise is sampled onto a S/H capacitor, it will noise subtraction in the analog domain, or if sampled, digitized, and then either fedback through a digital-to-analog converter or subtracted in an FPGA,

the mode will be in the digital domain. The circuit model here on the sampling portion of the delay-subtractor which extends to both domains.

The noise power modeled at the amplifier's input can be described as $\bar{u}_N^2 = 2S_N * B_n = S_N/(2\tau_0)$, where the noise bandwidth of the of the noise source is $B_n = 1/(4\tau_0)$ with low-pass time constant $\tau_0 = RC$.

Then, the autocorrelation functions according to [105], for the noise source

$$R_N(\tau) = \bar{u}_N^2 \; e^{-|\tau|/\tau_0} \tag{7.14}$$

and the delay-subtractor,

$$R_{DS}(\tau) = 2R_N(\tau) - R_N(\tau + T_{12}) - R_N(\tau - T_{12}) \tag{7.15}$$

can be combined to describe the CDS output noise power as:

$$\begin{aligned} \bar{u}_{CDS}^2 &= \bar{u}_{DS}^2 \\ &= R_{DS}(0) = \sigma_{DS}^2 \\ &= 2 \; \bar{u}_N^2 \left(1 - e^{\frac{-T_{12}}{\tau_0}}\right) \end{aligned} \tag{7.16}$$

and the delay-subtractor transfer function as:

$$H_{DS} = j2 \sin(\omega \frac{T_{12}}{2}). \tag{7.17}$$

With the H_{DS} transfer function and noise modeled at the amplifier's input, the total power in the frequency domain can be represented as:

$$\bar{u}_{CDS}^2 = \frac{1}{2\pi} \int_{-\infty}^{\infty} S_N(\omega) |H_{DS}(\omega)|^2 \, d\omega \tag{7.18}$$

$$
\begin{aligned}
S_{i\ CDS}(\omega) &= \frac{1}{T_s^2} \sum_{n=-\infty}^{\infty} S_{DS}(\omega - n\omega_s) \\
&= \frac{1}{T_s} \sum_{n=-\infty}^{\infty} R_{DS}(nT_s)\ e^{j\omega nT_s}
\end{aligned}
\tag{7.19}
$$

7.5.4 Delay-Subtractor Transfer Function

According to [3], the output spectral density after ideal sampling $S_{i\mathrm{CDS}}$ is modified by the S/H time t_A such that

$$
S_{\mathrm{CDS}} = S_{i\mathrm{CDS}}(\omega)\ t_A^2\ sinc^2(\omega t_A/2\pi) \tag{7.20}
$$

where $\alpha = t_A/T_s$ and the function $sinc(x) = \sin \pi x/(\pi x)$.

If the CDS output spectral density S_{CDS} is normalized with the white noise spectral density S_w and the *sinc* function squared, it can be approximated according to

$$
S_n(\omega) = \frac{S_{CDS}}{S_w \alpha^2\ \mathrm{sinc}^2(\omega t_A/2\pi)} \approx \beta^2 \gamma \tag{7.21}
$$

for conditions of oversampling $\beta < 1$, where

$$
\beta = \frac{T_s}{\tau_0} = 4T_s B_n. \tag{7.22}
$$

The ratio of the output noise power $\bar{u}_{CDS}^2$ to S_n, which is proportional due to the white noise shape of S_n, when taken up to the ideal Nyquist limited bandwidth, can be described as a factor of transfer functions:

$$
a = \frac{1}{2\pi} \int_0^{\frac{\omega_s}{2}} sinc^2(\omega t_A/2\pi)\, d\omega \Big/ \int_0^{\infty} sinc^2(\omega t_A/2\pi)\, d\omega. \tag{7.23}
$$

The delay-subtractor transfer function plotted in Fig. 7.13 shows a nearly linear shape from normalized frequency of 0 to 2. The effect of the squared H_{DS} transfer function

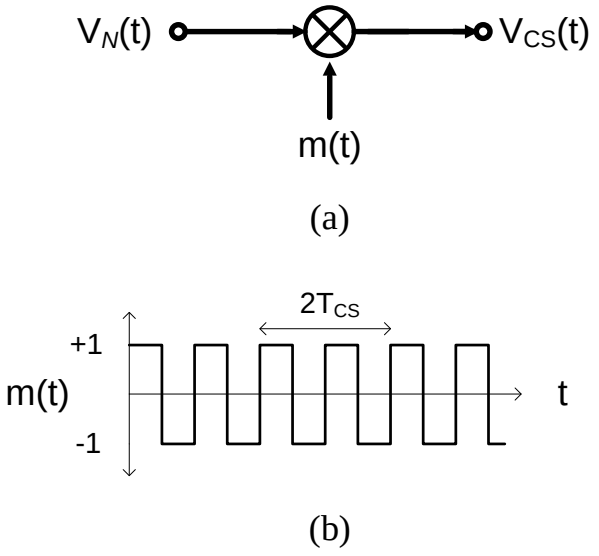

Figure 7.16: (a) Model of signal $V_N(t)$ chopped with modulation signal m(t) producing output $V_{CS}(t)$. (b) Modulation signal m(t) over time.

on the noise at the amplifier's input S_N is shown in Fig. 7.14 as a near complete flattening of the ASD up to the flicker corner frequency f_k. Unlike S_{AZ}, the noise floor is actually lower at lower frequency than the white noise normalized ASD level of 10^0.

7.5.5 Chopper Stabilization

The chopping technique does not rely on sampling but rather modulates the incoming signal to the amplifier to a higher frequency where low-frequency flicker noise is negligible before passing through the amplifier and then being demodulated back to the baseband. The chopping frequency defined as $f_{chop} = 1/T_{chop}$ where the period is the time between rising edges of the square modulation signal. For chopping stabilization to be effective in maintaining gain, the modulators have to match phase shift between input and output to

the phase shift of the amplifier.

According to [98], the total residual noise of a typical amplifier in the baseband can be given as:

$$S_{CDS} \cong S_0(1 + 0.8525 f_k T) \tag{7.24}$$

for $fT \leq 0.5$ and $f_c T \gg 1$. Where the contribution of the chopped flicker noise can be approximated as essentially a white noise component scaled by a value less than 1. An fitted transfer function based on:

$$S_{CS(f)} = \left(\frac{2}{\pi}\right)^2 \sum_{-\infty}^{\infty} \frac{1}{n^2} S_n\left(f - \frac{n}{T}\right) \tag{7.25}$$

can be given by:

$$H_{CS} = \frac{1}{H_{CS_c}} 0.04 \ln 13.4\pi f + 1 \tag{7.26}$$

where $H_{CS} = 2/(3\pi)$.

The chopper stabilization transfer function plotted in Fig. 7.13 shows a nearly logarithmic shape from normalized frequency of 0 to 2. The effect of the squared H_{CS} transfer function on the noise at the amplifier's input S_N is shown in Fig. 7.14 as a near complete flattening of the ASD up to and past flicker corner frequency f_k. Unlike S_{AZ}, the noise floor is actually insignificantly different across the frequency bandwidth below the chopping rate compared to the white noise normalized ASD level of 10^0.

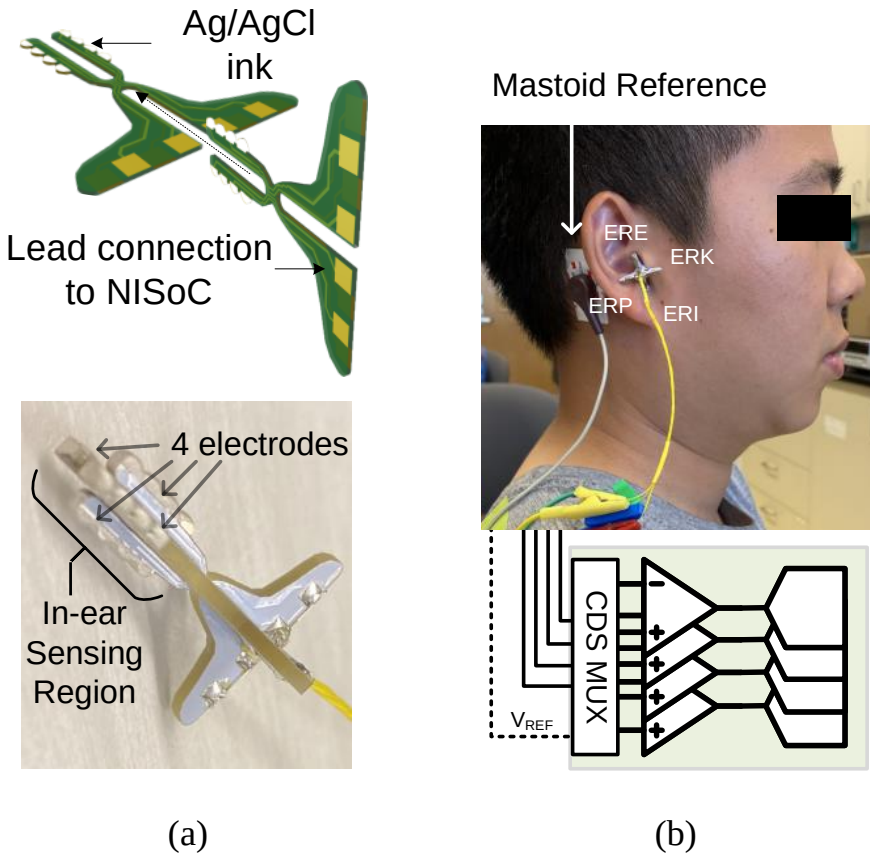

Figure 7.17: In-ear Ag-AgCl electrodes (a) enable EEG and EOG measurements recorded with the NISoC system (b) in an unonbtrusive recording setup.

7.6 Electrophysiological Recording

The in-ear EEG apparatus was comprised of the 2 planar Crocodile v1 electrode PCBs [71], mated together to form the 3D structure shown in Fig. 7.17(a). Each crocodile has 8 semi-circular silver-silver chloride (Ag-AgCl) plated electrodes with a diameter of 2 mm and a 0.4 mm thickness. In total, 16 sensing electrodes were positioned inside the ear canal with external reference and DRL.

The EEG experiment protocol implemented was a standard eyes-open and eyes-closed

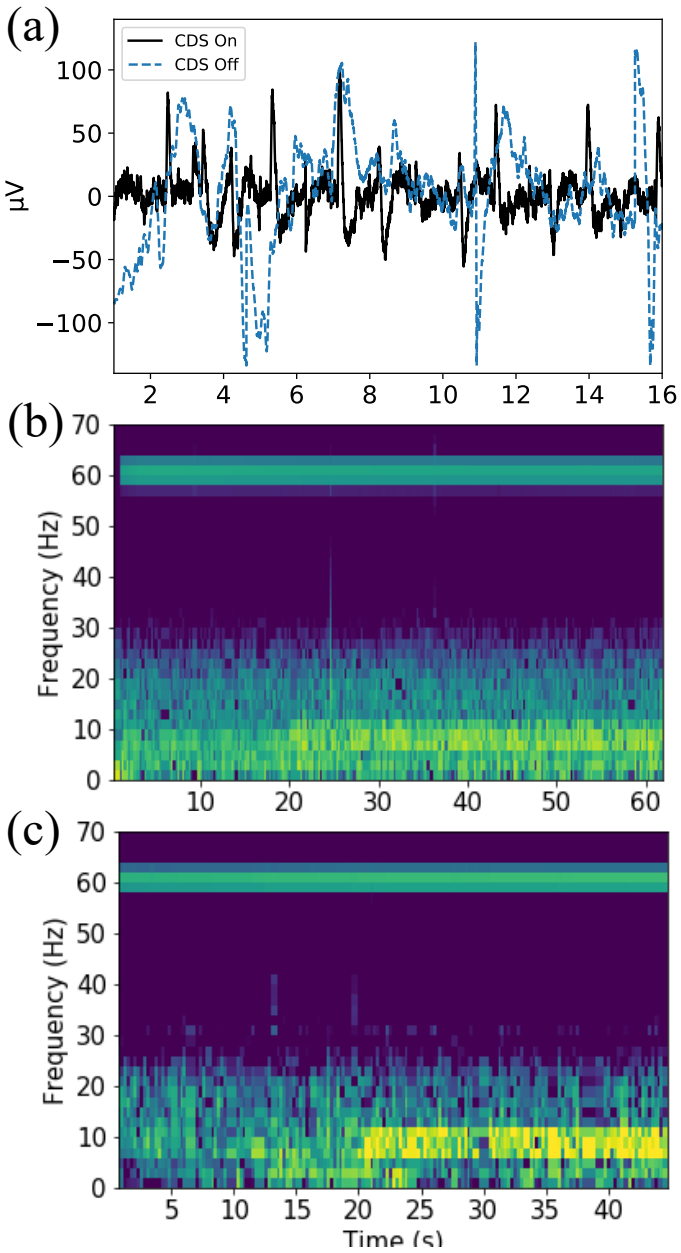

Figure 7.18: (a) EOG time-series data shown for left and right eye movements.(b) Spectrogram of in-ear EEG measurement without CDS and (c) with CDS.

alpha band power modulation [70, 71]. The subject was seated comfortably and asked to keep their eyes open for 30 seconds, followed by a 1 minute period of the subject keeping their eyes closed. For the EOG experiment, the subject was instructed to move their eyes left and right per the beat of a 1Hz metronome. Raw data from both experiments was low-pass filtered at a cutoff frequency of 20Hz using a 5th order Butterworth filter after the application of the CDS correction, where applicable.

The electrophysiology measurements made using the NISoC from In-Ear electrodes benefited from the low-frequency noise reduction of the windowed digital CDS. Specifically, left and right eye movements, seen as positive and negative voltage deflections, respectively, were seen to become substantially clearer in the time series data with digital CDS correction (Fig. 7.18a). In-ear EEG measurements tracking alpha activity in the brain during an eyes-closed protocol also benefited as seen in the comparison of the spectrograms of 2 consecutive measurements made without (Fig. 7.18b) and with (Fig. 7.18c) digital CDS correction. Alpha band power in the brain is seen to increase upon the subject closing their eyes at 20 seconds but it is clear that the SNR is enhanced in the recording with digital CDS correction (Fig. 7.18c).

7.7 Conclusion

We presented here a method for optimizing digital correlated double sampling using window weighting of reference samples to enhance the noise performance of an integrated neural interface System-on-Chip. Digital CDS correction substantially reduces 1/f noise

contributions from the amplifier. Digital CDS has advantages over analog CDS in that it does not require a feedback reset switching circuit, can be performed intermittently potentially saving signal bandwidth, and, as was shown here with the windowed weighting of reference samples, can benefit from optimized post-processing correction.

Algorithm 1: Digital Correlated Double Sampling

$w = abs(w_n)$

if $w = 0$ **then**

    $sub = S_{Ref}$

else if $w = 1$ **then**

    $sub[0] = S_{Ref}[0]$

    $sub[1:] = 0.5 \times S_{Ref}[0:\text{-}1] + 0.5 \times S_{Ref}[1:]$

else

    $span = w \times 2 + 2$

    $win = hanning(span)$

    $wts = win / \sum_{j=0}^{span} win[j]$

    $sub[0:w] = S_{Ref}[0:w]$

    $range = len(S_{Ref}) - (w \times 2 - 1)$

    for $i : 0 \rightarrow range$ **do**

        $sub[1 + w] = \sum_{j=0}^{span} wts[j] \times S_{Ref}[i : w \times +i]$

$C = S_{Elec} - sub$

$C = C - mean(C)$

Chapter 8

Attention State Classification with In-Ear EEG

8.1 Introduction

Electroencephalography entirely inside the ear (in-ear EEG) opens up exciting avenues for unobtrusive continuous physiological and cognitive state monitoring. This work presents techniques towards precise attention state classification based on data recorded from comfortable, binaural in-ear EEG instruments used during a vigilance task experiment. We recorded both on-scalp and in-ear EEG signals from multiple subjects, and we show that in-ear EEG offers comparable classification accuracy. Our work is the first adaptation of Common-mode spatial filtering techniques applied to signals acquired from sparse electrodes on untethered subjects. We demonstrate 90–95% accuracy (scalp-EEG with 30 electrodes) and 70–75% (in-ear EEG with 5 electrodes inside the ear canal and concha) in classifying

attentive and resting states. We also show our approach to be lightweight for low-power on-chip classification with the capacity for few-shot learning. A necessity for wearable, continuous health sensors accommodating resource-constrained applications and adaptation to inter-subject differences and varying environmental conditions. This study suggests the future viability for a System-on-Chip (SoC) integration for user-generic and portable devices capable of closed-loop cognitive state monitoring and neuro-feedback.

8.2 Introduction

Brain-Computer Interfaces (BCI) are an important technology that bridge human brains and different types of functional devices. Clinically, BCIs are in use for people with motor disabilities to extend control of their real, or virtual, environment using just brain waves. The technology has also been applied to training, rehabilitation, and recreation. Electroencephalography (EEG) is a ubiquitous non-invasive, portable neuro-imaging technique foundation to most BCIs, responsible for providing the rich spatiotemporal neural information in mental state classification [11]. The conventional EEG acquisition methods acquire brain waves with attachment of metallic electrodes with ionic conductive pastes to the subject's scalp together with a cap or other wearable equipment. Practical use of conventional scalp EEG in everyday life is severely limited because of the long setup procedures and obtrusive head-worn apparatus.

EEG recorded from inside the ear (in-ear EEG) has emerged as a new type of sensing modality that slims down conventional scalp EEG brain monitoring methods by

reducing electrode count and footprint to a discrete, comfortable device akin to wireless earphones [40,41,68,69,113]. In-ear EEG opens an exciting road map to wearable BCIs and continuous unobtrusive physiological and cognitive state monitoring. From normal everyday tasks like reading and driving, to critical tasks requiring sheer focus and self regulation like surgery, maintain attention on the task for enhanced safety and productivity becomes imperative. The requirement of continuous monitoring of attention during such tasks necessitates low-profile comfortable and portable EEG sensing. As the conventional bulky EEG headsets are unsuitable for wearable settings, in-ear EEG sensors offer a promising and convenient alternative. However, in-ear EEG devices have not been demonstrated yet to be practically suitable for real world applications as they can also have long wires and perform poorly compared to on-scalp headsets.

In particular, sensing in the ear canal produces not only new sensing locations other than the scalp and also proximity to brain sources, especially the auditory cortex, but also utilizes body real estate shared with everyday devices. In-ear EEG sensors have the potential to integrate with widely used earphones, hearing aids, and hearing prostheses. While in-ear EEG sensors have already shown great promises in the clinic and some daily applications, the main challenges of in-ear EEG sensing are weaker measured signals from smaller electrodes with reduced spacing and a lower signal-to-noise ratio compared to scalp EEG measurements. Specifically here, we only consider *in-ear* EEG for which all sensing, referencing, and active grounding (DRL) electrodes are placed only in the ear canal, concha cymba, or concha cavum [69].

There have been several studies on monitoring subject attention states through brain

activity measurement techniques. There are various situations (driving [27], studying [111], exercising [108]) where we are often required to maintain attention to boost efficiency and prevent severe consequences such as traffic accidents and workplace fatalities. However, most works involving mental state classification through in-ear EEG acquisition suffer from low accuracy or require higher epochs (in the order of 30 seconds to several minutes) [60] as compared to scalp-EEG, and the model is substantially prone to inter-subject variability, noise in the operating environments, and performance of the acquisition instruments. As a result, designing a robust in-ear EEG device capable of accurate cognitive-state analysis under various sources of noise and variability is challenging.

The primary motivation for this work is to develop efficient signal processing and Machine Learning (ML) methods for accurately determining attentive and resting brain states from unobtrusively, sparse electrodes placed in the ear for wearable and discrete electrophysiology measurement. Here we present the use of filter bank common spatial pattern (FBCSP), a spatial separation technique that we found to be most effective for cognitive state classification from time-series data [5, 6, 103]. Our FBCSP pipeline consists of a four-stage linear transformation and a robust feature selection algorithm. We observed that FBCSP is accommodating of inter-trials and inter-subject variability, as it enables the extraction of features at different frequency bands and eventually merges them into a final feature vector. FBCSP is also a lightweight training and test model which can be very reliably trained to various conditions and perform classification with ultra-low latency. Thus, this promises a better alternative to using multi-Layer perceptrons or recurrent neural networks [38], which have yet to be proven suitable for on-chip model tuning and

low-power classification.

8.3 Electropyhsiology Hardware Methods

8.3.1 In-Ear and Scalp EEG Acquisition

Brain activity was measured in this study simultaneously from scalp electrodes and in-ear electrodes placed binaurally. Scalp recordings were made using a battery-powered 30-channel dry EEG headset (Quick-30r, CGX Systems, USA) sampled at 500 Hz to a PC over a wireless interface. A total of five electrodes were placed in contact with each ear of the subject. As shown in Fig. 8.1, three electrodes per ear were sensing channels placed inside the ear canal with equal spacing around the canal circumference. Each sensing electrode has an ellipse profile with a height of $\sim$1 mm, and a major and minor axis of 6 mm and 4.5 mm, respectively. One electrode placed on the concha cavum was the reference, and one electrode was placed in the concha cymba was the ground DRL. All ear electrodes were dry Ag/AgCl. The in-ear electrodes were attached to passive leads that were connected to an eight-channel electrophysiology acquisition system (BioRadio, GLNeurotech, USA) sampled at 500 Hz to a PC over Bluetooth.

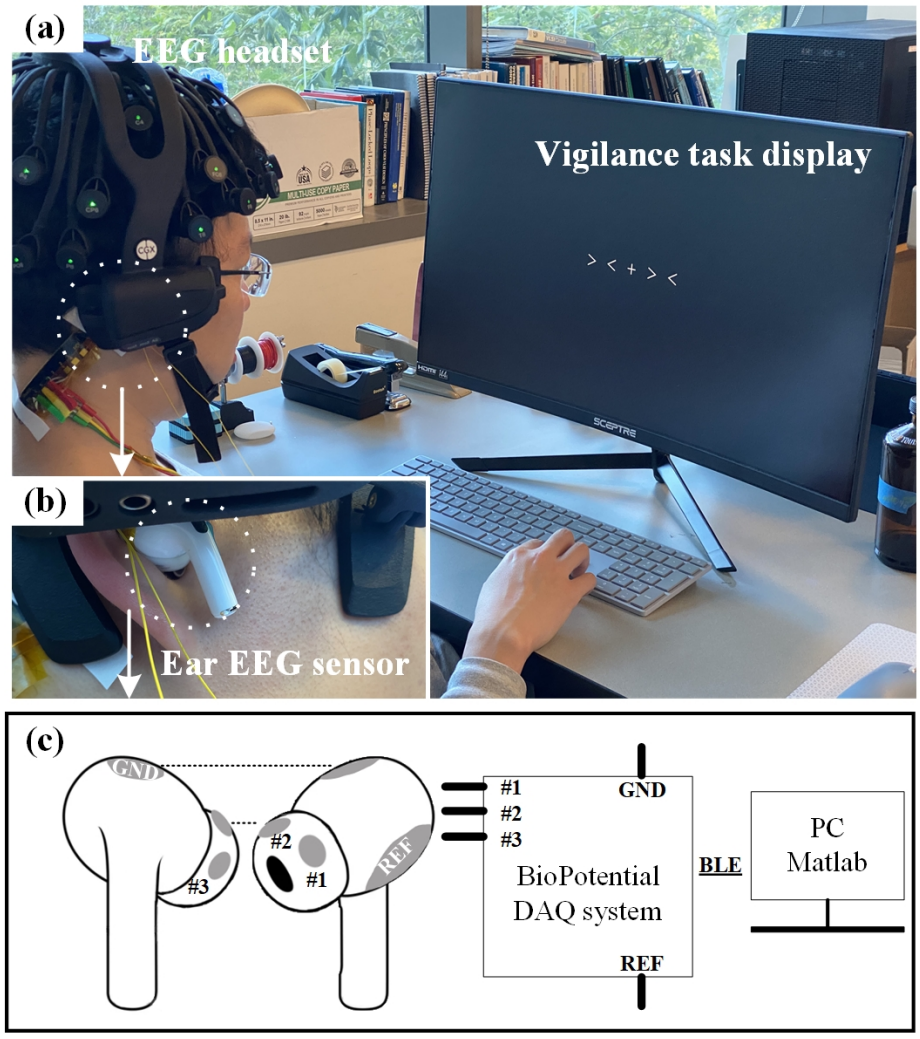

Figure 8.1: Vigilance test setup and in-ear EEG sensor design. (a) Vigilance test setup, (b) Zoom in view of the in-ear EEG sensor inserted into the ear canal along with the earphone, (c) Design of the in-ear EEG sensor and the acquisition system.

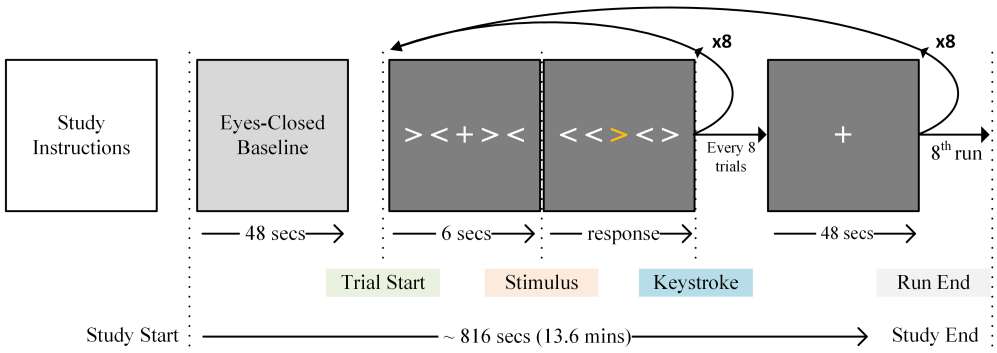

Figure 8.2: Experimental protocol for visual vigilance study begins with a baseline period during which the subject is instructed by on-screen directions to close their eye while the neutral colored, static screen is displayed.

8.4 Vigilance Experimental Methods

8.4.1 Participants

The study consisted of three healthy subjects between the ages of 23 and 31, all male. The subjects did not have a history of neuropathy, neuromuscular disorders, cognitive deficiencies, eye or ear-related diseases, had normal hearing and normal eyesight, or wore corrective lenses. The ear canals of each subject were cleaned with Isopropyl alcohol 30 minutes before in-ear recording to removed cerumen. All subjects had an adequate sleep the night prior to their respective recordings.

8.4.2 Experiment Protocol

To validate the performance of the ear sensor, benchmark auditory steady-state response (ASSR) experiments were conducted before and after the vigilance task. ASSR

is an electrophysiologic response to rapid auditory stimuli, and in-ear EEG sensor has been demonstrated to obtain ASSR and provide objective estimate of subject hearing threshold [21,68]. During the benchmark ASSR experiment, auditory stimuli were generated using broadband uniform white noise amplitude modulated 100 percent by 40 Hz frequencies sinusoidal signal. A Blackman window algorithm was utilized to create the amplitude modulation pattern. A pair of earphones connected via bluetooth were used to present the sound stimulus to subjects at 75 dB for one minute. Characteristic power spectra were obtained based on the raw time series data measurement from each in-ear EEG sensing channel. Qualified ear EEG sensing channels were featured with an around $-130dB(\frac{\mu V}{Hz})$ noise floor and a corresponding 40 Hz ASSR peak with a signal to noise ratio of 5–10 dB.

8.4.3 Stimulus Protocol

To evaluate the attentiveness of subjects, a visual vigilance protocol was designed similar to the one presented in [38], which incorporated an Eriksen flanker task [26] and a psychomotor vigilance task (PVT) [25]. The tasks evaluate the overall behavioral alertness during prolonged fixation and selective attention during reaction-timed button presses.

Subjects fitted with the EEG devices were seated comfortably in a quiet, naturally lit room at a desk in front of a 144 Hz monitor with a keyboard, as depicted in Fig. 8.1. They were directed by on-screen instructions to attend to a fixation cross at the center of the screen and press either the left or right arrow keys on the keyboard to indicate to which direction the fixation cross changed during each trial, according to the experimental protocol in Fig. 8.2. Each trial consisted of a fixation period of 6 seconds, during which

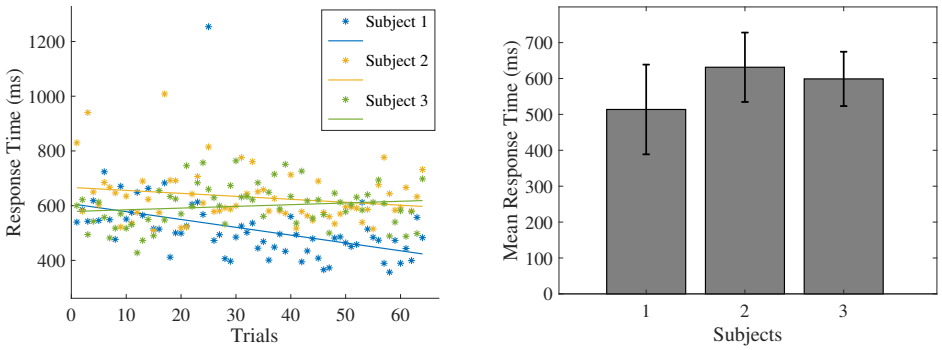

Figure 8.3: Response time calculated between stimulus presentation and keyboard press across all trials.

time the subject was to pay attention to a cross on the screen flanked by a pair of static symbols. The second phase of each trial would change the screen such that the fixation cross became either a left or a right arrow, and the flanking symbols would also change at the same time to random left or right arrows. Phase 3 of each trial occurs when the subject presses the left or right key on the keyboard after seeing the cross change to an arrow. The key pressed is recorded and later compared to the actual direction arrow that was displayed. The reaction time from symbol change to key press is also captured in each trial. After eight trials, there is a 48 second rest period during which the subject is asked to attend to a static screen showing only the fixation cross and no flanking symbols. There are no direction arrows presented or key presses required during the rest period. The cycle repeats for eight runs until 64 trials and eight rest periods are completed, or sooner if the subject decides to end the study early. Subjects are asked not to move during either fixation or rest periods.

8.4.4 Preprocessing

EEG data captured from the scalp headset and in-ear devices went through minimal preprocessing. Raw datasets were loaded into EEGLAB for visualization of time series data and LSL markers. Any channels that were not to be used, such as accelerometer and impedance, were removed, and a bandpass filter (FIR 1 to 58 Hz) was applied to all scalp channels. Data was exported in .edf format.

8.5 Data Analysis and Attention State Classification

Both scalp and in-ear EEG data obtained from all subjects were analyzed using different techniques discussed below. In all of the techniques, around 85% of the trials were used for training and cross-validation while 15% were used for testing. We selected continuous trial intervals for train and test data (eight 6-second attentive, and a 48-second resting phase divided into 8 trials per run i.e., total of 64 trials) to completely separate the train and test data and avoid overfitting. As the total duration of the attentive and rest states is close, the train and test data have almost 50% of attentive and rest labels. We examined the possibility of using baseline machine learning classifiers without feature extraction (i.e., on raw data with lightweight preprocessing as explained in Section 8.4.4) and with feature extraction. Specifically, we implemented a filter-bank common spatial pattern (FBCSP algorithm) for feature extraction.

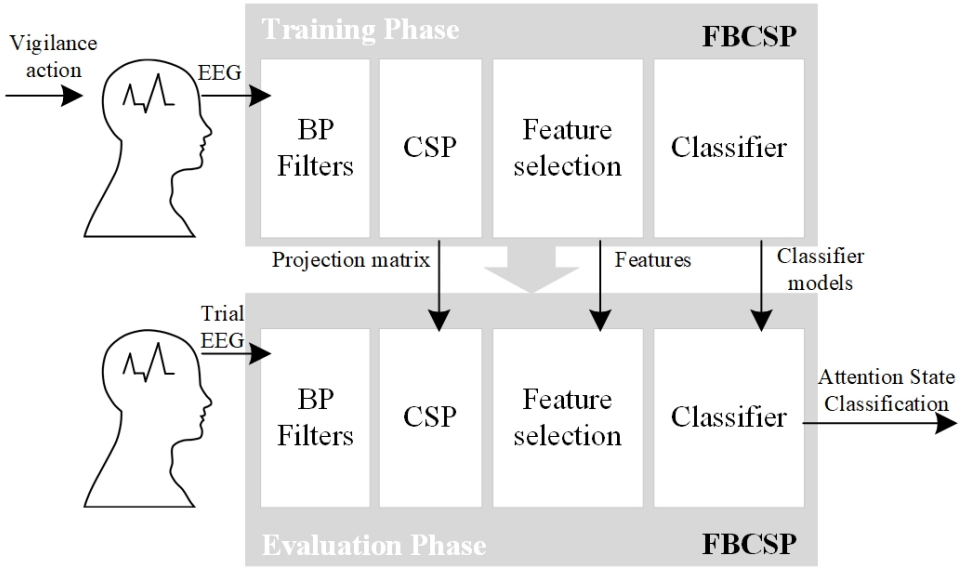

Figure 8.4: The FBCSP processing pipeline.

8.5.1 Filter-Bank Common Spatial Pattern (FBCSP) Algorithm

Common Spatial Pattern (CSP) algorithm is an efficient method for classifying EEG data [33] and has been explored for multi-class feature extractions in BCI systems. However, the effectiveness of CSP depends on subject-specific frequency bands to precisely determine the features. Thus recently there have been some developments on Filter-Bank CSP (FBCSP) algorithm [5] [6]. FBCSP separately calculates the features in each relevant frequency band and combines them into the most significant CSP features based on a mutual information-based best individual feature (MIBIF algorithm) [5].

Our processing pipeline is detailed in Fig. 8.4. It consists of multiple stages of combined signal processing and machine learning techniques to enhance the feature extraction and classification in the presence of signal variability in different operating conditions, acquisition hardware mismatches, and inter-subject signal quality fluctuations.

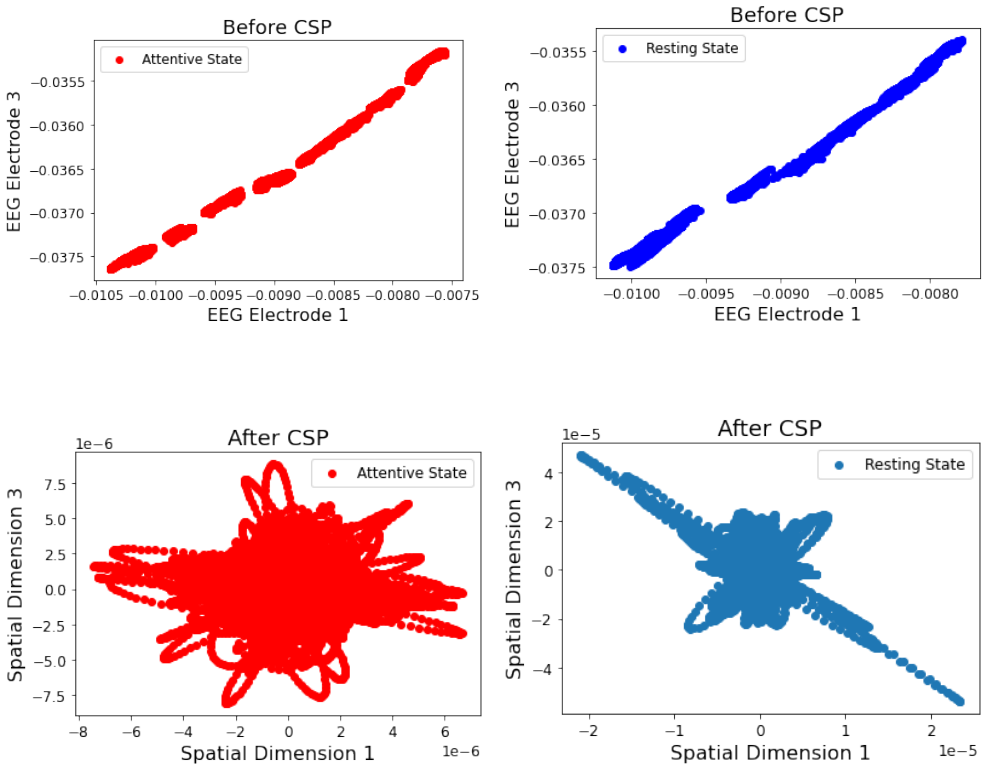

Figure 8.5: Scatter plots of samples belonging to each class to demonstrate their variance in two spatial directions before-CSP and after-CSP transformation. After-CSP transformation plot is obtained by combining the transformed signals from all frequency bands.

The first stage of FBCSP consists of a filter bank comprising multiple Chebyshev Type II band-pass filters between 4–40 Hz and in intervals of 4 Hz. The second stage performs spatial filtering using the CSP algorithm. Each frequency band has its own optimized CSP feature calculation. The primary purpose of CSP is to maximize the variance of class-specific samples in a specific spatial dimension. One typical discrimination of variance in different spatial dimensions is illustrated in Fig. 8.5 for in-ear EEG data (scatter plots of pre-CSP filtered and post-CSP filtered). Before CSP, the variance of samples related to

attentive and resting class is approximately the same across Electrode 1 and Electrode 3. However, there is more variation observed across one particular spatial dimension after the CSP transformation. The CSP algorithm computes the spatial transformed signals $Z_{b,i}$ for each frequency band as,

$$Z_{b,i} = W_b^T E_{b,i} \tag{8.1}$$

where $E_{b,i}$ denotes single-trial (i-th) EEG measurement from which is a filtered input signal through b-th band-pass filter and W_b denotes the corresponding CSP projection matrix. The projection matrices are computed to behave optimal for distinguishing between two cognitive states. This is done by solving the eigenvalue decomposition from the covariance matrices of the measurements of different cognitive states. The spatial filtered signal maximizes the differences in the variance of two classes of measurements. After this, FBCSP feature vectors $v_{b,i}$ are calculated from the transformed signals.

The third stage implements a feature selection algorithm which selects most discriminative CSP features from $v_{b,i}$. This is accomplished by a Mutual-Information based Individual Feature (MIBF) where mutual information of each feature is computed and sorted in descending order. Finally, the first k features are selected to be used for classification. The fourth stage is the classification step, for which we use a Support-Vector-Machine (SVM)-based method with a Radial-Basis-Function (RBF) kernel.

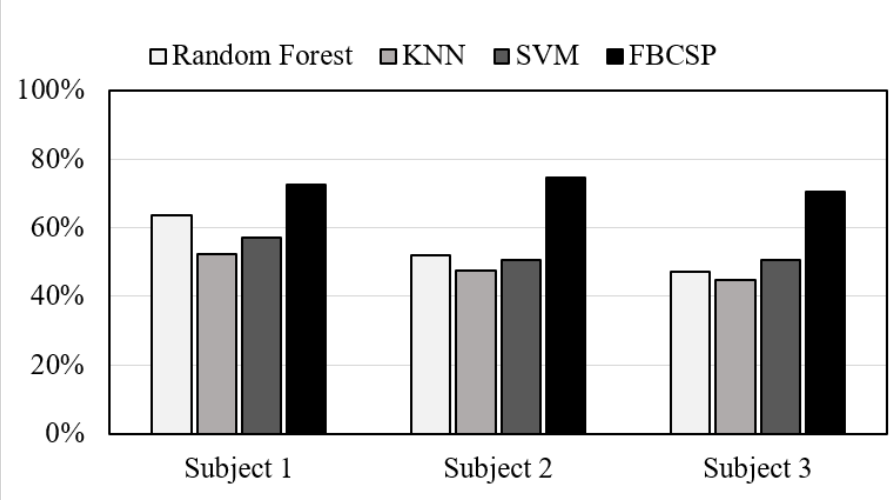

Figure 8.6: Accuracy of *in-ear* EEG signals (with 3 electrodes) using different classification techniques such as RF, KNN, and SVM without any feature extraction, and comparison with FBCSP feature extraction + classification method.

8.5.2 Classification Accuracy

Fig. 8.6 and Fig. 8.7 show the accuracy of the FBCSP and conventional ML techniques on the, respectively, in-ear and on-scalp signals for all the three subjects. There is a significant accuracy gap between Filter-Bank CSP feature extracted classification and baseline methods such as Random Forest (RF), K-Nearest Neighbor (KNN) and Support-Vector Machine(SVM). For the *in-ear* signals, the conventional techniques achieve no better than 54.3% on average. FBCSP, on the other hand, achieves 72.6% average accuracy for the three subjects with a standard deviation of 1.96%. It is noteworthy that for the FBCSP we used a support vector machine (SVM) classifier which, as shown in Fig. 8.6, achieves as low as 52.7% when working on simple preprocessed data.

For the on-scalp data, the FBCSP achieves an average accuracy of 90.2% (1.95%

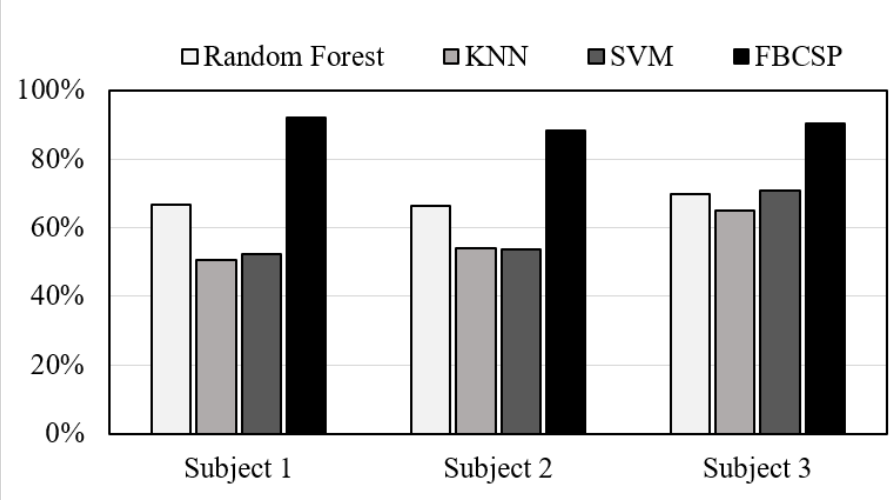

Figure 8.7: Accuracy of *on-scalp* EEG signals (with 25 electrodes) using different classification techniques such as RF, KNN, and SVM without any feature extraction, and comparison with FBCSP feature extraction + classification method.

standard deviation), which is 17.6% higher than the in-ear device accuracy. Without feature extraction, the random forest classifier (the best among the conventional techniques) achieves 67.6%. The FBCSP accuracy on our in-ear EEG dataset is promising, especially it is trained over only 64 trials. This promises a very lightweight training model that can be often trained on the fly. Our FBCSP model is expected to provide higher accuracy (upto 80–85%) when trained with larger datasets and through further experiment trials.

8.6 Conclusion

We presented a low-profile user-generic and portable in-ear EEG instrumentation device with just 5-electrodes capable of classifying cognitive states using a multi-frequency band feature extraction, feature selection, and classification algorithm. We demonstrated

up to 75% accuracy with a minimal in-ear EEG training dataset. This work paves the path for a complete system-on-chip closed-loop brain-state monitor that can be reliably used irrespective of the operating conditions.

Chapter 9

Conclusion

In summary, the ear is an attractive environment for health sensing because it offers a unique combination of physiological and cognitive signals that can be measured from devices made to be comfortable, discrete, and incorporated into existing personal hearables.

Limitations of existing in-ear systems were identified to include robustness, electrode count, fabrication complication, and scalability. These limitations were addressed by the design of universal PCB earpieces with high-density, easy assembly, and manufacturing scalability. Further, development of a consistent Ag-AgCl coating protocol improved electrode performance for dry-contact recording.

The need for versatile data acquisition systems to accommodate multiple modalities is met by the development of an open-source COTS system and a low-power BioADC integrated circuit. Joint electrophysiological and electrochemical sensing paradigms in the ear have been demonstrated for unobtrusive cognitive and metabolic state monitoring.

For future directions of this work, a priority will be the continued development

of in-ear sensing systems directed towards clinically relevant mobile health monitoring platforms to reduce morbidity and mortality across healthcare. In addition, the continued support of open-source efforts are critically important in providing a versatile set of tools to the electrophysiology community, lowering the barrier of entry to in-ear sensing research, accelerating the rate of development in the field for everyone. We plan to continue support of our Crocodile in-ear electrodes and the weDAQ system via their GitHub pages.

The broader capabilities and innovation of weDAQ and NISoC translate to versatile wearable sensing across the body. Integration of multiple sensor streams from subjects presents opportunities for the deployment of machine learning algorithms for diagnostics and wellness purposes. The ISN lab continues to welcome collaborations with industry and clinical partners in translating technology and innovation for healthcare with transformative point-of-care models of active user engagement.

Bibliography

[1] Noise Analysis in Operational Amplifier Circuits. *Texas Instruments, SLVA043B*, 2007.

[2] A. Akinin, N. Govil, H. Poizner, and G. Cauwenberghs. Frequency domain identification of proprioceptive evoked potentials in compliant kinematic experiments. In *2015 7th International IEEE/EMBS Conference on Neural Engineering (NER)*, pages 807–811. IEEE, 2015.

[3] A. Akinin, A. Paul, J. Wang, A. Buccino, and G. Cauwenberghs. Biopotential measurements and electrodes. In *Neural Engineering*, pages 65–96. Springer, Cham, 2020.

[4] H.-S. An, J.-W. Kim, and S.-W. Lee. Design of an asynchronous brain-computer interface for control of a virtual avatar. *2016 4th International Winter Conference on Brain-Computer Interface (BCI)*, pages 1–2, 2016.

[5] K. K. Ang, Z. Y. Chin, C. Wang, C. Guan, and H. Zhang. Filter bank common spatial pattern algorithm on bci competition iv datasets 2a and 2b. *Frontiers in Neuroscience*, 6:39, 2012.

[6] K. K. Ang, Z. Y. Chin, H. Zhang, and C. Guan. Filter bank common spatial pattern (fbcsp) in brain-computer interface. In *2008 IEEE International Joint Conference on Neural Networks (IEEE World Congress on Computational Intelligence)*, pages 2390–2397, 2008.

[7] T. Arakawa, R. Ishikawa, K. Iitani, K. Toma, Y. Iwasaki, and K. Mitsubayashi. Headset bio-sniffer with wireless cmos camera for percutaneous ethanol vapor from the ear canal. *Biosensors and Bioelectronics: X*, 11:100169, 2022.

[8] S. J. Asirvatham. *Mayo clinic electrophysiology manual*. Oxford University Press, 2013.

[9] M. Bariya, H. Y. Y. Nyein, and A. Javey. Wearable sweat sensors. *Nature Electronics*, 1(3):160–171, 2018.

[10] A. R. Bertelsen, H. Bladt, C. B. Christensen, S. L. Kappel, H. O. Toft, M. L. Rank, K. B. Mikkelsen, and P. Kidmose. Generic dry-contact ear-EEG. In *2019 41st Annual International Conference of the IEEE Engineering in Medicine and Biology Society (EMBC)*, pages 5552–5555, 2019.

[11] J. J. Bird, L. J. Manso, E. P. Ribeiro, A. Ekárt, and D. R. Faria. A study on mental state classification using eeg-based brain-machine interface. In *2018 International Conference on Intelligent Systems (IS)*, pages 795–800, 2018.

[12] S. Biswas, D. Chambers, W. D. Hairston, and S. Bhattacharya. Head pose classification for passenger with CNN. *Transportation Engineering*, page 100157, 2022.

[13] M. G. Bleichner and S. Debener. Concealed, unobtrusive ear-centered eeg acquisition: ceegrids for transparent eeg. *Frontiers in human neuroscience*, 11:163, 2017.

[14] J. R. Boston. Spectra of auditory brainstem responses and spontaneous EEG. *IEEE Transactions on Biomedical Engineering*, (4):334–341, 1981.

[15] W. Boucsein. *Electrodermal activity*. Springer Science & Business Media, 2012.

[16] Y.-L. Chen, W.-H. Kuan, and C.-L. Liu. Comparative study of the composition of sweat from eccrine and apocrine sweat glands during exercise and in heat. *International journal of environmental research and public health*, 17(10):3377, 2020.

[17] Y. Chi and G. Cauwenberghs. Micropower non-contact EEG electrode with active common-mode noise suppression and input capacitance cancellation. In *2009 Annual International Conference of the IEEE Engineering in Medicine and Biology Society*, pages 4218–4221, Minneapolis, MN, Sept. 2009. IEEE.

[18] Y. M. Chi and G. Cauwenberghs. Wireless non-contact eeg/ecg electrodes for body sensor networks. In *2010 International Conference on Body Sensor Networks*, pages 297–301. IEEE, 2010.

[19] Y. M. Chi, T.-P. Jung, and G. Cauwenberghs. Dry-contact and noncontact biopotential electrodes: Methodological review. *IEEE Reviews in Biomedical Engineering*, 3:106–119, 2010.

[20] Y. M. Chi, Y.-T. Wang, Y. Wang, C. Maier, T.-P. Jung, and G. Cauwenberghs. Dry and noncontact EEG sensors for mobile brain–computer interfaces. *IEEE Transactions on Neural Systems and Rehabilitation Engineering*, 20(2):228–235, 2012.

[21] C. B. Christensen, J. M. Harte, T. Lunner, and P. Kidmose. Ear-EEG-based objective hearing threshold estimation evaluated on normal hearing subjects. *IEEE Transactions on Biomedical Engineering*, 65(5):1026–1034, 2018.

[22] R. Clayton, O. Bernus, E. Cherry, H. Dierckx, F. H. Fenton, L. Mirabella, A. V. Panfilov, F. B. Sachse, G. Seemann, and H. Zhang. Models of cardiac tissue electrophysiology: progress, challenges and open questions. *Progress in biophysics and molecular biology*, 104(1-3):22–48, 2011.

[23] A. Delorme and S. Makeig. EEGLAB: an open-source toolbox for analysis of single-trial EEG dynamics. *Journal of Neuroscience Methods*, 2004.

[24] S. Dikker, L. Wan, I. Davidesco, L. Kaggen, M. Oostrik, J. McClintock, J. Rowland, G. Michalareas, J. J. Van Bavel, M. Ding, and D. Poeppel. Brain-to-brain synchrony tracks real-world dynamic group interactions in the classroom. *Current biology*, 27(9):1375–1380, 2017.

[25] D. F. Dinges and J. W. Powell. Microcomputer analyses of performance on a portable, simple visual rt task during sustained operations. *Behavior research methods, instruments, & computers*, 17(6):652–655, 1985.

[26] B. A. Eriksen and C. W. Eriksen. Effects of noise letters upon the identification of a target letter in a nonsearch task. *Perception & psychophysics*, 16(1):143–149, 1974.

[27] J. Fan, J. W. Wade, A. P. Key, Z. E. Warren, and N. Sarkar. Eeg-based affect and workload recognition in a virtual driving environment for asd intervention. *IEEE Transactions on Biomedical Engineering*, 65(1):43–51, 2018.

[28] C. for Disease Control Prevention. National diabetes fact sheet: national estimates and general information on diabetes and prediabetes in the united states, 2011. *Atlanta, GA: US department of health and human services, centers for disease control and prevention*, 201(1):2568–2569, 2011.

[29] S. K. Garg, M. Kipnes, K. Castorino, T. S. Bailey, H. K. Akturk, J. B. Welsh, M. P. Christiansen, A. K. Balo, S. A. Brown, and J. L. Reid. Accuracy and safety of dexcom g7 continuous glucose monitoring in adults with diabetes. *Diabetes Technology & Therapeutics*, 24(6):373–380, 2022.

[30] N. Georgi and R. L. B. Jeannès. Proposal of a remote monitoring system for elderly health prevention. In *2017 International Conference on Smart, Monitored and Controlled Cities (SM2C)*, pages 69–74. IEEE, 2017.

[31] V. Goverdovsky, D. Looney, P. Kidmose, and D. P. Mandic. In-ear EEG from viscoelastic generic earpieces: Robust and unobtrusive 24/7 monitoring. *IEEE Sensors Journal*, 16(1):271–277, 2016.

[32] V. Goverdovsky, W. von Rosenberg, T. Nakamura, D. Looney, D. J. Sharp, C. Papavassiliou, M. J. Morrell, and D. P. Mandic. Hearables: Multimodal physiological in-ear sensing. *Sci Rep*, 7(1):6948, 2017.

[33] M. Grosse-Wentrup and M. Buss. Multiclass common spatial patterns and information theoretic feature extraction. *IEEE Transactions on Biomedical Engineering*, 55(8):1991–2000, 2008.

[34] J. Gruzelier and P. Venables. Skin conductance orienting activity in a heterogeneous sample of schizophrenics. *Journal of Nervous and Mental Disease*, 1972.

[35] D. Hölle, J. Meekes, and M. G. Bleichner. Mobile ear-EEG to study auditory attention in everyday life. *Behavior research methods*, 53(5):2025–2036, 2021.

[36] Y.-J. Huang, C.-Y. Wu, A. M.-K. Wong, and B.-S. Lin. Novel active comb-shaped dry electrode for EEG measurement in hairy site. *IEEE Transactions on Biomedical Engineering*, 62(1):256–263, 2015.

[37] F. Islami, E. M. Ward, H. Sung, K. A. Cronin, F. K. Tangka, R. L. Sherman, J. Zhao, R. N. Anderson, S. J. Henley, and K. R. Yabroff. Annual report to the nation on the status of cancer, part 1: national cancer statistics. *JNCI: Journal of the National Cancer Institute*, 113(12):1648–1669, 2021.

[38] D.-H. Jeong and J. Jeong. In-ear EEG based attention state classification using echo state network. *Brain Sciences*, 10(6):321, May 2020.

[39] S. L. Kappel, D. Looney, D. P. Mandic, and P. Kidmose. Physiological artifacts in scalp eeg and ear-eeg. *Biomedical engineering online*, 16(1):1–16, 2017.

[40] S. L. Kappel, M. L. Rank, H. O. Toft, M. Andersen, and P. Kidmose. Dry-contact electrode ear-EEG. *IEEE Transactions on Biomedical Engineering*, 66(1):150–158, 2019.

[41] R. Kaveh, J. Doong, A. Zhou, C. Schwendeman, K. Gopalan, F. L. Burghardt, A. C. Arias, M. M. Maharbiz, and R. Muller. Wireless user-generic ear EEG. *IEEE Transactions on Biomedical Circuits and Systems*, 14(4):727–737, 2020.

[42] P. Kidmose, D. Looney, M. Ungstrup, M. L. Rank, and D. P. Mandic. A study of evoked potentials from ear-EEG. *IEEE Transactions on Biomedical Engineering*, 60(10):2824–2830, 2013.

[43] C. Kim, S. Joshi, H. Courellis, J. Wang, C. Miller, and G. Cauwenberghs. Sub-micro Vrms-Noise Sub- micro W/Channel ADC-Direct Neural Recording With 200-mV/ms Transient Recovery Through Predictive Digital Autoranging. *IEEE Journal of Solid-State Circuits*, 53(11):3101–3110, 2018.

[44] D. Kim, J. Park, J. Hwang, W. H. Cho, and S. W. Lee. Decoding prefrontal cognitive states from electroencephalography in virtual-reality environment. *2020 8th International Winter Conference on Brain-Computer Interface (BCI)*, pages 1–3, 2020.

[45] M. T. Knierim, C. Berger, and P. Reali. Open-source concealed EEG data collection for Brain-computer-interfaces - neural observation through OpenBCI amplifiers with around-the-ear cEEGrid electrodes. *Brain-Computer Interfaces*, 8(4):161–179, Oct. 2021.

[46] P. Kumari, L. Mathew, and P. Syal. Increasing trend of wearables and multimodal interface for human activity monitoring: A review. *Biosensors and Bioelectronics*, 90:298–307, 2017.

[47] J. Lee, K.-R. Lee, U. Ha, J.-H. Kim, K. Lee, S. Gweon, J. Jang, and H.-J. Yoo. A 0.8-V 82.9-μW in-ear BCI controller IC with 8.8 PEF EEG instrumentation amplifier and wireless BAN transceiver. *IEEE Journal of Solid-State Circuits*, 54(4):1185–1195, 2019.

[48] M. S. Lee, A. Paul, Y. Xu, W. D. Hairston, and G. Cauwenberghs. Characterization of Ag/AgCl electrode fabrication methods. *Frontiers in Electronics*, 2021.

[49] P.-E. Liss. The significance of the goal of health care for the setting of priorities. *Health Care Analysis*, 11:161–169, 2003.

[50] L. Littell, L. Roelle, A. Dalal, G. F. Van Hare, W. B. Orr, N. Miller, and J. N. Avari Silva. Assessment of apple watch series 6 pulse oximetry and electrocardiograms in a pediatric population. *PLOS Digital Health*, 1(8):e0000051, 2022.

[51] J. X. Liu, Y. Goryakin, A. Maeda, T. Bruckner, and R. Scheffler. Global health workforce labor market projections for 2030. *Human resources for health*, 15(1):1–12, 2017.

[52] W. C. Lobitz Jr and C. J. Campbell. Physiology of the glands of the human ear canal: Preliminary report. *Journal of Investigative Dermatology*, 19(2):125–135, 1952.

[53] D. Looney, P. Kidmose, C. Park, M. Ungstrup, M. L. Rank, K. Rosenkranz, and D. P. Mandic. The in-the-ear recording concept: User-centered and wearable brain monitoring. *IEEE Pulse*, 3(6):32–42, 2012.

[54] D. Looney, C. Park, P. Kidmose, M. L. Rank, M. Ungstrup, K. Rosenkranz, and D. P. Mandic. An in-the-ear platform for recording electroencephalogram. In *2011 Annual International Conference of the IEEE Engineering in Medicine and Biology Society*, pages 6882–6885. IEEE, 2011.

[55] S. Makeig. Independent component analysis of eeg data. *Advances in Neural Information Processing Systems (NIPS)*, 1995.

[56] S. Makeig. Evaluation of artifact subspace reconstruction for automatic artifact components removal in multi-channel eeg recordings. *IEEE Transactions on Biomedical Engineering*, 2019.

[57] R. Merletti and D. Farina. *Surface electromyography: Physiology, engineering, and applications*. John Wiley & Sons, 2016.

[58] R. Merletti and P. J. Parker. *Electromyography: physiology, engineering, and non-invasive applications*, volume 11. John Wiley & Sons, 2004.

[59] K. B. Mikkelsen, S. L. Kappel, D. P. Mandic, and P. Kidmose. Eeg recorded from the ear: characterizing the ear-eeg method. *Frontiers in neuroscience*, 9:438, 2015.

[60] T. Nakamura, Y. D. Alqurashi, M. J. Morrell, and D. P. Mandic. Automatic detection of drowsiness using in-ear eeg. In *2018 International Joint Conference on Neural Networks (IJCNN)*, pages 1–6, 2018.

[61] C. K. H. Ne, J. Muzaffar, A. Amlani, and M. Bance. Hearables, in-ear sensing devices for bio-signal acquisition: a narrative review. *Expert Review of Medical Devices*, 18(sup1):95–128, 2021.

[62] A. D. Nordin, W. D. Hairston, and D. P. Ferris. Faster gait speeds reduce alpha and beta EEG spectral power from human sensorimotor cortex. *IEEE Transactions on Biomedical Engineering*, 67(3):842–853, 2019.

[63] O. Ogbeiwi. General concepts of goals and goal-setting in healthcare: A narrative review. *Journal of Management & Organization*, 27(2):324–341, 2021.

[64] OpenBCI. Cyton board 8-channels. *https://docs.openbci.com/*.

[65] W. H. Organization. *World health statistics 2023: monitoring health for the SDGs, sustainable development goals*. World Health Organization, 2023.

[66] M. O'Sullivan, J. P. Pena, A. Bocchino, C. O'Mahony, D. Costello, E. Popovici, and A. Temko. Comparison of electrode technologies for dry and portable EEG acquisition. *2017 7th IEEE International Workshop on Advances in Sensors and Interfaces (IWASI)*, pages 15–20, 2017.

[67] T. P. O'Toole, H. M. Blanck, R. Flores-Ayala, K. Rose, D. A. Galuska, J. Gunn, A. O'Connor, R. Petersen, and K. Hacker. Five priority public health actions to reduce chronic disease through improved nutrition and physical activity. *Health Promotion Practice*, 23(1_suppl):5S–11S, 2022.

[68] A. Paul, A. Akinin, M. S. Lee, M. Kleffner, S. R. Deiss, and G. Cauwenberghs. Integrated In-Ear Device for Auditory Health Assessment. *IEEE EMBS*, page 4, 2019.

[69] A. Paul, S. R. Deiss, D. Tourtelotte, M. Kleffner, T. Zhang, and G. Cauwenberghs. Electrode-Skin Impedance Characterization of In-Ear Electrophysiology Accounting for Cerumen and Electrodermal Response. In *2019 9th International IEEE/EMBS Conference on Neural Engineering (NER)*, pages 855–858, 2019.

[70] A. Paul, G. Hota, B. Khaleghi, Y. Xu, T. Rosing, and G. Cauwenberghs. Attention State Classification with In-Ear EEG. In *2021 IEEE Biomedical Circuits and Systems Conference (BioCAS)*, pages 1–5, 2021.

[71] A. Paul, M. Lee, Y. Xu, S. Deiss, and G. Cauwenberghs. A versatile in-ear biosensing system for continuous brain and health monitoring. In *2022 IEEE International Circuits and Systems Conference (ISCAS)*, pages 1–5, 2022.

[72] A. Paul, M. S. Lee, Y. Xu, S. R. Deiss, and G. Cauwenberghs. A versatile in-ear biosensing system and body-area network for unobtrusive continuous health monitoring. *IEEE Transactions on Biomedical Circuits and Systems*, 2023.

[73] J. M. Peake, G. Kerr, and J. P. Sullivan. A critical review of consumer wearables, mobile applications, and equipment for providing biofeedback, monitoring stress, and sleep in physically active populations. *Frontiers in physiology*, 9:743, 2018.

[74] G. Pei, G. Guo, D. Chen, R. Yang, Z. Shi, S. Wang, J. Zhang, and J. Wu. BrainKilter: A real-time EEG analysis platform for neurofeedback design and training. *IEEE Access*, 8:13, 2020.

[75] N. Pham, T. Dinh, T. Kim, Z. Raghebi, N. Bui, H. Truong, T. Nguyen, F. Banaei-Kashani, A. Halbower, T. Dinh, P. Nguyen, and T. Vu. Detection of microsleep events with a behind-the-ear wearable system. *IEEE Transactions on Mobile Computing*, 22(2):841–857, Feb. 2023.

[76] N. Pham, T. Dinh, Z. Raghebi, T. Kim, N. Bui, P. Nguyen, H. Truong, F. Banaei-Kashani, A. Halbower, and T. Dinh. Wake: a behind-the-ear wearable system for microsleep detection. In *Proceedings of the 18th International Conference on Mobile Systems, Applications, and Services*, pages 404–418, 2020.

[77] T. W. Picton, O. G. Lins, and M. Scherg. The recording and analysis of event-related potentials. *Handbook of neuropsychology*, 10:3–3, 1995.

[78] A. T. Poulsen, S. Kamronn, J. Dmochowski, L. C. Parra, and L. K. Hansen. EEG in the classroom: Synchronised neural recordings during video presentation. *Scientific reports*, 7(1):1–9, 2017.

[79] G. Prum, J. Ten Bosch, and H. de Jongh. Jaw muscle emg-activity and static loading of the mandible. *Journal of Biomechanics*, 1978.

[80] U. Rashid, I. Niazi, N. Signal, and D. Taylor. An EEG experimental study evaluating the performance of Texas Instruments ADS1299. *Sensors*, 18(11):3721, Nov. 2018.

[81] A. Riley and E. Nica. Internet of things-based smart healthcare systems and wireless biomedical sensing devices in monitoring, detection, and prevention of covid-19. *American Journal of Medical Research*, 8(2):51–64, 2021.

[82] T. Röddiger, C. Clarke, P. Breitling, T. Schneegans, H. Zhao, H. Gellersen, and M. Beigl. Sensing with earables: A systematic literature review and taxonomy of phenomena. *Proceedings of the ACM on Interactive, Mobile, Wearable and Ubiquitous Technologies*, 6(3):1–57, 2022.

[83] T. Röddiger, T. King, D. R. Roodt, C. Clarke, and M. Beigl. OpenEarable: Open hardware earable sensing platform. In *Proceedings of the 1st International Workshop on Earable Computing, EarComp*, volume 22, pages 29–34, 2022.

[84] P. M. Rodrigues, B. C. Bispo, C. Garrett, D. Alves, J. P. Teixeira, and D. Freitas. Lacsogram: A new EEG tool to diagnose alzheimer's disease. *IEEE Journal of Biomedical and Health Informatics*, 25(9):3384–3395, 2021.

[85] V. R. R. Samson. Electroencephalogram-based openbci devices for disabled people. *Proc. Conf. Micro-Electronics*, 2018.

[86] B. Schazmann, D. Morris, C. Slater, S. Beirne, C. Fay, R. Reuveny, N. Moyna, and D. Diamond. A wearable electrochemical sensor for the real-time measurement of sweat sodium concentration. *Analytical Methods*, 2(4):342–348, 2010.

[87] C. Schwendeman, R. Kaveh, and R. Muller. Drowsiness detection with wireless, user-generic, dry electrode ear EEG. In *2022 44th Annual International Conference of the IEEE Engineering in Medicine and Biology Society (EMBC)*, pages 9–12, 2022.

[88] J. R. Sempionatto, V. R.-V. Montiel, E. Vargas, H. Teymourian, and J. Wang. Wearable and mobile sensors for personalized nutrition. *ACS sensors*, 6(5):1745–1760, 2021.

[89] D. Seok, S. Lee, M. Kim, J. Cho, and C. Kim. Motion artifact removal techniques for wearable EEG and PPG sensor systems. *Frontiers in Electronics*, 2021.

[90] Siddharth, A. N. Patel, T.-P. Jung, and T. J. Sejnowski. A wearable multi-modal bio-sensing system towards real-world applications. *IEEE Transactions on Biomedical Engineering*, 66(4):1137–1147, 2019.

[91] M. Smuck, C. A. Odonkor, J. K. Wilt, N. Schmidt, and M. A. Swiernik. The emerging clinical role of wearables: factors for successful implementation in healthcare. *NPJ Digital Medicine*, 4(1):45, 2021.

[92] A. Sonsale, J. Sharp, and I. Johnson. Gustatory sweating of the external auditory canal. *The Journal of Laryngology & Otology*, 113(11):1000–1001, 1999.

[93] M. Stoeckelhuber, C. Matthias, M. Andratschke, B. M. Stoeckelhuber, C. Koehler, S. Herzmann, A. Sulz, and U. Welsch. Human ceruminous gland: ultrastructure and histochemical analysis of antimicrobial and cytoskeletal components. *The Anatomical Record Part A: Discoveries in Molecular, Cellular, and Evolutionary Biology: An Official Publication of the American Association of Anatomists*, 288(8):877–884, 2006.

[94] T. J. Sullivan, S. R. Deiss, and G. Cauwenberghs. A low-noise, non-contact eeg/ecg sensor. In *2007 IEEE Biomedical Circuits and Systems Conference*, pages 154–157. IEEE, 2007.

[95] Y. R. Tabar, K. B. Mikkelsen, N. Shenton, S. L. Kappel, A. R. Bertelsen, R. Nikbakht, H. O. Toft, C. H. Henriksen, M. C. Hemmsen, M. L. Rank, M. Otto, and P. Kidmose. At-home sleep monitoring using generic ear-EEG. *Frontiers in Neuroscience*, 17:987578, Feb. 2023.

[96] T. Tang, L. Yan, J. H. Park, H. Wu, L. Zhang, H. Y. B. Lee, and J. Yoo. 34.6 EEG dust: A BCC-based wireless concurrent recording/transmitting concentric electrode. In *2020 IEEE International Solid- State Circuits Conference - (ISSCC)*, pages 516–518, 2020.

[97] W. Tang, L. Yin, J. R. Sempionatto, J.-M. Moon, H. Teymourian, and J. Wang. Touch-based stressless cortisol sensing. *Advanced Materials*, 33(18):2008465, 2021.

[98] G. C. Temes. Autozeroing and Correlated Double Sampling Techniques. In J. H. Huijsing, R. J. van de Plassche, and W. M. C. Sansen, editors, *Analog Circuit Design: Low-Noise, Low-Power, Low-Voltage; Mixed-Mode Design with CAD Tools; Voltage, Current and Time References*, pages 45–64. Springer US, Boston, MA, 1996.

[99] J. Teversham, S. S. Wong, B. Hsieh, A. Rapeaux, F. Troiani, O. Savolainen, Z. Zhang, M. Maslik, and T. G. Constandinou. Development of an ultra low-cost SSVEP-based BCI device for real-time on-device decoding. In *2022 44th Annual International Conference of the IEEE Engineering in Medicine & Biology Society (EMBC)*, pages 208–213, 2022.

[100] C. Tronstad, O. Elvebakk, H. Kalvøy, M. R. Bjørgaas, and Ø. G. Martinsen. Detection of sympathoadrenal discharge by parameterisation of skin conductance and ecg measurement. In *2017 39th Annual International Conference of the IEEE Engineering in Medicine and Biology Society (EMBC)*, pages 3997–4000. IEEE, 2017.

[101] J. Wang, R. Liu, Y. Tchoe, A. P. Buccino, A. Paul, A. Antonio-Chronowska, K. A. Frazer, C. Kim, S. Dayeh, and G. Cauwenberghs. Low-Power 256-Channel Nanowire Electrode-on-Chip Neural Interface for Intracellular Electrophysiology. In *2021 IEEE Biomedical Circuits and Systems Conference (BioCAS)*, pages 01–04, 2021.

[102] J. Wang, A. Paul, D. Zhang, J. Wu, Y. Xu, Y. Zou, C. Kim, and G. Cauwenberghs. 1024-Electrode Hybrid Voltage/Current-Clamp Neural Interface System-on-Chip with Dynamic Incremental-SAR Acquisition. In *2020 IEEE Symposium on VLSI Circuits*, pages 1–2, 2020.

[103] Y. Wang, S. Gao, and X. Gao. Common spatial pattern method for channel selelction in motor imagery based brain-computer interface. In *2005 IEEE Engineering in Medicine and Biology 27th Annual Conference*, pages 5392–5395, 2005.

[104] Y. WANG, P. ZHANG, H. SHAO, L. J. ANDES, and G. IMPERATORE. 1015-p: Cost of diabetes complications in us adults aged 65 years or older. *Diabetes*, 70(Supplement_1), 2021.

[105] H. Wey and W. Guggenbuhl. Noise transfer characteristics of a correlated double sampling circuit. *IEEE Trans. Circuits Syst.*, 33(10):1028–1030, Oct. 1986.

[106] H. Wey and W. Guggenbuhl. An improved correlated double sampling circuit for low noise charge coupled devices. *IEEE Transactions on Circuits and Systems*, 37(12):1559–1565, 1990.

[107] R. C. Woodruff, X. Tong, S. L. Jackson, F. V. Loustalot, and A. S. Vaughan. trends in national death rates from heart disease in the united states, 2010–2020. *Circulation*, 146(Suppl_1):A9853–A9853, 2022.

[108] Z. Yang and H. Ren. Feature extraction and simulation of eeg signals during exercise-induced fatigue. *IEEE Access*, 7:46389–46398, 2019.

[109] A. K. Yetisen, J. L. Martinez-Hurtado, B. Ünal, A. Khademhosseini, and H. Butt. Wearables in medicine. *Advanced Materials*, 30(33):1706910, 2018.

[110] L. Yin, M. Cao, K. N. Kim, M. Lin, J.-M. Moon, J. R. Sempionatto, J. Yu, R. Liu, C. Wicker, and A. Trifonov. A stretchable epidermal sweat sensing platform with an integrated printed battery and electrochromic display. *Nature Electronics*, 5(10):694–705, 2022.

[111] I. A. Zaeni, U. Pujianto, A. R. Taufani, M. Jiono, and P. S. Muhammad. Concentration level detection using eeg signal on reading practice application. In *2019 International Conference on Electrical, Electronics and Information Engineering (ICEEIE)*, volume 6, pages 354–357, 2019.

[112] A. Zani and A. M. Proverbio. Cognitive electrophysiology of mind and brain. In *The cognitive electrophysiology of mind and brain*, pages 3–12. Elsevier, 2003.

[113] X. Zhou, Q. Li, S. Kilsgaard, F. Moradi, S. L. Kappel, and P. Kidmose. A wearable ear-eeg recording system based on dry-contact active electrodes. In *2016 IEEE Symposium on VLSI Circuits (VLSI-Circuits)*, pages 1–2, 2016.